

**Faculty of Science and Engineering
Department of Chemical Engineering**

Simulation of Colloidal Suspension Systems

Hongfei Fang

**This thesis is presented for the Degree of
Doctor of Philosophy
of
Curtin University**

March 2010

Declaration

To the best of my knowledge and belief this thesis contains no material previously published by any other person except where due acknowledgment has been made.

This thesis contains no material which has been accepted for the award of any other degree or diploma in any university.

Signature:

Date:

Simulation of Colloidal Suspension Systems

Hongfei Fang

ABSTRACT

Colloidal suspensions are common in everyday experience. Investigating crucial interactions between colloidal particles, understanding and controlling the diffusion of colloidal particles suspended in fluids and autonomously organising colloidal particles into patterns or structures have attracted significant interests in both fundamental research and applied science.

The current research work is focused on the development of simulation platform for colloidal suspension to study the mechanism of colloid particle diffusion and self-assembly behaviour. Based on discrete element method (DEM), the model developed takes into account the crucial interactions, i.e. the electrostatic repulsion force, van der Waals attraction force, Brownian force, hydration force and hydrodynamic force. To investigate diffusion behaviour of a particle in confined suspension, the hydration and hydrodynamic effect are theoretically analysed. And validated by experimental data, the simulation results verify the anisotropic diffusion effect caused by hydration and hydrodynamic force. The diffusion model is also extended to study the diffusion behaviour of charged particle approaching very close (nanoscale) to the confined plane.

Coupled with a simplified fluid flow model, a convective colloidal self-assembly process is investigated on the simulation platform. A detailed insight of the combined influences of fluid flow field, geometrical confinement, and the interparticle interactions on the self-assembly process can be obtained. In this study, different self-assembled structures are simulated and various transition areas are found where a growing crystal transits from n to $n+1$ layer as a function of varied 3 phase contact angle and the velocity and direction of fluid flow. The results indicate that the colloidal particles self-assemble to a more close-packed structure when the fluid flow velocities increase; colloidal monolayer forms in the presence of large fluid velocity in transverse direction; and the structural transition areas vary following the variation of wedge angle.

BRIEF BIOGRAPHY OF THE AUTHOR

Hongfei Fang graduated with Bachelor's degree in Control Science and Engineering with academic distinctions from Zhejiang University, Hangzhou, China in year 2003. He received Curtin International Research Tuition Scholarship (CIRTS) and commenced his PhD research work in August 2006 under the supervision of Dr. Qin Li and Prof. Moses O. Tadé. From December 2006, he spent over one and half years in Max-Planck Institute for Polymer Research, Mainz, Germany, as an exchange student. His research interests are mathematical modelling and Discrete Element Method (DEM) simulations.

List of Publications

Hongfei Fang, Moses. O. Tadé and Qin Li. An explicit scheme for simulating hindered colloidal diffusion near a rigid wall...*To be submitted to Physical Review E*

Hongfei Fang, Moses. O. Tadé and Qin Li. A numerical study on the role of geometry confinement and fluid flow in colloidal self-assembly...*To be submitted to Advanced Powder Technology*

Hongfei Fang, Moses. O. Tadé and Qin Li. A numerical study on defects formation at the onset of 3D colloidal self-assembling. CHEMECA 2010, September 26 – September 29, Adelaide, Australia.

Hongfei Fang, Qin Li and Moses. O. Tadé. The role of geometry confinement in fluid flow driven self-assembly. CHEMECA 2008, September 28 - October 1, Newcastle, Australia.

ACKNOWLEDGEMENTS

“It was the best of times, it was the worst of times...”

--‘A Tale of Two Cities’, Charles Dickens

As I am crossing the finish line of my thesis, the same exciting and nervous feelings well up inside as I had when my baby girl was born just one month ago. Here I would like to express my deepest gratitude to the people who made many valuable contributions to my thesis as it developed through its various stages.

First and foremost I offer my sincerest gratitude to my supervisor, Dr. Qin Li, who has supported me throughout my thesis and my entire PhD with her patience, knowledge and in securing me a scholarship. Qin, it is my great honour to be your first PhD student and I really appreciate for all your encouragement, guidance and confidence in me. One simply could not wish for a better or friendlier supervisor. Sincere thanks to Prof. Moses O Tadé, who offered me such a fascinating study opportunity and gave me continuous reassurance and support. Special thanks to Prof. Gang Rong for his understanding and guidance on my preliminary research; thanks to Prof. Wolfgang Knoll and all my colleagues in MPI-P, Germany, the friendly academic air there helped me a lot in the preparation of my thesis.

Thanks to Chao Li, Yun Yu, Xiangpeng, Tonghua, Hong Zang, Shaomin, Binhui, Pengchao, Yanqiang, Johan, Fonny, Faye and all my colleagues in Zhejiang University, China, for their joyful accompaniment and blessings. Special thanks to Cam and Sue, Guoqiang and Taotao, whenever I ask for help, you are right there. How lucky I am to have such good friends like you in my life.

This work is especially dedicated to my lovely parents for their priceless love and great help during the tough time that I have gone through, and to all my family members. To my beloved two ladies, Meijuan Liu, thanks for being such a wonderful, virtuous and supportive wife to me, taking good care of my daily life and accompanying me on the ‘Long March’ towards my PhD degree. This thesis would not have been possible without your constant support; Qizhen Fang, my lovely baby girl, thanks for joining us and witnessing my preparing this thesis, which is definitely one of the most significant moments for your dad’s life. Last but not the least, I offer my regards and blessings to all of those who have helped me in any respect during the completion of this thesis but I might not have acknowledged.

TABLE OF CONTENTS

ABSTRACT	i
BRIEF BIOGRAPHY OF THE AUTHOR	ii
ACKNOWLEDGEMENTS	iii
TABLE OF CONTENTS	iv
LIST OF FIGURES	vii
LIST OF TABLES	ix
NOMENCLATURE	x

CHAPTER ONE

INTRODUCTION	1-1
---------------------------	------------

1.1 BACKGROUND	1-1
1.2 MOTIVATIONS AND CONTRIBUTIONS	1-2
1.3 OBJECTIVES AND SCOPE	1-4
1.4 STRUCTURE OF THE THESIS	1-4

CHAPTER TWO

LITERATURE REVIEW OF DEM & SIMULATION METHODS USED IN COLLOIDAL SUSPENSION SYSTEM	2-1
--	------------

2.1 DEM SIMULATION METHOD	2-1
2.1.1 Theoretical Background	2-2
2.1.2 Applications and Recent Advances	2-5
2.1.3 Challenges of DEM	2-7
2.2 OTHER SIMULATION METHODS ON COLLOIDAL SYSTEM	2-7
2.2.1 Brownian Dynamics Simulation	2-7
2.2.2 Monte Carlo Simulation	2-9
2.2.3 Lattice Boltzmann Simulation	2-11

CHAPTER THREE

DEVELOPMENT OF SIMULATION PLATFORM.....3-1

3.1	MODEL ESTABLISHMENT	3-1
3.1.1	Hydration Force	3-1
3.1.2	DLVO Forces	3-2
3.1.3	Brownian Force.....	3-5
3.1.4	Hydrodynamic Drag Force	3-8
3.2	SIMULATION PLATFORM DEVELOPMENT	3-8
3.2.1	Programming Language	3-8
3.2.2	Program Structure	3-10
3.2.3	Algorithm Application	3-13
3.3	DATA POST-PROCESSING TECHNIQUE.....	3-15
3.3.1	Data Read Software Development	3-15
3.3.2	Off-line Data 3D Demonstration	3-17

CHAPTER FOUR

DIFFUSION COEFFICIENT ANALYSIS OF BROWNIAN PARTICLE4-1

4.1	INTRODUCTION	4-1
4.2	THEORETICAL BACKGROUND.....	4-3
4.3	MODEL ESTABLISHMENT	4-5
4.3.1	Hydrodynamic Drag Force Revisited	4-5
4.3.2	Simulation Method	4-8
4.4	SIMULATION RESULTS AND DISCUSSIONS	4-12
4.4.1	Model Validity	4-12
4.4.2	The Comprehensive Study of Hindered Diffusion	4-17
4.5	CONCLUSIONS	4-29

CHAPTER FIVE

SIMULATION OF COLLOIDAL SELF-ASSEMBLY5-1

5.1	INTRODUCTION	5-1
5.2	MODEL ESTABLISHMENT	5-3
5.2.1	General Framework	5-3
5.2.2	Consideration on the Fluid Field	5-6
5.2.3	The Rules Set for Particle Deposition	5-8
5.3	RESULTS AND DISCUSSIONS	5-12
5.3.1	Self-assembly under Different Fluid Flow Field.....	5-12
5.3.2	Self-assembly under Different Wedge Shape Angle	5-17
5.3.3	Defect Formation Mechanism	5-18
5.4	CONCLUSIONS	5-22

CHAPTER SIX

CONCLUSIONS AND FUTURE WORK6-1

6.1	CONCLUSIONS	6-1
6.1.1	Development of Simulation Platform.....	6-1
6.1.2	Diffusion Coefficient Analysis of Brownian Particle	6-2
6.1.3	Simulation of Colloidal Self-assembly	6-2
6.2	IDENTIFIED PROBLEMS AND FUTURE WORK.....	6-3
6.2.1	Improvement on Diversity of Geometrical Confinement.....	6-3
6.2.2	Improvement on Particle Packing Rules	6-3
6.2.3	Applications of Simulation Platform ‘SimCos’	6-4

LIST OF FIGURES

Figure 1-1. Thesis flow diagram.	1-6
Figure 2-1. Models of contact forces (Cleary and Prakash, 2004).	2-4
Figure 3-1. Relationship between power spectral density (PSD) and amplitude of Brownian motion.	3-7
Figure 3-2. Flowchart of simulation process.	3-10
Figure 3-3. Data read software GUI.	3-16
Figure 3-4 Flowchart of Data read program.	3-16
Figure 4-1. Illustrative sketch of relation between y and R	4-8
Figure 4-2. Mean square displacements $\langle \Delta x^2 \rangle$, $\langle \Delta y^2 \rangle$ and $\langle \Delta z^2 \rangle$ as functions of time. . 4-12	
Figure 4-3. Schematic diagram of an isolated PMMA sphere confined in a thin glass cell.	4-13
Figure 4-4. The measured diffusion coefficient $D_{ }$ (solid circles) and D_{\perp} (solid triangles) for an isolated sphere near one planar wall, normalized by D_0	4-14
Figure 4-5. D/D_0 for a particle near a planar wall. Comparison among theoretical prediction, experimental data, and simulation CASE I, II and III.	4-16
Figure 4-6. Scheme of the particle diffusion system.	4-17
Figure 4-7. Snapshot of simulation process for particle diffusion in the vicinity of a planar wall.	4-18
Figure 4-8. Mean square displacements $\langle \Delta x^2(t) \rangle$, $\langle \Delta y^2(t) \rangle$ and $\langle \Delta z^2(t) \rangle$ as functions of t	4-19
Figure 4-9. D/D_0 for uncharged particle suspended in aqueous system near a planar wall. Comparison between theoretical prediction and simulation.	4-21
Figure 4-10. D/D_0 for charged particle suspended in aqueous system near a planar wall. Comparison among theoretical prediction, simulation cases of particle in neutral system and in charged system.	4-22
Figure 4-11. Mean square displacements $\langle \Delta y^2(t) \rangle$ as a function of t , for particle of radius 100 nm in charged system near a planar wall ($y/R \sim 1$).	4-24
Figure 4-12. Long time effect of particle's diffusion at $y/R=1.12$	4-24

Figure 4-13. D/D_0 for charged particle suspended in aqueous system near a planar wall. Comparison among theoretical prediction, simulation cases of particle of radius 100 nm, 50 nm and 10 nm.....	4-26
Figure 4-14. Mean square displacements $\langle \Delta y^2(t) \rangle$ as a function of t during 2×10^4 simulation time steps, for particle of radius (a) 50 nm, and (b) 10 nm in charged system near a planar wall ($y/R \sim 1$).	4-27
Figure 4-15. Effect of charged system on the particle diffusion at the nanoscale level.	4-28
Figure 5-1. Geometrical set-up of the simulated cell of a colloidal suspension system.	5-4
Figure 5-2. Scheme of interparticle interactions.	5-4
Figure 5-3. Side sectional view of the simulated fluid flow field in a colloidal suspension system.	5-7
Figure 5-4. General stationary rules for particles deposition.	5-8
Figure 5-5. Growing structural transition condition.	5-9
Figure 5-6. Stationary rules for particles in transition row.	5-11
Figure 5-7. Side sectional view of fluid flow velocity vector contour in the wedge-shape confinement and nearby bulk volume.	5-13
Figure 5-8. Growing crystal structures.	5-14
Figure 5-9. Snapshots of particles dispersion in the bulk volume.	5-15
Figure 5-10. Profiles of forces on a randomly selected particle in CASE I and II.	5-15
Figure 5-11. Profiles of forces on a randomly selected particle in CASE III.	5-16
Figure 5-12. Trajectories of two particles during self-assembly process.	5-19
Figure 5-13. The force profile of the 'red star' particle.	5-20
Figure 5-14. Structures comparison for two different packing options.	5-22

LIST OF TABLES

Table 3-1. Parameters for calculating electrostatic double-layer force.	3-5
Table 3-2. Main functions in simulation model.	3-11
Table 3-3. Main functions in data read program.	3-17
Table 4-1. Stokes' Laws correction factor for a planar wall, Equation 4-5~Equation 4-7.	4-6
Table 4-2. Key simulation parameters of particle diffusion model.	4-11
Table 4-3. Free diffusion coefficient of particle in bulk.....	4-12
Table 4-4. Key parameters used in the experiment (Lin et al., 2000).....	4-13
Table 4-5. D/D_0 for a particle near a planar wall. Comparison among theoretical prediction, experimental data, and simulation CASE I, II and III.....	4-15
Table 4-6. Explicit function of D_{\perp} / D_0 for a particle near a planar wall.	4-16
Table 4-7. D/D_0 for uncharged particle suspended in neutral aqueous system near a planar wall. Comparison among theoretical prediction and simulation results.	4-20
Table 4-8. D/D_0 for charged particle suspended in aqueous system near a planar wall. Comparison among theoretical prediction, simulation cases of particle in neutral system and in charged system.....	4-22
Table 4-9. D/D_0 for charged particle suspended in aqueous system near a planar wall. Comparison among theoretical prediction, simulation cases of particle of radius 100 nm, 50 nm and 10 nm.....	4-26
Table 5-1. Forces acting on the particle.	5-5
Table 5-2. Key simulation parameters of particles self-assembly model.	5-6

NOMENCLATURE

A_H	Hamaker constant (J)
B	Friction coefficient (N s m ⁻¹)
C_H	Hydration constant (N m ⁻¹)
c	Viscous damping coefficient
c_0	Ionic concentration in bulk (mol L ⁻¹)
D	Distance (m), diffusion coefficient (m ² s ⁻¹)
F	Summation of all forces (N)
F_b	Buoyancy force (N)
F_B	Brownian force (N)
F_C	Contact force (N)
F_d	Hydrodynamic force (N)
F_{DLVO}	DLVO forces (N)
F_{edl}	Electrostatic force (N)
F_g	Gravitation force (N)
F_{HYD}	Hydration force (N)
F_n	Normal contact force (N)
F_t	Tangential contact force (N)
F_{vdw}	Van der Waals force (N)
f	Non-contact force (N)
G_i	Gaussian distribution random sequence
h	Planck constant (m ² kg s ⁻¹)
I	Moment of inertia (N m)
k_n	Normal spring constant (N m ⁻¹)
k_t	Tangential spring constant (N m ⁻¹)
k_B	Boltzmann constant (m ² kg s ⁻² K ⁻¹)
M	Summation of moment (N m)
m_p	Particle mass (kg)

n	Refractive index, number of dimension
N	Number of particles
r_i	Coordinates (m)
R	Particle radius (m)
$R(\tau)$	Autocorrelation function
$S(f)$	Single-sided power spectral density
T	Temperature (K)
U	Particle velocity (m s^{-1})
V	Fluid velocity (m s^{-1})
w	Helmholtz free energy for the interaction between two surfaces per unit area (J m^{-2})
x, y, z	Cartesian coordinates (m)
ω	Angular velocity (rad s^{-1})
ε	Dielectric permittivity
ε_0	Vacuum permittivity ($\text{A s V}^{-1}\text{m}^{-1}$)
τ_R	Relaxation time (s)
κ	Inverse debye length (m^{-1})
ρ_p	Particle density (kg m^{-3})
ρ_f	Fluid density (kg m^{-3})
η	Fluid viscosity (Pa s)
μ	Dynamic viscosity ($\text{kg m}^{-1} \text{s}^{-1}$), friction coefficient
ψ	Surface potential (V)
λ	Debye length (m)
λ_{\perp}	Normal correction factor
$\lambda_{//}$	Parallel correction factor
ν_e	Mean ionization frequency of material (Hz)
θ	Wedge contact angle ($^{\circ}$)
σ	Surface charge density (A s m^{-2})
Δt	Time step (s)
$\Delta x(t)$	Displacement (m)
$\langle \Delta x^2(t) \rangle$	Mean square displacement (m^2)

CHAPTER ONE

INTRODUCTION

1.1 BACKGROUND

Colloidal suspensions are complex fluids that consist of mesoscopic particles suspended in a solvent (e.g. water). The colloidal particles are significantly larger than the solvent molecules, but small enough to show Brownian motion. They have recently attracted increasing attention as advanced materials with controlled particulate microstructures, such as photonic crystals (Weitz and Russel, 2004), textured ceramics (Sakka and Suzuki, 2005), and electrorheological / magnetorheological fluids (Phule and Ginder, 1998). Colloidal suspensions play an important role in biology, e.g. blood, and also many industrial products are essentially colloidal suspensions and are important to our daily life. For example, domestic products such as shaving cream, deodorants and weedicide; food processing, preserving and packaging industry; harmful effects' reduction of pollution problems and oil extraction from geological deposits. The dynamic behaviour of colloidal suspension is important from both scientific and industrial viewpoints (Russel et al., 1989, Larson, 1999). It includes many fundamental problems, such as diffusion of colloidal particles under Brownian motion, rheological behaviour of colloidal systems under shear fields and the kinetics of colloidal aggregation, colloidal self-assembly, and crystallization.

Computer simulations serve as adjuncts to theory and real experiments and provide otherwise inaccessible (or not easily accessible) information. As we have full control over the simulation parameters and can measure every conceivable property of a system during a numerical simulation process, computer simulations are more than mere attempts to reproduce experimental results, but provide us detailed autopsies and diagnostics not normally achievable in a laboratory. Over the last several decades, computer simulations have been applied to study a wide range of phenomena in colloidal systems.

1.2 MOTIVATIONS AND CONTRIBUTIONS

The motivations for this study were:

- I. To reduce the requirement for physical prototypes and experiments. Numerical simulation is able to predict the structural and rheological properties of colloidal suspension, and provide more accurate information about colloidal suspension without the restrictions of experimental conditions.

Although diffusion of spherical colloidal particles has been extensively studied experimentally, shortcomings of experimental work are obvious. For example, it cannot be realized through experiment to put a particle closely enough towards a planar wall, so that the investigation of the diffusion behaviour of particle under geometry confinement is inaccessible. Also it is experimentally impossible to switch on or off each interaction forces separately.

- II. To provide more quantitative information about colloidal suspension system. Owing to the scarce information related to colloidal suspension system at the microscopic level, numerical simulation case studies provide vivid view of colloid particle behaviour by three dimensional (3D) demonstration of static suspension system and dynamic process. In current colloid self-assembly simulation models, the interaction forces between particles and between particles and confinement boundaries are always neglected, so that detailed formation mechanisms of crystal ordered structure and defect are illusive.
- III. To establish better understanding of the colloidal particle diffusion behaviour and self-assembly performance. With discrete element method (DEM), the numerical simulation is able to analyse particle

diffusion down to nanoscale distance, and investigate each interaction forces individually, which cannot be realized through experimental studies. However, current application of DEM method are more related to large scale applications, i.e. macro-level behaviour of large particles.

The contributions of this study may be summarized as:

- I. The comprehensive descriptions on development of 3D simulation platform 'SimCos' for colloidal system will serve as a liberal reference for future improvement, especially for simulation platform design used in colloid science and engineering. The computational methods applied in this study examine aspects of colloidal suspension system from a variety of different perspectives, which would be difficult to address in either pure theory or experiment.
- II. The development of colloidal particle diffusion and self-assembly models will illuminate microscopic diffusion and self-assembly processes to an ultra fine timescale which is difficult to observe during experiment. The particle diffusion model developed extends the understanding of the particle diffusion coefficient at the nanoscale level which is difficult to realize in an experimental system.
- III. The computer simulation results would help elucidate the particle diffusion and assembly mechanism at the nanoscale level and study how the assembly properties are affected by varying system parameters during the growth of crystal structure. The knowledge derived from the simulation cases will be useful to effectively control the growth of colloidal crystal structure.

1.3 OBJECTIVES AND SCOPE

The primary objective of this study is to understand the colloidal particle system under microscopic scale, by use of an in-house developed simulation platform in a manoeuvrable way. The scope of the study is summarized as follows:

- I. To develop a simulation platform using programming compiler Microsoft Visual C++ and Open Graphics Library (OpenGL) as the graphical representation of the simulation system.
- II. To investigate theoretically the interaction forces in the colloid system.
- III. To develop suitable mathematical model for colloidal particle diffusing in aqueous solution and investigate diffusion coefficient under geometry confinement by performing simulation on the in-house developed simulation platform.
- IV. To develop suitable mathematical model for colloidal self-assembly process and investigate growing crystal structure under the influence of fluid flow and geometry confinement by performing simulation on the in-house developed simulation platform.
- V. To devise and develop data post-processing software for analysing the data generated from the simulation studies.

1.4 STRUCTURE OF THE THESIS

This section provides a brief overview of the thesis, which is organized in four main chapters and the flow diagram of the thesis structure is shown in Figure 1-1.

Chapter 2 presents a state-of-the-art overview of different numerical simulation methods applied on simulating colloidal suspension system and reviews briefly the DEM method used to simulate various granular flows behaviour of microscale particles, with its theoretical background and recent applications.

Then Chapter 3 presents the development of simulation platform ‘SimCos’ based on DEM method for colloidal suspension system, and introduces data post-processing technique applied for simulation data analysis. The interaction forces taken into account in the model are discussed and the program structure of the simulation platform are described in this chapter.

Chapter 4 deals with the diffusion of a spherical colloidal particle suspended in aqueous solution. Based on the in-house developed simulation platform introduced in Chapter 3, diffusion coefficients of a spherical colloidal particle moving in the vicinity of a planar wall are calculated and analysed for different particle size and neutral and charged systems.

Chapter 5 presents simulation case studies of a large number of colloid particles self-assembling to ordered structure, and the effect of fluid flow field and geometry confinement are investigated.

Finally, Chapter 6 draws the conclusions and provides recommendations for future studies.

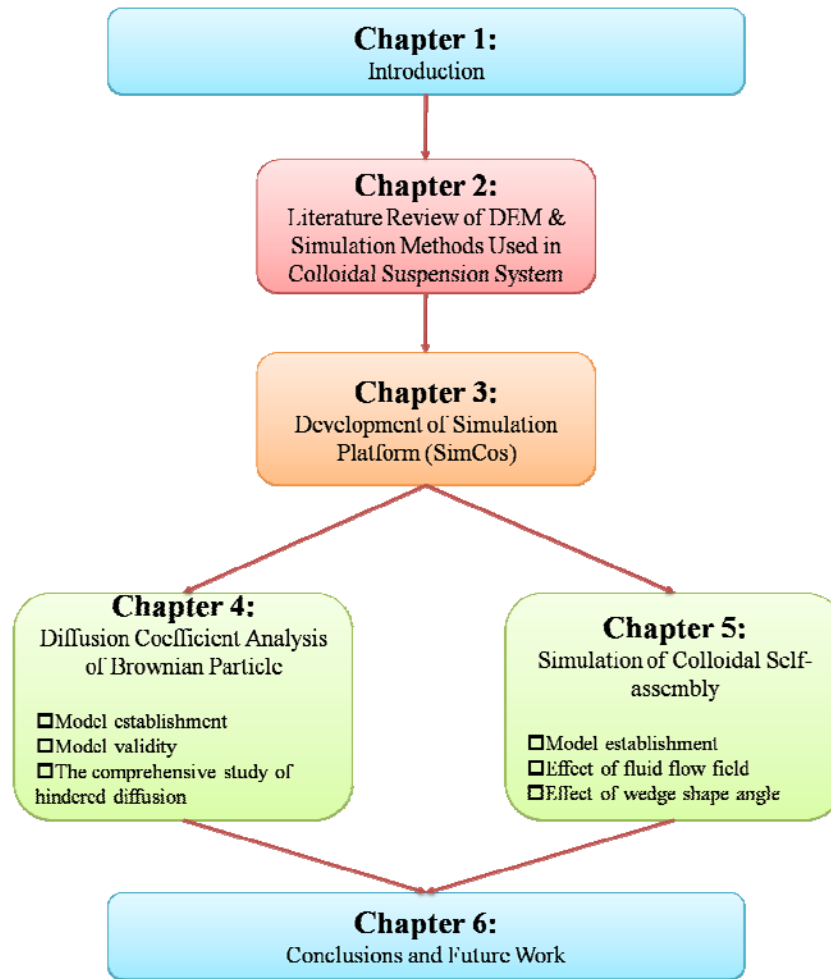


Figure 1-1. Thesis flow diagram.

CHAPTER TWO

LITERATURE REVIEW OF DEM & SIMULATION METHODS USED IN COLLOIDAL SUSPENSION SYSTEM

CHAPTER TWO

LITERATURE REVIEW OF DEM & SIMULATION METHODS USED IN COLLOIDAL SUSPENSION SYSTEM

2.1 DEM SIMULATION METHOD

Discrete element method (DEM), a discontinuous numerical technique analogous to molecular dynamics, was originally developed by Cundall and Strace in the early 1970's to investigate the assembly behaviour of rock mass subjected to mechanical loading conditions (Cundall and Strace, 1979). During the last three decades, DEM has been extended to simulate various granular flows in different processes such as fractured rock masses (Bardet and Scott, 1985), vibrated bed (Gallas et al., 1992, Bizon et al., 1998), fluidized beds (Tsuji et al., 1993, Hoomans et al., 1996, Link et al., 2007, Link et al., 2009), landslides (Cleary and Campbell, 1993, Campbell et al., 1995), river ice jams (Hopkins et al., 1996), hopper flow (Ristow, 1992, Zhu and Yu, 2004), the movement of colloidal particles in ceramic suspensions (Hong, 1997), and mixing process (Stewart et al., 2001, Kuo et al., 2002, Cleary and Sinnott, 2008, Lemieux et al., 2008). Li et al. examined the influence of fluid superficial velocity, particle rigidness and initial packing status upon the properties of the compressed particle bed by DEM simulations (Li et al., 2005). Feng et al. presented a numerical study of segregation and mixing of binary mixtures of particles in a gas-fluidized bed through DEM simulation, where the motion of individual particles is 3D and the flow of continuous gas is 2D (Feng et al., 2004).

It has been known as a reliable solution for researchers who want to study the behaviour of granular materials in both micro and macro scales, and any physical process that involves the disaggregation and movement of material is best modelled with DEM rather than continuum methods such as FEM, because of its significant potential in solving various geometrical problems

and simulating complex behaviour of granular materials compared to the analytical and experimental approaches.

2.1.1 Theoretical Background

In DEM, each particle is treated as an individual element, and each element has its own specific properties, such as position, velocity, charge and dimensions. Furthermore, each particle interacts with its neighbouring particles and its surroundings. A particulate assembly is modelled as a collection of individual particles. The material properties and the size distribution of the particles can be precisely specified as an input to the modelling. The particles interactions and the motion of the particles in the suspension are modelled on a microscopic scale: the motion of each particle is tracked numerically by using a discrete time stepping method. Every time step, the forces that act on a particle are summed and the velocity and the displacement of the particle are calculated by integration of Newton's equations of motion. Strictly speaking, the movement of the particle at each time step is affected not only by the forces from its immediate neighbouring particles and vicinal fluid but also the particles and fluids far away. It is of great complexity to model such propagation process. However, in DEM methodology, an assumption is that by choosing a suitable numerical time step so that during a single time step the disturbance from particles and fluids far away cannot propagate further than their immediate neighbourhood. Thus every time step the forces acting on a particle can be determined exclusively from its interaction with the particles in its neighbourhood. Although this assumption is considered to be the main defect in DEM (Yuu et al., 1995), in a practical situation it is minor compared to other simplifications assumed in DEM such as using spherical particles or not modelling breakage or wear of particles. The DEM is based on a finite number of discrete, semi-rigid usually spherical particles interacting by means of contact or non-contact forces and every single particle in a considered system is described by Newton's

equations of motion. The interactions between contiguous particles are modelled as a dynamic process and the time evolution of the particles is advanced using an explicit finite difference scheme.

The three key aspects of a DEM simulation are (Cleary and Prakash, 2004):

- I. A search grid is occasionally used to construct a particle neighbourhood interaction list. By using only particle pairs in the neighbourhood list reduces the contact detection and force calculation to an $O(N)$ operation, where N is the total number of particles. This approach significantly reduces the computation cost and in this way, problems with up to a million particles are now easily solvable on moderate-speed single-processor workstations, and even a PC can run the simulation of a suspension system composes of large amount of colloidal particles. This contact detection solution is of greater help in the 3D simulation.
- II. The contact forces for each collision are estimated using the spring-dashpot model for each pair of particles in the neighbourhood list, as shown in Figure 2-1. The contact force is further divided into the normal force F_n and tangential force F_t , in the form of

$$F_n = k_n \Delta x_n - c \frac{dx_n}{dt} \quad (2-1)$$

$$F_t = \begin{cases} k_t \Delta x_t - c \frac{dx_t}{dt} & \text{if } |F_t| \leq \mu |F_n| \\ \mu |F_n| \frac{x_t}{|x_t|} & \text{if } |F_t| > \mu |F_n| \end{cases} \quad (2-2)$$

where k_n and k_t are the spring constants in normal and tangential direction, respectively. Δx_n and Δx_t are the overlapping distances between particles or particle and boundary in the normal and tangential directions,

respectively. c , μ are the viscous damping coefficient and friction coefficient respectively.

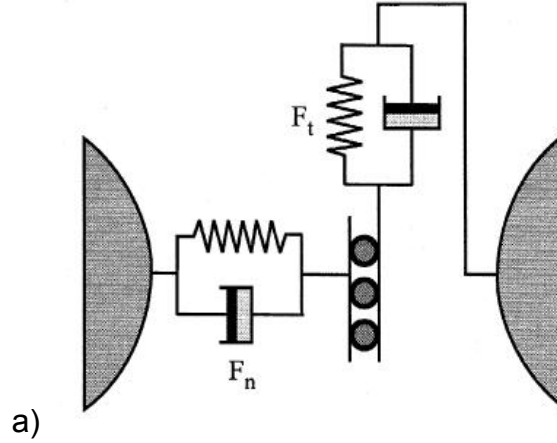


Figure 2-1. Models of contact forces (Cleary and Prakash, 2004).

III. All the contact and other forces acting on the particles can be formulated by Newton's equations of motion as follows

$$m_p \frac{dU_i}{dt} = \sum_j F_{ij} + f_i \quad (2-3)$$

$$I \frac{d\omega_i}{dt} = \sum_j M_{ij} \quad (2-4)$$

where m_p and I are the mass and moment of inertia of the particle, and U and ω are the directional and angular velocities, respectively. The first term on the right hand side of these equations, F_{ij} and M_{ij} are the sum of the force and moment resulting from the contact between the particles i and j . f_i is a non-contact force acting on the particle i which comprises hydrodynamic drag force, hydration force, buoyancy force, gravitation, van der Waals force and electrostatic force.

2.1.2 Applications and Recent Advances

DEM can now be routinely applied in the investigation of particles interactions and particles packing process. There have been numerous and various simulations described in the literature.

DEM simulation offered explanations of material phenomenology and suggested possible practical solutions to solve fine powder flow problems: the achievement of steady, controllable, reproducible discharge of a fine pharmaceutical powder from an intermediate storage vessel to the main process reactor (Baxter et al., 2000). However, the simulation scale was many orders of magnitude fewer than in the industry. Yang et al. used DEM-based dynamic simulation, which treated particle packing as a dynamic process where interparticle forces were explicitly considered, to depict and quantify the 3D chainlike structure of fine particles (Yang et al., 2000). However, the simulation case only considered particle packing when the van der Waals force dominated, while the influence of suspension medium was neglected.

DEM was also used to simulate large-scale particulate flows over large areas of specific real terrains, assuming that it was also possible to identify unstable masses and model their initial release in a shear failure with an appropriate geometry, volume and size distribution (Cleary and Prakash, 2004). Cordelair and Greil used DEM to simulate solid formation during electrophoretic deposition and got an insight into the kinetics determining particle packing and density gradient microstructures of colloidal ZrO_2 ceramic powder (Cordelair and Greil, 2004). The micromechanical behaviour of Si-based particulate systems subjected to tri-axial compression loading was investigated by using DEM simulation. It shows that the single-particle properties of the Si based assemblies significantly affect the micromechanical behaviour of the assemblies and DEM is a powerful tool to

get insights on the internal behaviour of discrete particulates under mechanical loading (Amin and Antony, 2006). However, in this study, only simple linear normal and tangential spring forces were employed in the particle interaction forces model.

The toner behaviour in the development nip of the Océ Direct Imaging (DI) print process is of great importance as the print quality of the DI technology is primarily determined by the toner flow in the region between the DI-drum and the imaging roller. A 2D DEM simulation of toner assembly in the above process was developed and shown that by determining the appropriate interaction rules and the associated parameters, the print quality could be improved (Severens et al., 2006). 2D DEM simulation has been used to model bed comminution to understand the crushing mechanism of multiple particles at a time, and investigate the failure behaviour of particles around the stressing walls and inter-particle breakage and effects of crushing walls and velocities on fragmentation of particles during bed comminution (Khanal et al., 2007). Morgan carried out 2D DEM simulation to examine the dynamics and internal deformation of overlapping volcanoes constructed upon a weak devolvement horizon (Morgan, 2006). Compared to the above 2D DEM simulation studies, 3D DEM simulation is more comprehensive, reliable and consequently require more usage of computation processing power.

Fast common plane (FCP), a fast contact detection algorithm for 3D DEM, was proposed to find the common plane between polygonal particles. By limiting the search space for the plane, it could be about 12-40 times faster than conventional search algorithm for finding the common-plane (Nezami et al., 2004). Although this algorithm improved the contact detection speed during particles packing simulation, it had no insights and investigation for the algorithm applied to more complicated cases such as particle self-assembly or diffusion in suspension.

2.1.3 Challenges of DEM

The main disadvantages of the DEM technique are related to computational capabilities limited by a huge number of particles and relatively small time step used in time integration. However, the capacities of computers are growing dramatically making DEM accessible for use on personal computers (Balevicius et al., 2006).

A significant challenge in DEM modelling is creation of the model itself. For multi-scale modelling that is modelling a colloidal suspension with multiple size particles, the contact detection algorithm will vary from the mono-size system and be much more complicated. Another challenge with DEM is how to specify the micro-properties (particle contact properties) so that the flow on macro-level of the thousands of particles behaves in the same way as real granular flow. It becomes more difficult to determine the DEM particle properties when cohesion is added.

2.2 OTHER SIMULATION METHODS ON COLLOIDAL SYSTEM

As stated above, current research of DEM method are more related to large scale applications, i.e. macro-level behaviour of large particles. Since we are concerned about the colloidal particle properties of micro and submicro scale, and computer simulations have been an integral and efficient tool in the study of colloidal system for many years, the review below intends to provide an overview of main simulation methods applied to colloidal system.

2.2.1 Brownian Dynamics Simulation

The Brownian dynamics simulation algorithm originates from the work of Ermak and McCammon (1978), and is the most simple form of stochastic dynamics algorithms for solving the Langevin equations. In Brownian

dynamics algorithm, the stochastic Brownian force contains no correlations in space or time and the equations are solved with a low-order algorithm (Ermak, 1975, Vangunsteren and Berendsen, 1982, Branka and Heyes, 1998, Branka and Heyes, 1999, Ricci and Ciccotti, 2003). An individual friction and stochastic Brownian force is assigned to each particle of the system as the effect of the fluid. The displacement of a particle is proportional to the force on it gives the correct dynamics, and the trajectory of a particle is simulated stochastically by a series of small displacements chosen from a distribution which is the short time solution of the Smoluchowski equation. Brownian dynamics simulation is intended to describe colloidal suspensions in time scales largely compared to molecular collision times and the macroscopic behavior of Brownian dynamics simulation is diffusive.

Aggregation of magnetic colloids at relatively high solids fraction was studied (Gunal and Visscher, 1996), and the behavior of clusters of ferromagnetic particles in a colloidal dispersion subjected to a simple shear flow was investigated (Sato et al., 1999) through Brownian dynamics simulation. Using Brownian dynamics simulation, Hutter (1999) identified the coagulation time scales in colloidal suspensions for various solid content ratios. The dependence of the time scales on the solid content and the colloidal interaction parameters was investigated to achieve a better understanding of the coagulation mechanisms. Scholl et al. (2000) performed Brownian dynamics simulation to numerically simulate TIRM (total internal reflection microscopy) experiment for the mobility of a colloidal particle in a viscous fluid in close proximity to a planar wall. Brownian dynamics simulations was also used to study the colloidal suspensions of Laponite clay platelets and the behavior of the diffusion coefficients as a function of the platelet concentration and the Debye length were studied (Odriozola et al., 2004). The work of Unni (Unni and Yang, 2005) offer a useful application of Brownian dynamics simulation to study the colloidal particle deposition in a

micro-channel flow by computing the particle deposition in terms of the surface coverage.

As stated above, the Brownian dynamics algorithm is widely used and has been applied to a variety of problems. An advantage of Brownian dynamics is that the simulation (and theoretical) problem of the heating up of the system in non-equilibrium simulations does not occur, because the velocities of the colloidal particles have been eliminated by assuming equilibrium in the momentum variables. However, elimination of velocities results in that there is no obvious way of dealing with the particles interactions anymore and it is not accessible to look into particle's behavior at specific time step, although differentiable potentials such as the Lennard-Jones potential (Heyes, 1988, Dickinson, 2000) was used to avoid this problem in most Brownian dynamics simulations without hydrodynamic interactions. And in Brownian dynamics simulation, very small time step is required to produce accurate thermodynamic and short-time dynamical results, and the generation of the random displacement is extremely costly regarding computation time when many particles are involved, especially in three spatial dimensions.

2.2.2 Monte Carlo Simulation

Monte Carlo simulation method is a class of computational algorithms that rely on repeated random sampling to compute their results. It is a stochastic approach that offers similar advantages of Brownian dynamics with its capability to model processes occurring at rapid time scales. A classical method to conducting Monte Carlo simulation is Metropolis method (Metropolis et al., 1953), which uses the energy of the system as a criterion to evaluate the acceptance or rejection of a Monte Carlo step. Details of Monte Carlo simulations are given by Frankel and Eppenga (1982), Frankel and Ladd (1984a) and Allen and Tildesley (1987).

Monte Carlo simulation was used to study the interaction between two uniformly charged colloidal particles carrying absorbed oppositely charged polyelectrolytes (Granfeldt et al., 1991). Milchev (2002) studied the depletion interaction between a spherical colloidal particle and a planar wall in dilute and semidilute monodisperse solutions by means of a Monte Carlo simulation. The structure and growth kinetics of homo- and heterocoagulation in two dimensions for colloidal particles of equal size were investigated by Monte Carlo simulation (Stoll and Pefferkorn, 1996). Colloidal dispersion under shear, with DLVO (Derjaguin-Landau-Verwey-Overbeek) potential between particles and Brownian motion acting on particles, was modeled by Monte Carlo method (Olivi-Tran et al., 1998). Colloidal particle coagulation and breakup phenomena under turbulent fluid shear was simulated through a Monte Carlo model which was then modified to the form suitable for carrying out sectional mass balance in order to alleviate the memory problem arising from an enormous number of particles encountered in typical colloidal systems (Kim et al., 2003). Chen et al. developed a comprehensive Monte Carlo simulation of colloidal membrane filtration to investigate the phase transition phenomenon of the particle deposition from a fluid-like polarization layer to a solid cake (Chen et al., 2005, Chen and Kim, 2006). More recently, Monte Carlo simulation was employed to investigate the ability of a charged fluid-like vesicle to adhere to and encapsulate an oppositely charged spherical colloidal particle, and a discontinuous wrapping transition of the colloid as a function of the number of charges on the vesicle was revealed (Fosnaric et al., 2009).

As Monte Carlo simulation incorporates additional step of assessing the energy difference in progressing from one time step to the next step, and the algorithm presented for implementation is simple, it accurately represents the physical attributes of the system. And Monte Carlo simulation is free from the restrictions of solving Newton's equations of motion, which allows for cleverness in the proposal of moves that generate trial configurations within

the statistical mechanics ensemble of choice. However, because of not solving Newton's equations of motion, no dynamical information can be obtained from traditional Monte Carlo simulation. And since Monte Carlo simulation is often used in the representation of molecular fluids, it seldom represents the flow of colloidal particles, due to the different nature of the interactions between particles and molecules.

2.2.3 Lattice Boltzmann Simulation

Lattice Boltzmann simulation methods, a mesoscopic numerical method based on the kinetic theory, is a class of computational fluid dynamics (CFD) methods for fluid simulation. McNamara and Zanetti (1988) introduced the first lattice Boltzmann model in 1988, in which Boolean fields were replaced by continuous distributions over the lattices, and the Fermi-Dirac distribution was used as the equilibrium distribution function. Instead of solving the Navier-Stokes equations, the discrete Boltzmann equation is solved to simulate the flow of a Newtonian fluid with collision models (Mcnamara and Zanetti, 1988, Succi, 2001). The overviews of fundamentals of the lattice Boltzmann simulation method are given by Chen and Doolen (1998), Ladd and Verberg (2001), He et al., (2009) and Dunweg and Ladd (2009).

Recently, lattice Boltzmann simulation method has been extended to simulate incompressible thermal flows (McNamara and Alder, 1993, Bartoloni et al., 1993, Chen et al., 1994, McNamara et al., 1997, He et al., 1998, Tang et al., 2005), compressible flows (Kataoka and Tsutahara, 2004), microscale gaseous flows (Lim et al., 2002, Nie et al., 2002), etc.. Ladd (2001) successfully applied the lattice Boltzmann simulation method to colloidal systems and showed that the CPU cost scales linearly with the number of particles. Moreover, he showed how fluctuations can be included into the model, which is essential in order to investigate Brownian motion. Basagaoglu et al. (2008) used a two dimensional lattice Boltzmann model to

simulate trajectories of individual inert particles through narrow smooth-walled and rough-walled channels under relatively low Reynolds number flow conditions, and provide a qualitative indication of the behavior of three dimensional experimental systems.

In many lattice Boltzmann simulation models of particle-fluid problems stated above, the interparticle interactions are either ignored or simply treated to collisions between particles. However, more accurate resolutions and a detail analysis of particle interactions are required in most practical applications. Forces acting discretely on each individual particle while experiencing many-body interferences from the neighbouring particles should be accurately described in order to develop a consummate simulation model of colloidal suspension system. To do so, an ideal model should then narrow its scope to a microscopic scale and compute each distinct force and displacement more actually in three spatial dimensions, thus the DEM method is employed to meet this need.

CHAPTER THREE

DEVELOPMENT OF SIMULATION PLATFORM

CHAPTER THREE

DEVELOPMENT OF SIMULATION PLATFORM

3.1 MODEL ESTABLISHMENT

As stated in Chapter 2, previous DEM applied simulation works mainly include contact forces such as elastic, cohesion and friction force. However, in our simulation model, we focus more on non-contact forces such as hydration force, DLVO forces, Brownian force and hydrodynamic drag force (Li et al., 2008, Fujita and Yamaguchi, 2008). This is because the simulation object is of nanoscale and the above mentioned non-contact force play more important roles compared to contact forces between colloidal particles. The detail of interaction models are discussed as follows.

3.1.1 Hydration Force

In the case of hydrophilic colloidal particles, silica particles in our simulation case for example, the hydration forces are believed to arise from strongly H-bonding surfaces, such as hydrated ions or hydroxyl groups (Israelachvili, 1992). The boundary layer is termed the hydration layer, which was first presented by Derjaguin and his colleagues (Derjaguin and Kussakov, 1939). It was experimentally found that hydration forces between hydrophilic silica surfaces in water are an order of magnitude larger than the electrostatic double-layer repulsive force in a short-range separation (Israelachvili, 1992, Yotsumoto and Yoon, 1993). This hydration repulsive force would be helpful in preventing the particles from approaching each other, and thus lead to a high stabilization of an aqueous colloidal suspension. Empirically, the hydration repulsion energy per unit area between two hydrophilic surfaces is written as

$$w = C_H e^{-D/\lambda} \quad (3-1)$$

where $\lambda \approx 1$ nm is the decay length, D is the distance between bare particle and plane (Peschel et al., 1982, Israelachvili and Wennerstrom, 1996, Valle-Delgado et al., 2005, Peng et al., 2006), and $C_H = 1.2$ mN m⁻¹ is the hydration constant for quartz (Skvarla and Kmet, 1991). So, with Derjaguin approximation, the hydration force between particle and plane is

$$F_{HYD} = 2\pi R \cdot w = 2\pi R C_H e^{-D/\lambda} \quad (3-2)$$

The hydration layer thickness for both silica particle and silica plane is about 7 nm (Israelachvili, 1992, Sasaki and Maeda, 1994).

3.1.2 DLVO Forces

DLVO theory was developed by Derjaguin, Landau, Verwey, and Overbeek to explain the aggregation of aqueous dispersions quantitatively (Derjaguin, Acta Physicochim. URSS 1939, L.D. Landau, 1941). DLVO forces composite the attractive van der Waals force and the repulsive electrostatic double-layer force. Van der Waals force promotes coagulation while the electrostatic double-layer force stabilizes dispersions.

The van der Waals energy per unit area between two identical planar surfaces is

$$w = -\frac{A_H}{12\pi D^2} \quad (3-3)$$

where $A_H = 7.65 \times 10^{-21}$ J is Hamaker constant for silica-water-silica system, calculated from

$$A_H = \frac{3}{4} k_B T \left(\frac{\varepsilon_1 - \varepsilon_2}{\varepsilon_1 + \varepsilon_2} \right)^2 + \frac{3h\nu_e}{16\sqrt{2}} \frac{(n_1^2 - n_2^2)^2}{(n_1^2 + n_2^2)^{3/2}} \quad (3-4)$$

where k_B is the Boltzmann constant, T is the room temperature, ε_1 and ε_2 are the dielectric permittivity of silica and water, respectively, h is the Planck

constant, ν_e is the mean ionization frequency for silica, n_1 and n_2 are the refractive indices of silica and water, respectively (Hunter, 2001, Butt et al., 2003, Bergna and Roberts, 2006).

With Derjaguin approximation, the van der Waals force between two spherical particles is

$$F_{\text{vdw}} = \pi R \cdot w = -\frac{A_H R}{12D^2} \quad (3-5)$$

And the van der Waals force between spherical particle and plane is

$$F_{\text{vdw}} = 2\pi R \cdot w = -\frac{A_H R}{6D^2} \quad (3-6)$$

The constant potential electric double layer energy per unit area is

$$\begin{aligned} w &= \varepsilon \varepsilon_0 \kappa \psi_1 \psi_2 \left[\csc h \kappa D + \frac{\psi_1^2 + \psi_2^2}{2\psi_1 \psi_2} (1 - \coth \kappa D) \right] \\ &= \varepsilon \varepsilon_0 \kappa \psi_1 \psi_2 \left[\frac{2}{e^{\kappa D} - e^{-\kappa D}} + \frac{\psi_1^2 + \psi_2^2}{2\psi_1 \psi_2} \left(1 - \frac{e^{\kappa D} + e^{-\kappa D}}{e^{\kappa D} - e^{-\kappa D}} \right) \right] \end{aligned} \quad (3-7)$$

where ε is the dielectric permittivity, ε_0 is the vacuum permittivity, ψ_1 and ψ_2 are the surface potentials of two particles or particle and plane, respectively, and κ is the inverse Debye length. For an aqueous monovalent salt solution at room temperature, the inverse Debye length is given by

$$\kappa = \frac{\sqrt{c_0 \frac{L}{\text{mol}}}}{3.04 \times 10^{-10} \text{ m}} \quad (3-8)$$

with the ionic concentration c_0 in mol L^{-1} .

The constant charge electric double layer energy per unit area is

$$w = \frac{\sigma_1 \sigma_2}{\varepsilon \varepsilon_0 \kappa} \left(\frac{1 + e^{-\kappa D}}{\sinh \kappa D} \right) \quad (3-9)$$

where σ_1 and σ_2 are the surface charge densities that relate to the surface potential in the form of $\sigma_1 = \varepsilon \varepsilon_0 \kappa \psi_1$ and $\sigma_2 = \varepsilon \varepsilon_0 \kappa \psi_2$, respectively.

Under low potential conditions and small degrees of double layer overlap ($e^{-\kappa D} \ll 1$), both Equation 3-7 and Equation 3-9 reduce to the approximation form as

$$w = 2\varepsilon \varepsilon_0 \kappa \psi_1 \psi_2 e^{-\kappa D} \quad (3-10)$$

In the following simulation cases, the surface potential are kept fixed and Equation 3-10 is used as an approximation for calculating electrostatic double layer force. Because the Equation 3-10 helps to keeps the computational effort low, and it is a good approximation for most simulation conditions that particles are with small degrees of double layer overlap. Then with Derjaguin approximation, the electrostatic double-layer force between two spherical particles is

$$F_{\text{edl}} = \pi R \cdot w = \pi R \varepsilon \varepsilon_0 \kappa \psi_1 \psi_2 \left[\frac{2}{e^{\kappa D} - e^{-\kappa D}} + \frac{\psi_1^2 + \psi_2^2}{2\psi_1 \psi_2} \left(1 - \frac{e^{\kappa D} + e^{-\kappa D}}{e^{\kappa D} - e^{-\kappa D}} \right) \right] \quad (3-11)$$

And its approximation form is

$$F_{\text{edl}} = \pi R \cdot w = 2\pi R \varepsilon \varepsilon_0 \kappa \psi_1 \psi_2 e^{-\kappa D} \quad (3-12)$$

The electrostatic double-layer force between spherical particle and plane is

$$F_{\text{edl}} = 2\pi R \cdot w = 2\pi R \varepsilon \varepsilon_0 \kappa \psi_1 \psi_2 \left[\frac{2}{e^{\kappa D} - e^{-\kappa D}} + \frac{\psi_1^2 + \psi_2^2}{2\psi_1 \psi_2} \left(1 - \frac{e^{\kappa D} + e^{-\kappa D}}{e^{\kappa D} - e^{-\kappa D}} \right) \right] \quad (3-13)$$

And its approximation form is

$$F_{\text{edl}} = 2\pi R \cdot w = 4\pi R \varepsilon \varepsilon_0 \kappa \psi_1 \psi_2 e^{-\kappa D} \quad (3-14)$$

Values of parameters used to calculate the electrostatic double-layer force are listed in Table 3-1.

Table 3-1. Parameters for calculating electrostatic double-layer force.

Variables	Base values
Particle radius (nm), R	100
Surface potential of particle (mV), ψ_1	-30
Surface potential of wall (mV), ψ_2	-50
Bulk concentration (mol L ⁻¹), c_0	1.0×10^{-4}
Dielectric permittivity of water, ε	80
Vacuum permittivity (A s V ⁻¹ m ⁻¹), ε_0	8.85×10^{-12}
Temperature (K), T	298

3.1.3 Brownian Force

In this section, a detailed deduction process of Brownian force is presented. For colloidal particle suspended in aqueous solution, its Brownian motion is described by Langevin equation,

$$m_p \frac{dU}{dt} + BU = F_B \quad (3-15)$$

where m_p is the particle mass, U is the particle velocity, $B = 6\pi\eta R$, is called friction coefficient, and F_B is the Brownian force. With boundary condition: $t = 0, r = 0; t = -\infty, U = 0$, and the system is in thermodynamic equilibrium, i.e.

$$\frac{1}{2} m_p \langle U^2 \rangle = \frac{n}{2} k_B T \delta \quad (3-16)$$

where n is the number of dimension.

The solution to Equation 3-15 is

$$U(t) = \frac{1}{m_p} e^{(-t/\tau_R)} \int_{-\infty}^t e^{(t'/\tau_R)} F_B(t') dt' \quad (3-17)$$

The autocorrelation function of velocity is

$$\begin{aligned} R_U(\tau) &= E[U(t)U(t-\tau)] = \frac{1}{m_p^2} e^{(-2t/\tau_R)} \int_{-\infty}^t \int_{-\infty}^{t-\tau} e^{[(t'+t'')/\tau_R]} E[F_B(t')F_B(t'')] dt' dt'' \\ &= \frac{1}{m_p^2} e^{(-2t/\tau_R)} \int_{-\infty}^t \int_{-\infty}^t e^{[(t'+t''-\tau)/\tau_R]} R_F(\tau) dt' dt'' = \frac{1}{2m_p^2} e^{(-2t/\tau_R)} e^{(-\tau/\tau_R)} R_F(\tau) \int_{-\infty}^{2t} e^{(\xi/\tau_R)} d\xi \\ &= \frac{R_F(\tau)}{2Bm_p} e^{(-\tau/\tau_R)} \end{aligned} \quad (3-18)$$

Substituting Equation 3-16, the following equations are given for autocorrelation function of Brownian force in one dimension .

$$R_F(\tau) = 2Bk_B T \delta(\tau), \text{ for } n=1 \quad (3-19)$$

On the other hand, the autocorrelation function $R(\tau)$, is the inverse Fourier transform of the power spectral density (PSD), which describes how the power of a signal or time series is distributed with frequency. There are various types of PSD, such as PSD of acceleration, PSD of velocity, PSD of force (Equation 3-19) (Ounis et al., 1991). And thus the corresponding autocorrelation function varies. Generally,

$$R(\tau) = E[n(t)n(t-\tau)] = \frac{S(f)}{2} \delta(\tau), \quad (3-20)$$

or

$$R(\tau) = E[n(t)n(t-\tau)] = S(f) \delta(\tau), \quad (3-21)$$

where $S(f)$ is the single-sided PSD, and $\frac{S(f)}{2}$ is the double-sided PSD.

The Gaussian white noise signal can be modelled as

$$n(t_i) = G_i \cdot \sqrt{\frac{S(f)}{2\Delta t}} \quad (3-22)$$

where G_i is a (0, 1) Gaussian white noise signal sequence, and $\frac{S(f)}{2\Delta t}$ is the variance of the noise signal, namely the square value of standard deviation (amplitude). $\frac{S(f)}{2\Delta t}$ is the area under the PSD curve in the $PSD-f$ graph (Figure 3-1), Δt is the sampling period, namely time step of Brownian motion.

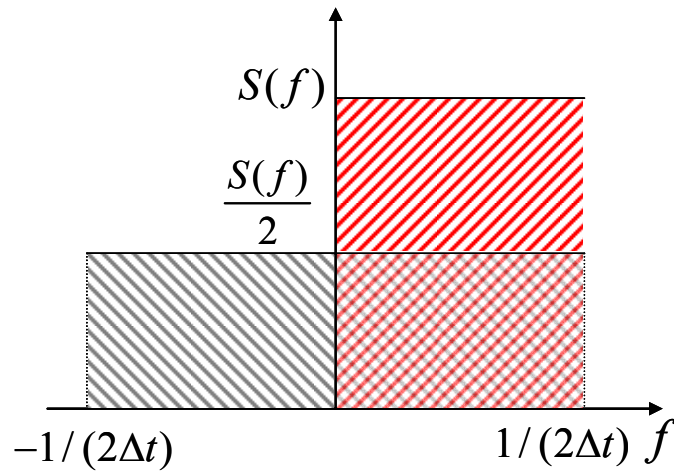


Figure 3-1. Relationship between power spectral density (PSD) and amplitude of Brownian motion.

And thus, PSD of Brownian force and Force Autocorrelation Function is

$$R_F(\tau) = E[F_B(t)F_B(t-\tau)] = \frac{S_F(f)}{2} \delta(\tau) \quad (3-23)$$

Comparing Equation 3-19 with Equation 3-23, it comes

$$\frac{S_F(f)}{2} = 2Bk_B T, \quad (3-24)$$

and Brownian force for free particle in bulk suspension is given by

$$F_B = G_i \sqrt{\frac{S_F(f)}{2\Delta t}} = G_i \sqrt{\frac{2Bk_B T}{\Delta t}} = G_i \sqrt{\frac{12\pi k_B T \eta R_{HYD}}{\Delta t}} \quad (3-25)$$

3.1.4 Hydrodynamic Drag Force

When a colloidal particle with a radius of R , suspended in a quiescent medium of viscosity η , moves freely with velocity U , it experiences a hydrodynamic drag force opposite to its direction of motion, in the case of the low Reynolds number, is

$$F_d = -6\pi\eta RU \quad (3-26)$$

For a particle moving under geometry confinement, e.g. in the vicinity of a planar wall, the hydrodynamic drag force experienced is larger than in the bulk, which will be discussed in detail in Chapter 4.

3.2 SIMULATION PLATFORM DEVELOPMENT

3.2.1 Programming Language

The simulation platform is built on a 32 bit windows based platform with 800 x 600 display resolution. The programming language used to develop this platform is C++ and the compiler is Microsoft Visual C++, which is a commercial integrated development environment (IDE) product engineered by Microsoft for programming languages. The version of Visual C++ used was Microsoft Visual Studio 2005. Compared to other programming languages such as Visual Basic (VB), C++ together with its compiler Visual C++ have the following advantages:

- I. The code is written as a library of routines in object-oriented Visual C++, which aims to provide a flexible environment for the general task of managing particles in a container.
- II. Ability to create windows based graphical user interface (GUI) application.
- III. Stability and speed. Especially for really large problems, and intermediate problems, object-oriented programming is a necessity for stable, maintainable code. And through simplifying the loading of resources and giving message loop, each iteration will be significantly faster.
- IV. Great reusability from code through inheritance, that is we do not have to throw the prototype away, but just flesh it out with real functionality. In other words, it is easy to directly alter the code underneath. However, with other programming language, VB for example, we would be stuck with the encapsulation provided. The VB statements are too weak to go digging underneath. Although the application programming interface (APIs), formerly called the Win32 can be accessed by directly opening a system dynamic-link library (DLL), we cannot do much in the way of the program's structure, because it has already been created by VB.

The graphical representation of the simulation system is Open Graphics Library (OpenGL), which is a standard specification for writing applications that produce simple and interactive 2D and 3D computer graphics applications, from 3D animation, CAD-aided design to visualized simulation. Since it came out from 1992, OpenGL has developed as the only open graphics standard which is independent of the application platform. A typical OpenGL applications can run on any platform, by re-compiling the OpenGL library of the target system.

Since OpenGL is included in Microsoft windows operation system, it can be integrated with Visual C++ compactly, and realize the computing and graphics algorithms efficiently. To put it simply, OpenGL has functions of model, transformation, colour processing, light processing, texture mapped, image processing, animation and object motion blur, and so on.

3.2.2 Program Structure

The basic structure of simulation process is shown in Figure 3-2, and the main functions of the simulation platform are listed in Table 3-2.

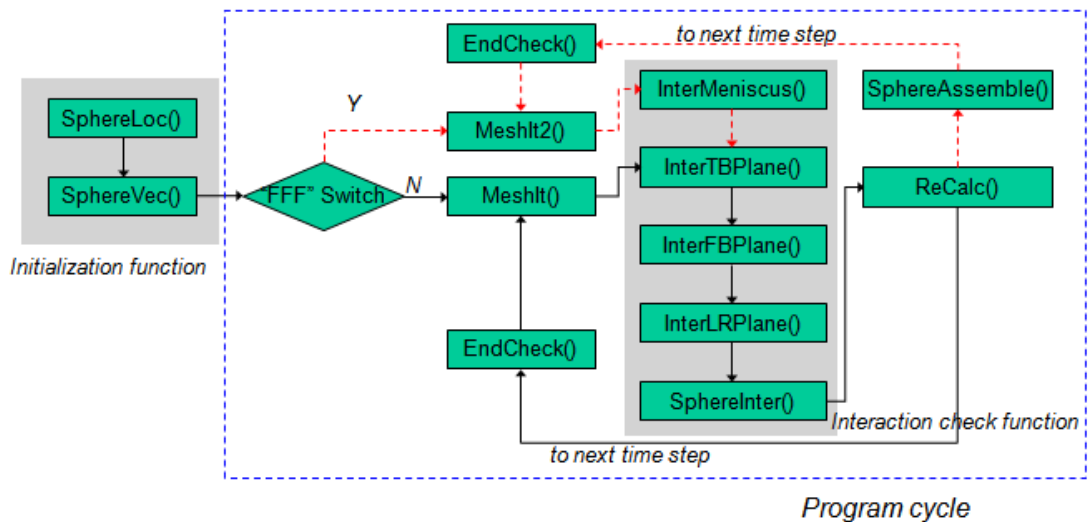


Figure 3-2. Flowchart of simulation process.

Table 3-2. Main functions in simulation model.

Function Name	Function
SphereLoc()	Get spheres initial random locations
SphereVec()	Get spheres initial random velocities
'FFF' Switch()	Check if fluid flow field takes effect
MeshIt()	Locate all spheres into their meshes
MeshIt2()	Locate all spheres into their new meshes as geometry changed
InterWedge()	Check interaction between spheres and wedge
InterTBPlane()	Check interaction between spheres and top & bottom planes
InterFBPlane()	Check interaction between spheres and front & back planes
InterLRPlane()	Check interaction between spheres and left & right planes
SphereInter()	Check interaction between spheres
ReCalc()	Calculate new coordinates and velocities of all spheres
SphereAssemble()	Self-assembly process of all spheres
EndCheck()	Check if process finish or not
KeyPressed()	Simulation platform operation keys

3.2.2.1 Initialization

In the initialization function, random functions are used to randomly locate all particles in suspension with initial velocities. By treating system clock as a random seed, *srand(time(0))* function is used to generate random number. In this way, as time processing, the random seed varied to make sure random numbers generated are different. And the distance between every two

particles are checked to avoid overlap between them, which makes particles suspend evenly.

3.2.2.2 *Simulation program cycle*

It is important to recalculate and update the size of the 3D mesh xyz array if particle radius and container size change. Visual C++ coding of this section is located in the *MeshIt* function.

In the interaction check function, the interaction between particle-particle and particle-wall are checked and calculated, under neighbourhood criterion.

The '*FFF*' switch, *MeshIt2*, *InterWedge* and *SphereAssemble* functions are a library of sample routines which can be easily implemented into the backbone model, when simulating colloidal self-assembly process which will be discussed in Chapter 5.

During each simulation cycle, there's a simulation process *endcheck* function to check if the process is finished or not. The criterion to determine the end of a process is different for different simulation cases. For a particle diffusion simulation case which will be discussed in Chapter 4, an overall simulation time is preset to determine simulation process ending. For colloidal self-assembly simulation case, a preset ratio of particles formed ordered structure is used to determine simulation process ending.

3.2.2.3 *Data output*

In the simulation platform, there are two options to output simulation data. The first one is to output data with decimal format, which can be directly read from any text based program like notepad. The problem with this type of data is that it takes up too much computer hard disk space and is difficult to open when file is large. The other option used in this simulation program is to

output data with binary format, which is a much smaller size data file. For simulation data output, a time step called sample time period is set to control the frequency of data output, so that the data file size is reduced and data at specific time steps can be analysed easily. And data post-processing work including data read software development and off-line simulation process demonstration technique are used to analyse the simulation data, which will be introduced in the following section.

3.2.3 Algorithm Application

The application of DEM to a system includes four basic steps, which are discussed in detail as follows:

3.2.3.1 *Mesh the system and referencing all particles*

During the simulation process, it is important to determine particle's properties at each time step. In this way, all particles need to have a specific number to be tracked. And to find particles which have interaction in between, the general search procedure is of the size $O(N^2)$, where N is the total number of particles. To minimize the usage of computation processing power, the neighbourhood list is implemented and the system is meshed in 3D grids.

Each particle is spatially sorted into an $XMSize \times YMSize \times ZMSize$ grid with a reference number, and the next step is to find and track each particle during simulation process. For the neighbourhood list defined in the simulation platform, particles within 3 mesh grids are considered to be neighbours, i.e. for a particle of interest, search pattern for other particle is 3 mesh grids forward and 3 mesh grids backward in all xyz axes. After the search process, the distance between particles and then interaction between particles are calculated.

3.2.3.2 Interaction modelling

The details of calculating the main interaction force are discussed as above. For this DEM based simulation platform, other forces such as gravitation, buoyancy force are also included as constant linear force vector acting at the centre of each particle.

3.2.3.3 Determining each particle's parameters

Particle motion is determined by applying Newton's second law as follows.

$$m_p \frac{dU}{dt} = F \quad (3-27)$$

where m_p is the mass of particle, F is the summation of all forces act on the particle, and U is the velocity vector of particle.

With the assumption that the force acting on a particle is constant over one time step, t_d , the velocity vector of each particle is then determined by

$$U_{t+t_d} = U_t + \frac{F}{m_p} t_d \quad (3-28)$$

and the coordinates at the end of time step are then determined using an explicit numerical integration method, which is given as follows

$$r_{t+t_d} = r_t + 0.5t_d(U_{t+t_d} + U_t) \quad (3-29)$$

where r_t is the coordinates of particle at time t .

3.2.3.4 Updating system

Timestamp is recorded, and data of particle's velocities and coordinates are written into specific data files for a completed simulation time step. After that, system update working starts, which includes using the velocity and

coordinates calculated from last time step as initial values for integration in new time step, and sorting all particles into mesh system with new reference particle numbers.

3.3 DATA POST-PROCESSING TECHNIQUE

3.3.1 Data Read Software Development

A large number of data such as velocities, coordinates of each single particle at every sample time step, and forces acting on each single particle at every sample time step are generated during a simulation process, and output into different preset data files. As is mentioned above, the simulation data are output with binary format and cannot be directly read from text based program. And also in order to analyse particle's movement quantitatively, simulation data of any certain time are required. A data read software is developed to meet this need. The GUI of the data read software is shown in Figure 3-3. Firstly, select a simulation data file of .prn extension as the input file, and create a .txt file as output file. Secondly, input the data read parameters including the total number of particles in the simulation process, the start time T_1 and end time T_2 of select data read period, and the sample data read time step T_s . Thirdly, select objective particles whose simulation data are chosen to read into data read output files. At last, click '!Start' button to read binary data and write them into decimal .txt file.

There are three options designed to select objective particles:

- I. Read all particles' data.
- II. Input the total number of particles, 20 for example, that are required to read data, and click 'randomly select' button to randomly select 20 particles, with their particle numbers outputting into a particle number file.

- III. Read the data of certain particle number. For example, input number '5' in the box next to 'Select ONE', the data of particle number 5 will be read and written into .txt data file.

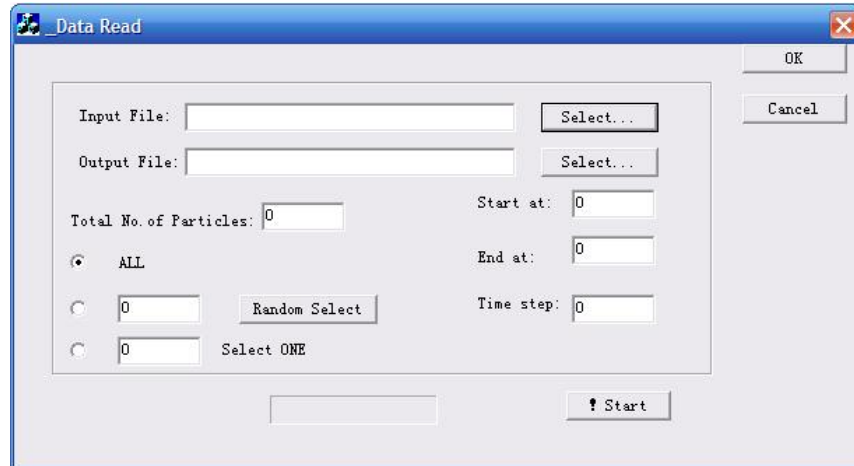


Figure 3-3. Data read software GUI.

The flowchart of the data read program is shown in Figure 3-4, and the main functions of the data read program are listed in Table 3-3.

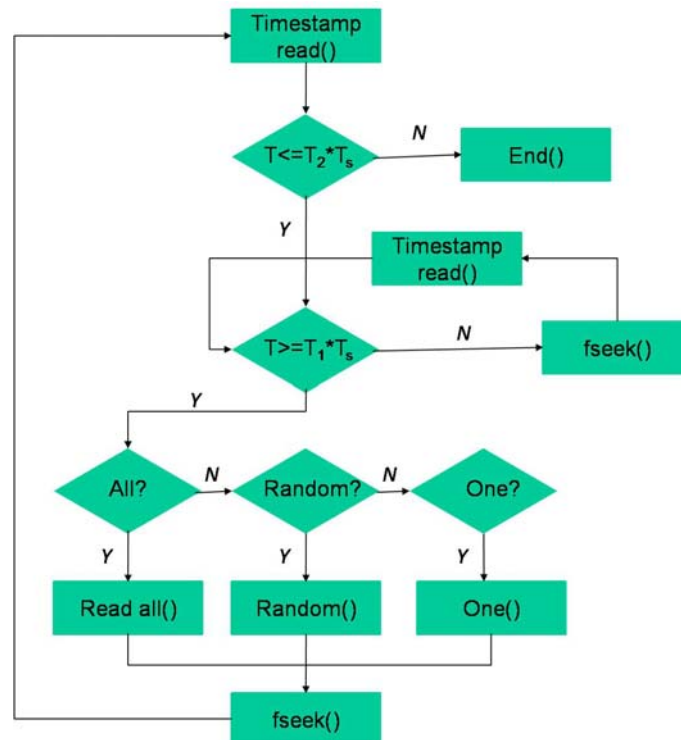


Figure 3-4 Flowchart of Data read program.

Table 3-3. Main functions in data read program.

Function Name	Function
Timestamp read()	Get the current timestamp
Read all()	Read all particles data into decimal .txt file
Random()	Read randomly selected particles data into decimal .txt file
One()	Read one appointed particle data into decimal .txt file
fseek()	Locate the data read point to the following timestamp
End()	End the data read process

By using the data read software, the large volume simulation data which are all in binary format can be converted to decimal format and output for data analysis. However, the data post-processing method introduced above is not direct-viewing for simulation process at particular time step. And thus, off-line data 3D demonstration program is developed, as stated in the following section.

3.3.2 Off-line Data 3D Demonstration

As mentioned above, the data files created during simulation are with configuration of a run-timestamp followed by the particle's xyz coordinates, which are all in binary format. Here to demonstrate simulation off-line data, the backbone program of the simulation platform 'SimCos' is simplified. Here only the environment settings of 'SimCos' are used, with particles and suspension container through OpenGL drawing. And instead of checking interaction between particles, calculating forces acting on particles, particles' velocities and consequently coordinates, the particle coordinates data file is used as direct input. There are three different ways for off-line data 3D demonstration, as listed below:

- I. To demonstrate snapshots of simulation process at any particular time step. By setting a specific time step, the particles' coordinates at this time step are input and a snapshot of simulation process at this time step is displayed.
- II. To demonstrate the snapshot of any particular particles. The particles' numbers are displayed on the surface of the particles and particles of no interest are set to disappear. In this way, it is much more clear to check if two particles interact with each other, through a vivid 3D view.
- III. To demonstrate simulation process in a larger time-scale. As the time step used in simulation process is very small, it is difficult to observe particle movement during each simulation time step. By setting a large data sample time step, 10 times simulation time step for example, the particle movement can be tracked in an easier and efficient way when reading off-line simulation coordinates data file.

CHAPTER FOUR

DIFFUSION COEFFICIENT ANALYSIS OF BROWNIAN PARTICLE

CHAPTER FOUR

DIFFUSION COEFFICIENT ANALYSIS OF BROWNIAN PARTICLE

4.1 INTRODUCTION

Brownian motion, starting with the seminal work of A. Einstein and M. Smoluchowski (Einstein, 1905, Smoluchowski, 1906), has been the subject of intense research over 100 years (Chandrasekhar, 1943, Hanggi and Marchesoni, 2005), from polymer physics to biophysics (Reimann, 2002, Frey and Kroy, 2005, Sokolov and Klafter, 2005), aerodynamics, and statistical mechanics. As a simple stochastic process, Brownian motion can be modelled to mathematically characterize the random diffusion of free colloidal particles suspended in fluids. Understanding and controlling the diffusion of colloidal particles in fluids are the main challenges in cell biology (Bareford and Swaan, 2007), catalytic reactions occurring in porous media (Daniel and Astruc, 2004) and separation techniques of size-dispersed particles on micro or nanoscale (Corma, 1997).

Here we focus on the problem of the diffusion of Brownian particles in confined geometries (Burada et al., 2009). When a colloidal particle suspended in a quiescent fluid approaches a planar wall, the dynamics of the particle are different from the bulk dynamics due to hydrodynamic interactions between the colloidal particle and the wall. Brenner and Goldman et al. (Brenner, 1961, Goldman, 1967) predicted that the hydrodynamic mobility of a particle perpendicular and parallel to a planar wall tended to be zero as the separation distance between particle and wall became infinitely small, and the diffusion coefficients perpendicular and parallel to the wall were greatly reduced when the particles were close enough to the wall, i.e. within distances comparable to or less than their radius. For decades, Brownian motion of spherical colloidal particles in the vicinity of a wall has been extensively studied, both theoretically (Faxen, 1923, Brenner, 1961,

Brenner, 1962) and experimentally (Feitosa and Mesquita, 1991, Faucheux and Libchaber, 1994). An optical trapping (Grier, 1997, Neuman and Block, 2004) technique has been applied to measure the nanoscale displacements of colloidal particles and analyse diffusion coefficient under geometry confinement. Combining optical trapping with total internal reflection microscopy, Walz and Suresh (1995) studied the sedimentation of spherical colloidal particles and results were in very good agreement with Brenner's prediction. Combining optical tweezers with a video microscopy experiment, Lin et al. (2000) showed that the particles movement agreed with Brenner's prediction in both perpendicular and parallel directions, when there is no electrostatic interaction in the system. A recent study which applied fluorescence microscopy in three dimensional particle tracking (Banerjee and Kihm, 2005) showed that Brenner's predictions for particle mobility parallel to a planar wall are valid for colloids. In a typical experiment, trajectories of tracer particles were recorded and analysed in terms of position correlations or mean square displacement. From those data, information on the size of the diffusing objects or on their interactions with the surrounding medium can be extracted (Gambin et al., 2006). Resonance enhanced dynamic light scattering was firstly used to probe the dynamic phenomena of particle diffusion in the fluid close to a gold surface, and the possibility to measure the diffusion of small, weakly scattering PS colloids ($R_h = 20$ nm) was demonstrated (Plum et al., 2009). However, this experimental study of particle diffusion did not include non-hydrodynamic effects such as electrostatic interaction and hydration force.

However, there are some shortcomings in the experimental work and previous numerical simulations. Firstly, it cannot be realized through experiment to put a particle closely enough towards the wall, and previous works only consider distances between particle and wall down to 1 μm (Lin et al., 2000). Secondly, there is fluctuation of the initial position of the particle for each experimental sample and the speed of the image capture is limited by the hardware, so that the displacement of the particle for every time step

cannot be precisely obtained. Thirdly, many other interaction other than hydrodynamic drag force and Brownian force were not included in previous numerical models and experiments for simplifying the complexity of the system (Carbajal-Tinoco et al., 2007). And it is experimentally impossible to switch on or off each interaction force separately.

In this chapter, a series of simulations are set up in a modelled geometry, where a spherical colloidal particle is in the vicinity of a solid horizontal wall. The Brownian motion either perpendicular or parallel to the wall are studied and the diffusion coefficient related to the varying distance between particle and wall for different particle size and different charge systems are analysed.

4.2 THEORETICAL BACKGROUND

As stated in Chapter 3, a colloidal particle with a radius of R , moving freely with velocity U in a quiescent medium of viscosity η , experiences a hydrodynamic drag force opposite to its direction of motion,

$$F_d = -6\pi\eta RU \quad (4-1)$$

The diffusion coefficient D_0 of the sphere is given by the Stokes-Einstein relation

$$D_0 = \frac{k_B T}{6\pi\eta R} \quad (4-2)$$

where k_B is the Boltzmann constant and T is the temperature of the system.

If the colloidal particle moves in the vicinity of a planar wall, the surrounding fluid will cause a hydrodynamic interaction with the interface. The drag force acting on the particle is larger than in the bulk, and its diffusion is hindered by hydrodynamic interaction between particle and wall, and therefore its diffusion coefficient is smaller than in the bulk. The motion of the particle

becomes anisotropic as the drag force parallel to the wall is less than that perpendicular to the wall. The expressions for the parallel and perpendicular components of the drag force are conventionally represented by incorporating correction factors λ_{\perp} and λ_{\parallel} . These expressions are

$$F_{\perp} = F_d \lambda_{\perp} = -6\pi\eta RU \lambda_{\perp} \quad (4-3)$$

and

$$F_{\parallel} = F_d \lambda_{\parallel} = -6\pi\eta RU \lambda_{\parallel} \quad (4-4)$$

Brenner (1961) calculated the exact solution of λ_{\perp} for a spherical particle moving perpendicular to the wall,

$$\lambda_{\perp}^{-1} = \frac{D_{\perp}}{D_0} = \left\{ \frac{4}{3} \sinh \alpha \sum_{n=1}^{\infty} \frac{n(n+1)}{(2n-1)(2n+3)} \left[\frac{2 \sinh(2n+1)\alpha + (2n+1) \sinh 2\alpha}{4 \sinh^2(n+\frac{1}{2})\alpha - (2n+1)^2 \sinh^2 \alpha} - 1 \right] \right\}^{-1} \quad (4-5)$$

where $\alpha = \operatorname{arccosh} \left(\frac{y}{R} \right) = \ln \left[\frac{y}{R} + \sqrt{\left(\frac{y}{R} \right)^2 - 1} \right]$, and y is the shortest distance

between the particle centre and wall.

However, there is no exact analytical expression for λ_{\parallel} . The commonly applied approximation is due to Faxén (1923), including terms of order $(R/y)^5$, using the so-called ‘method of reflections’,

$$\lambda_{\parallel}^{-1} = \frac{D_{\parallel}}{D_0} = 1 - \frac{9}{16} \left(\frac{R}{y} \right) + \frac{1}{8} \left(\frac{R}{y} \right)^3 - \frac{45}{256} \left(\frac{R}{y} \right)^4 - \frac{1}{16} \left(\frac{R}{y} \right)^5 + O \left(\frac{R}{y} \right)^6 \quad (4-6)$$

Using the same method, the approximation form of λ_{\perp} is inclusive of terms of order $(R/y)^3$,

$$\lambda_{\perp}^{-1} = \frac{D_{\perp}}{D_0} = 1 - \frac{9}{8} \left(\frac{R}{y} \right) + \frac{1}{2} \left(\frac{R}{y} \right)^3 + O \left(\frac{R}{y} \right)^4 \quad (4-7)$$

Experimental evidence for this wall effect is comparably recent and consists mostly in measuring changes in the diffusion coefficient of a micro-sized spherical particle moving towards a surface (Carbajal-Tinoco et al., 2007, Schaffer et al., 2007).

4.3 MODEL ESTABLISHMENT

Based on the established simulation platform SimCos (Fang and Li, 2009), the interaction model is described in Chapter 3. And here hydration force, DLVO forces, hydrodynamic drag force and Brownian force are implemented to model particle diffusion phenomena. And for a colloid particle suspended in an aqueous solution in the vicinity of a planar wall, the hydrodynamic drag force is revised as follows.

4.3.1 Hydrodynamic Drag Force Revisited

When a particle is suspended in an aqueous solution, its hydrodynamic drag force in the form of Equation 4-1 changes to

$$F_d = -6\pi\eta R_{HYD}U \quad (4-8)$$

where R_{HYD} is the hydrodynamic radius of particle, with 7 nm thickness hydration layer. And the expressions for the parallel and perpendicular components of the drag force in the vicinity of planar wall are

$$F_{\perp} = F_d \lambda_{\perp} = -6\pi\eta R_{HYD}U \lambda_{\perp} \quad (4-9)$$

and

$$F_{//} = F_d \lambda_{//} = -6\pi\eta R_{HYD} U \lambda_{//} \quad (4-10)$$

Here comes the selection of order number in Equation 4-5, Equation 4-6 and Equation 4-7 for the correction factors λ_{\perp} and $\lambda_{//}$, respectively, as shown in Table 4-1.

Table 4-1. Stokes' Laws correction factor for a planar wall, Equation 4-5~Equation 4-7.

α	Distance ratio (y/R)	Parallel correction factor ($\lambda_{//}$)				Perpendicular correction factor (λ_{\perp})			
		1st	3rd	4th	5th	1st	3rd	n=1	n=3
				(Equation 4-6)		(Equation 4-7)		(Equation 4-5)	
0	1	2.2857	1.7778	2.5859	3.0843	-8	2.6667	∞	∞
0.5	1.1276	1.9954	1.6997	2.0850	2.2455	429.41	2.8486	8.0122	8.8403
1	1.5431	1.5736	1.4937	1.5662	1.5839	3.6909	2.4569	2.7696	2.9882
1.5	2.3524	1.3143	1.2979	1.3076	1.3091	1.9166	1.7852	1.7515	1.8308
2	3.7622	1.1758	1.1726	1.1738	1.1739	1.4266	1.4077	1.3822	1.4120
2.5	6.1323	1.1010	1.1003	1.1005	1.1005	1.2247	1.2214	1.2108	1.2219
3.0	10.068	1.0592	1.0590	1.0591	1.0591	1.1258	1.1252	1.1211	1.1252
5.0	74.210	1.0076	1.0076	1.0076	1.0076	1.0154	1.0154	1.1211	1.1252
12	81377	1	1	1	1	1	1	1.1211	1.1252

So, for parallel correction factor, 5th order approximation is used:

$$\lambda_{//}^{-1} = \frac{D_{//}}{D_0} = 1 - \frac{9}{16} \left(\frac{R}{y} \right) + \frac{1}{8} \left(\frac{R}{y} \right)^3 - \frac{45}{256} \left(\frac{R}{y} \right)^4 - \frac{1}{16} \left(\frac{R}{y} \right)^5 \quad (4-11)$$

For perpendicular correction factor with the approximation form Equation 4-7, with the distance ratio decreasing, the perpendicular correction factor

increases non-monotonously and even changes to negative value. While with exact solution Equation 4-5, the perpendicular correction factor increases monotonously and up to ∞ when the distance ratio decreases to 1, which is a perfect boundary condition. Comparing the perpendicular correction factor value of 1st ($n=1$) and 3rd ($n=3$) order in Equation 4-5, the difference is insignificant as shown in Table 4-1. Since the computational effort is lower with 1st order equation, the exact solution with 1st order approximation is used to calculate perpendicular correction factor:

$$\lambda_{\perp}^{-1} = \frac{D_{\perp}}{D_0} = \left\{ \frac{4}{3} \sinh \alpha \sum_{n=1}^{\infty} \frac{n(n+1)}{(2n-1)(2n+3)} \left[\frac{2 \sinh(2n+1)\alpha + (2n+1) \sinh 2\alpha}{4 \sinh^2(n + \frac{1}{2})\alpha - (2n+1)^2 \sinh^2 \alpha} - 1 \right] \right\}^{-1} \quad (4-12)$$

$$\text{where } \alpha = \arccos h\left(\frac{y}{R}\right) = \ln \left[\frac{y}{R} + \sqrt{\left(\frac{y}{R}\right)^2 - 1} \right], n=1.$$

When a particle is suspended in an aqueous solution, for the y/R or R/y factor used to calculate perpendicular and parallel correction factors, the definitions of R and y are still ambiguous, i.e. R is a particle bare radius or hydrodynamic radius R_{HYD} , and y is a distance from the centre of the particle to the hydration surface or bare surface of the wall. As shown in Figure 4-1, since both particle and wall are incompressible, with boundary condition $y/R = 1$, $\lambda = \infty$ (Brenner, 1961), R is the particle bare radius and y is the distance from the centre of the particle to the wall bare surface.

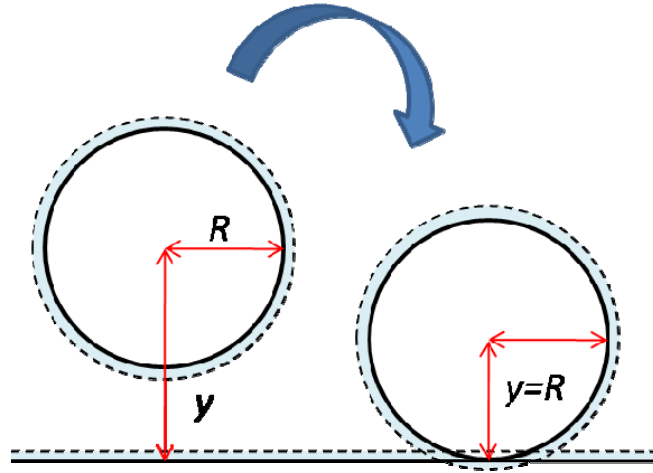


Figure 4-1. Illustrative sketch of relation between y and R .

4.3.2 Simulation Method

The diffusion coefficient of a free Brownian particle in one dimension, e.g., in the x direction, D_{0-x} is defined by (Hunter, 2001)

$$\langle \Delta x^2(t) \rangle = 2D_{0-x}t \quad (4-13)$$

The value of D_{0-x} is obtained as follows. First, particle displacements $\Delta x(t)$ corresponding to each sample time step for all samples are recorded. Then the mean square displacement in the x direction $\langle \Delta x^2(t) \rangle$ is derived by calculating the variance of $\Delta x(t)$ at each sample time step. At last D_{0-x} is determined from the linear fit of $\langle \Delta x^2(t) \rangle$ to t (Equation 4-13). The same method is used to derive the diffusion coefficients along the y and z directions.

For each simulation case, the diffusion coefficient D_0 of a free Brownian particle in bulk suspension is derived first. And through comparison to experiment (Lin et al., 2000) and theory, the simulation model is validated. And then investigate the diffusion coefficient by including different interaction forces and geometry confinement effect.

Data read software and video snapshot (Fang and Li, 2009) are the post-processing technique used to demonstrate diffusion coefficient real time process or display off-line data while preset a sample time step to enlarge the microscopic view.

Below the selection of the simulation time step t , total run time t_{all} for a trial sample, time step Δt to calculate Brownian force and the sample number N during the simulation process are investigated.

As mentioned in Chapter 3, for colloidal particle suspended in aqueous solution, its Brownian motion is described by Langevin equation,

$$m_p \frac{dU}{dt} + BU = F_B \quad (4-14)$$

where $B = 6\pi\eta R$. With boundary condition: $t = 0, r = 0; t = -\infty, U = 0$, and the system being in thermodynamic equilibrium, i.e.

$$\frac{1}{2} m_p \langle U^2 \rangle = \frac{n}{2} k_B T \delta \quad (4-15)$$

Taking the Brownian motion in x direction as an example, Equation 4-14 can be substituted as

$$m_p \Delta x \cdot \frac{d^2 \Delta x}{dt^2} + B \Delta x \cdot \frac{d \Delta x}{dt} = \Delta x \cdot F_B \quad (4-16)$$

$$\text{As } \frac{d(\Delta x^2)}{dt} = 2 \Delta x \cdot \frac{d \Delta x}{dt} \quad (4-17)$$

$$\frac{d^2(\Delta x^2)}{dt^2} = 2 \Delta x \cdot \frac{d^2 \Delta x}{dt^2} + 2 \cdot \left(\frac{d \Delta x}{dt} \right)^2 \quad (4-18)$$

It comes

$$\Delta x \cdot \frac{d^2 \Delta x}{dt^2} = \frac{1}{2} \cdot \frac{d^2 (\Delta x^2)}{dt^2} - \left(\frac{d \Delta x}{dt} \right)^2 \quad (4-19)$$

So that Equation 4-15 takes the form:

$$\frac{1}{2} m_p \frac{d^2 (\Delta x^2)}{dt^2} + \frac{1}{2} B \frac{d (\Delta x^2)}{dt} - m_p \left(\frac{d \Delta x}{dt} \right)^2 = \Delta x \cdot F_B \quad (4-20)$$

Averaging both sides of Equation 4-20 over many particle samples (averaging over an ensemble), or over different initial times, it comes

$$\frac{1}{2} m_p \frac{d^2}{dt^2} \langle \Delta x^2 \rangle + \frac{1}{2} B \frac{d}{dt} \langle \Delta x^2 \rangle - 2 \left\langle \frac{1}{2} m_p U^2 \right\rangle = 0 \quad (4-21)$$

Combining with Equation 4-15, Equation 4-21 becomes

$$m_p \frac{d^2 u}{dt^2} + B \frac{du}{dt} = 2k_B T \quad (4-22)$$

where $\langle \Delta x^2 \rangle$ is denoted by u .

The solution to Equation 4-22 is

$$\langle \Delta x^2 \rangle = u = \frac{2k_B T}{B} \left[t + \tau_R (e^{(-t/\tau_R)} - 1) \right] \quad (4-23)$$

where τ_R is the relaxation time, with a form of

$$\tau_R = \frac{m_p}{6\pi\eta R} \quad (4-24)$$

At a very short time (this short time t , molecular time $\ll t \ll \tau_R$, is of the order of the time between successive collisions between the Brownian particle and the molecules of the surrounding fluid), relative to times between collisions with molecules, the particle velocity is the thermal velocity as

determined at equilibrium (Equation 4-15). In Equation 4-23, at short time, $t \ll \tau_R$, e.g. $t = 0.1\tau_R$, it is possible to expand the exponential,

$$\langle \Delta x^2 \rangle \approx \frac{2k_B T}{B} \left[t + \tau_R \left(1 - \frac{t}{\tau_R} + \frac{t^2}{2\tau_R^2} - 1 \right) \right] = \frac{k_B T}{m_p} t^2 \quad (4-25)$$

Namely, at a short time, relative to times between collisions, the particle moves as a free particle with constant velocity.

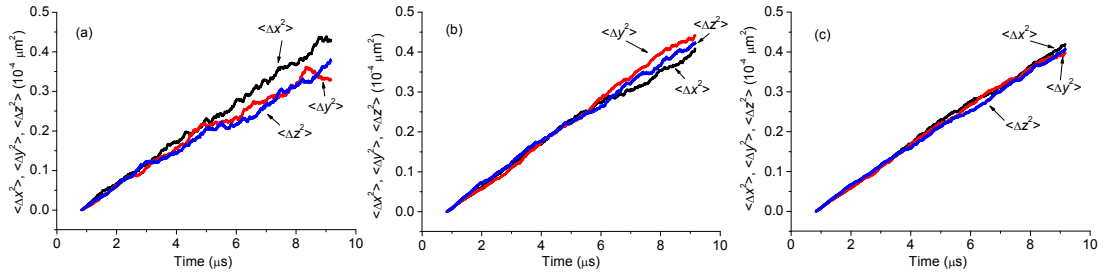
In Equation 4-23, at long enough time $t_{all} \gg \tau_R$, e.g. $t_{all} = 10^3 \tau_R$, the exponential decays away, and τ_R can be neglected compared to t_{all} , so it comes to Equation 4-13. The time step Δt used to calculate Brownian force is determined through a trial simulation case, where a colloidal particle is subject to free Brownian motion in the bulk. The key parameters included in the model are listed in Table 4-2, and the simulation results are listed in Table 4-3. Comparing the calculated diffusion coefficient got from simulation with theoretical value which is $2.04 \times 10^{-12} \text{ m}^2 \text{ s}^{-1}$ got from Equation 4-2, the appropriate time step Δt is set to be 0.50 ns to calculate Brownian force.

Table 4-2. Key simulation parameters of particle diffusion model.

Variables	Base values
Particle radius (nm), R	100
Particle density (kg m^{-3}), ρ_p	2200
Fluid density (kg m^{-3}), ρ_f	1000
Fluid viscosity (Pa s), η	0.001
Time step (ns), t_d	0.5

Table 4-3. Free diffusion coefficient of particle in bulk.

Δt (ns)	0.40	0.43	0.45	0.50
Diffusion Coefficient D_0 ($\times 10^{-12} \text{ m}^2 \text{ s}^{-2}$)	2.47	2.21	2.05	2.04

Figure 4-2. Mean square displacements $\langle \Delta x^2 \rangle$, $\langle \Delta y^2 \rangle$ and $\langle \Delta z^2 \rangle$ as functions of time.

(Note: (a) for 200 samples, (b) for 500 samples and (c) for 1000 samples.)

Theoretically, for a colloidal particle subjected to free Brownian motion, the mean square displacements in x , y and z direction should be the same. This criterion is used to determine an appropriate sample number used to calculate the diffusion coefficient.

Comparing the results obtained from different samples (Figure 4-2), the appropriate sample number N used to calculate the diffusion coefficient is chosen to be 1000.

4.4 SIMULATION RESULTS AND DISCUSSIONS

4.4.1 Model Validity

Lin et al. (Lin et al., 2000) used video microscopy combined with optical tweezers to measure the Brownian motion of an isolated uncharged PMMA sphere suspended in a 30% (by weight) sucrose solution confined between two parallel walls. The optical tweezers were used to control the relative

distance between a sphere undergoing Brownian motion and the wall, as is illustrated in Figure 4-3.

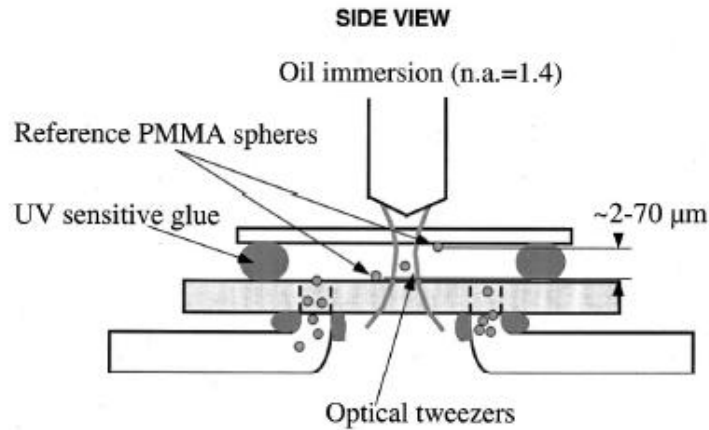


Figure 4-3. Schematic diagram of an isolated PMMA sphere confined in a thin glass cell.

(Note: The location of the sphere with respect to the walls is manipulated by optical tweezers. The spheres stuck to the wall are used as reference points to determine the cell spacing and the location of the moving sphere relative to the cell walls (Lin et al., 2000).)

Table 4-4 lists the key parameters used in the experiment. Figure 4-4 is the experimental results of a particle moving near one planar wall. The experimental data agree with the theoretical prediction within the experimental precision.

Table 4-4. Key parameters used in the experiment (Lin et al., 2000).

Variables	Base values
Particle radius (nm), R	466
Particle density (kg m^{-3}), ρ_p	1200
Fluid density (kg m^{-3}), ρ_f	1130
Fluid viscosity (Pa s), η	0.003
Time step (ns), t_d	0.5

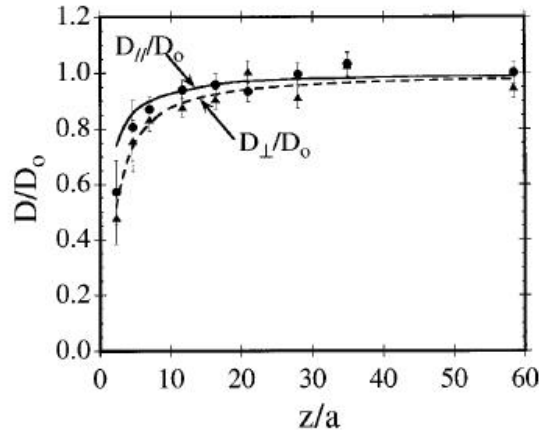


Figure 4-4. The measured diffusion coefficient D_{\parallel} (solid circles) and D_{\perp} (solid triangles) for an isolated sphere near one planar wall, normalized by D_0 .

(Note: The solid line is the theoretical prediction for D_{\parallel} / D_0 , calculated (not fitted) using Equation 4-6, and the dashed line is the theoretical prediction for D_{\perp} / D_0 , calculated (not fitted) using Equation 4-7 (Lin et al., 2000).)

Since the use of uncharged particle, the DLVO force between particle and wall is neglected. However, as this is a sucrose solution, the existence of hydration force and hydration layer in this system is still ambiguous. Below simulation case studies are carried out to explore if there is a hydration layer existing outside the particle in this system.

First, the uncharged particle is treated as bare particle without any hydration layer outside (CASE I). In this case, only the Brownian force and hydrodynamic drag force take effect. Then, a 7 nm thickness hydration layer is included outside the bare particle, and hydration effect is taken into account correspondingly (CASE II). Finally, the particle is treated with a volume expansion effect, which is an important property of polymer (CASE III). The relaxation time τ_R calculated from Equation 4-24 is 17.3 ns, and the theoretical diffusion coefficient calculated from Equation 4-2 is $1.47 \times 10^{-13} \text{ m}^2 \text{ s}^{-1}$. The simulation time step is set to be 0.5 ns, the data sampling time is set to be 10 ns and the simulation is run for 10 μs . The simulation results of CASE I to III, compared with theoretical prediction and experimental data are shown in Table 4-5. As shown in Table 4-5, the simulation values are smaller

than the theoretical prediction values, especially when y/R approaches to 1. The reason for this systematic deviation is that the distance of the particle from the wall varies with time as a result of Brownian motion of the particle, while the calculated diffusion coefficient is a value for initial particle-wall separation.

Table 4-5. D/D_0 for a particle near a planar wall. Comparison among theoretical prediction, experimental data, and simulation CASE I, II and III.

y/R	D_{\perp} / D_0					D_{\parallel} / D_0				
	theory	experiment	I*	II*	III*	theory	experiment	I*	II*	III*
2.3	0.56	0.48	0.31	0.35	0.34	0.76	0.57	0.58	0.59	0.65
4.7	0.78	0.76	0.57	0.66	0.68	0.88	0.81	0.77	0.78	0.85
7.0	0.85	0.84	0.68	0.69	0.81	0.92	0.87	0.91	0.84	0.86
12	0.91	0.88	0.75	0.86	0.87	0.95	0.94	0.90	0.95	0.95
16	0.93	0.91	0.89	0.79	0.98	0.96	0.93	0.92	0.92	0.98
21	0.95	1.0	0.90	1.0	1.0	0.97	0.93	0.95	0.94	1.0
28	0.96	0.91	0.92	0.94	1.0	0.98	1.0	0.97	0.99	0.99
35	0.97	1.0	0.95	0.95	0.98	0.98	1.0	1.0	1.0	1.1
58	0.98	0.95	0.99	0.99	0.99	0.99	1.0	0.99	1.0	1.1

(Note: I*: CASE I, bare particle without hydration layer outside; II*: CASE II, bare particle with a 7 nm thickness hydration layer outside; III*: CASE III, bare particle with a volume expansion effect.)

The results data got from the above three cases are fitted with third order exponential decay function, as shown in Table 4-6 and Figure 4-5(a). From Table 4-6, the fit model parameters between CASE III and experiment match the best. In order to compare the match degree between three simulation models and the experiment, fit comparison work were done, and the P-value testing the statistical significance are 0.8392, 0.9933 and 0.9952, respectively. So it comes to the conclusion that by including a volume

expansion effect and correspondingly including hydration effect for particle suspended in sucrose solution, the results agree the best with the theoretical prediction and experiment data, compared to the other two hydration layer treatment of particle in this system, as shown in Figure 4-5.

Table 4-6. Explicit function of D_{\perp} / D_0 for a particle near a planar wall.

D_{\perp} / D_0	$A_0 + A_1 e^{-\frac{1}{a_1}(y/R)} + A_2 e^{-\frac{1}{a_2}(y/R)} + A_3 e^{-\frac{1}{a_3}(y/R)}$						
	A_0	A_1	a_1	A_2	a_2	A_3	a_3
experiment	0.96739	-1.02363	1.0446	-1.14629	1.04494	-0.33342	7.70815
I	1.04684	-1.75345	0.96051	-0.14523	65.55151	-0.57721	8.24893
II	0.99437	-0.36484	10.84212	-0.1677	10.83819	-15.94559	0.53307
III	0.99834	-1.23936	1.0458	-0.75439	1.04637	-0.64154	6.00151

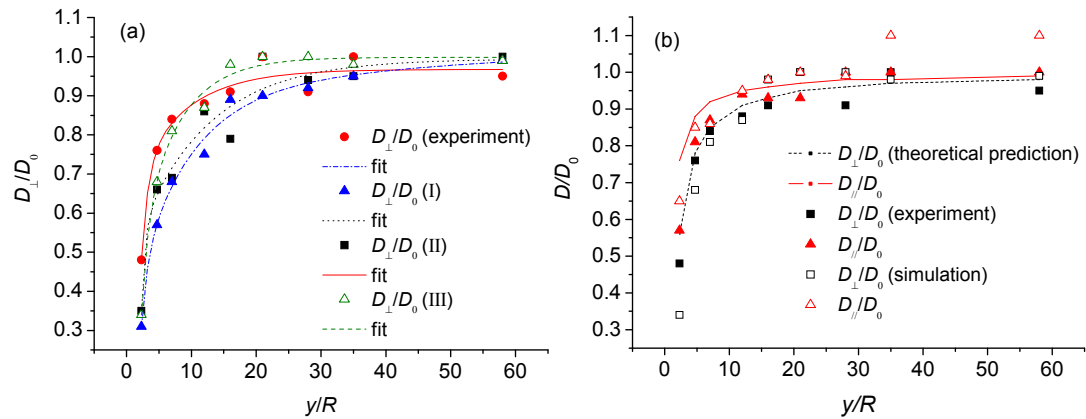


Figure 4-5. D/D_0 for a particle near a planar wall. Comparison among theoretical prediction, experimental data, and simulation CASE I, II and III.

(Note: (a) The comparison of perpendicular diffusion coefficients D_{\perp} normalized by D_0 , among experimental data (solid circles), simulation CASE I for bare particle (solid triangles), simulation CASE II for particle inclusive of hydration layer (solid squares), and simulation CASE III for particle inclusive of volume expansion effect (open triangle). The solid line, the dot-dash line, the dot line, and the dash line are fitted with third order exponential decay function for experimental data, simulation values for bare particle, simulations values for particle inclusive of hydration layer, and simulation values for particle inclusive of volume

expansion effect, respectively. And (b) the simulation value of diffusion coefficients D_{\perp} and $D_{//}$ for an isolated spherical colloidal particle near one horizontal planar wall, normalized by D_0 . For comparison with theoretical prediction value using Equation 4-11 and Equation 4-12 and the experimental data (Lin et al., 2000).)

4.4.2 The Comprehensive Study of Hindered Diffusion

Here we consider the problem of a spherical colloidal particle of radius R moving towards a planar surface, $y = 0$, with its initial velocity U (illustrated in Figure 4-6). Both the particle and plane are silica with 7 nm hydration layer thickness. Figure 4-7 shows a snapshot of this particle diffusion simulation process.

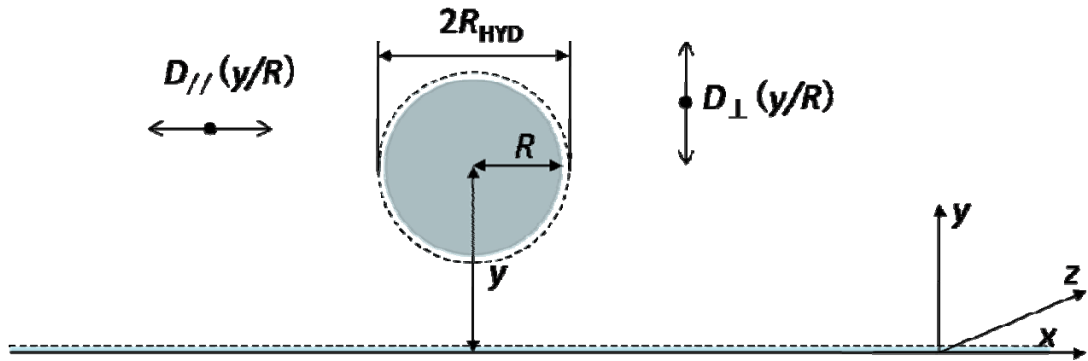


Figure 4-6. Scheme of the particle diffusion system.

(Note: A spherical colloidal particle moving in the vicinity of a planar wall at $y = 0$, with y being the particle-wall separation. The diffusion of the particle parallel to the wall $D_{//}$ differs from that perpendicular to the wall D_{\perp} .)

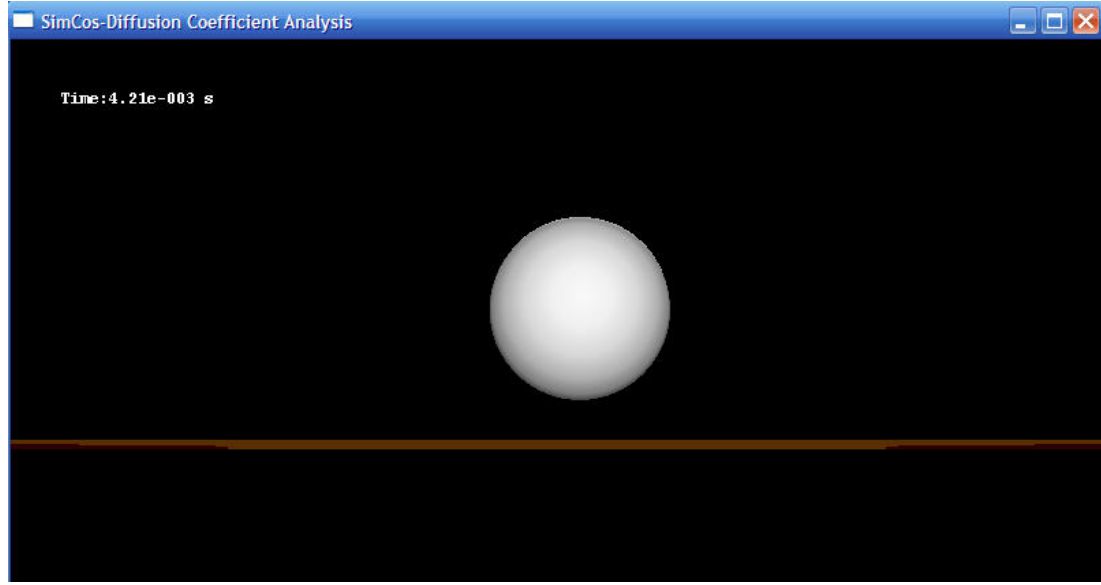


Figure 4-7. Snapshot of simulation process for particle diffusion in the vicinity of a planar wall.

4.4.2.1 *Neutral system*

Firstly, we present simulation case where an uncharged particle is suspended in aqueous solution, moving near a wall. The parameters used in this simulation are the same as shown in Table 4-2.

Before running the simulation system, initialization work is required, which are listed as follows: The particle's initial velocity U is determined by its thermodynamic equilibrium (Equation 4-15), the relaxation time τ_R calculated from Equation 4-24 is 5.01 ns and the theoretical diffusion coefficient calculated from Equation 4-2 is $2.04 \times 10^{-12} \text{ m}^2 \text{ s}^{-1}$. The simulation time step is set to be 0.5 ns, the data sampling time is 10 ns and the simulation run time is 10 μs .

At each simulation time step, the displacements of particle compared to its initial coordinates in three axes are calculated and at each data sampling time, the displacements data are output to displacements data file. At the end of the running time 10 μs , which are 2×10^4 computation cycles for a single

sample, the running time and the computation cycle counter are reset to zero, and the particle is reset with its initial velocity and position. The simulation process is terminated until the 1000 samples are all finished.

The value of diffusion coefficient $D_{//}$ in parallel direction is obtained as follows. First, the mean square displacements $\langle \Delta x^2(t) \rangle$ and $\langle \Delta z^2(t) \rangle$ are derived through calculating average square root summing value over 1000 samples. Then D_x and D_z are determined from the linear fit of $\langle \Delta x^2(t) \rangle$ and $\langle \Delta z^2(t) \rangle$ to t , respectively (Equation 4-13). And $D_{//}$ is the average of D_x and D_z . The same method is used to derive the diffusion coefficient D_{\perp} in perpendicular direction. The diffusion coefficient is then normalized by dividing simulated free diffusion coefficient in bulk.

Figures 4-8 shows $\langle \Delta x^2(t) \rangle$, $\langle \Delta y^2(t) \rangle$ and $\langle \Delta z^2(t) \rangle$ as functions of t , respectively.

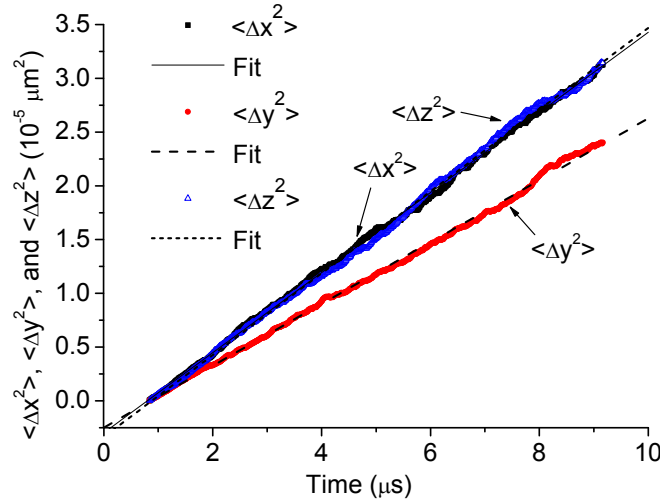


Figure 4-8. Mean square displacements $\langle \Delta x^2(t) \rangle$, $\langle \Delta y^2(t) \rangle$ and $\langle \Delta z^2(t) \rangle$ as functions of t .

(Note: The lines are fits of the data to a linear function of t (Equation 4-13).)

Note that the starting points in Figures 4-8 are not the initial coordinates. Because the initial coordinates are arbitrarily preset and here we are only interested in the relative displacement, so the initial coordinates at $t=0$ are

eliminated. Figure 4-8 indicates that the motion parallel to the confined wall (the x-z plane) is isotropic and the motion perpendicular to the wall is hindered to some extent. This is because the confined wall is placed horizontally which is perpendicular to particle diffusion in vertical y direction, and the mean square displacement perpendicular to the wall $\langle \Delta y^2(t) \rangle$ increases slower than $\langle \Delta x^2(t) \rangle$ and $\langle \Delta z^2(t) \rangle$, which are parallel to the wall.

The results of diffusion coefficients are shown in Table 4-7 and Figure 4-9. As expected, both perpendicular and parallel diffusion coefficients D_{\perp} and D_{\parallel} decrease as the distance between particle and wall decreases, and for the same value of y/R , the perpendicular diffusion coefficient D_{\perp} is smaller than the parallel diffusion coefficient D_{\parallel} .

Table 4-7. D/D_0 for uncharged particle suspended in neutral aqueous system near a planar wall. Comparison among theoretical prediction and simulation results.

y/R	D_{\parallel} / D_0		D_{\perp} / D_0	
	theory	simulation	theory	simulation
1.12	0.44	0.19	0.12	0.01
1.18	0.48	0.23	0.17	0.03
1.24	0.52	0.26	0.21	0.04
1.30	0.55	0.27	0.24	0.06
1.50	0.62	0.38	0.34	0.12
2.3	0.76	0.56	0.56	0.30
4.7	0.88	0.77	0.78	0.59
7.0	0.92	0.84	0.85	0.77
12	0.95	0.90	0.91	0.80
16	0.96	0.90	0.93	0.81

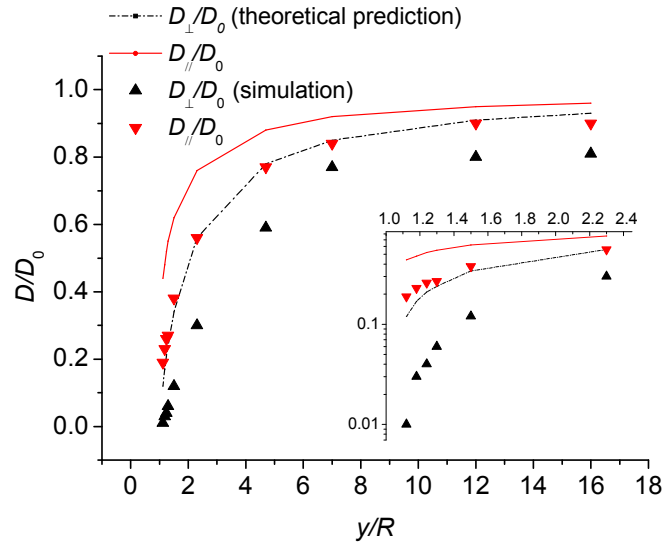


Figure 4-9. D/D_0 for uncharged particle suspended in aqueous system near a planar wall. Comparison between theoretical prediction and simulation

(Note: The solid and dashed lines are the values of D_{\parallel}/D_0 and D_{\perp}/D_0 calculated from the approximation given by Equation 4-11 and Equation 4-12, respectively. The inset with log-log scales magnifies the difference between the simulated results and theoretical values for D_{\parallel}/D_0 and D_{\perp}/D_0 when $y/R \sim 1$.)

4.4.2.2 Charged system

Then for particle and wall with -30 mV surface potential, the DLVO forces take effect when particle moves near the wall. Table 4-8 and Figure 4-10 show the comparison of resultant diffusion coefficient among theoretical prediction, simulation cases of particle in neutral system and in charged system. It shows that the parallel diffusion coefficient for a particle in charged system is larger than that in a neutral system, especially as y/R approaches 1. For perpendicular diffusion coefficient D_{\perp} , it shows that D_{\perp} can be derived from linear fit of $\langle \Delta y^2(t) \rangle$ to t (Equation 4-13) when $y/R > 2$. And compared to neutral system, it is larger in charged system as well.

Table 4-8. D/D_0 for charged particle suspended in aqueous system near a planar wall. Comparison among theoretical prediction, simulation cases of particle in neutral system and in charged system.

y/R	$D_{//} / D_0$			D_{\perp} / D_0		
	theory	simulation		theory	simulation	
		neutral	charged		neutral	charged
1.12	0.44	0.19	0.23	0.12	0.01	
1.18	0.48	0.23	0.26	0.17	0.03	
1.24	0.52	0.26	0.29	0.21	0.04	
1.30	0.55	0.27	0.35	0.24	0.06	
1.50	0.62	0.38	0.39	0.34	0.12	
2.3	0.76	0.56	0.59	0.56	0.30	0.33
4.7	0.88	0.77	0.73	0.78	0.59	0.63
7.0	0.92	0.84	0.83	0.85	0.77	0.73
12	0.95	0.90	0.90	0.91	0.80	0.87
16	0.96	0.90	1.0	0.93	0.81	0.81

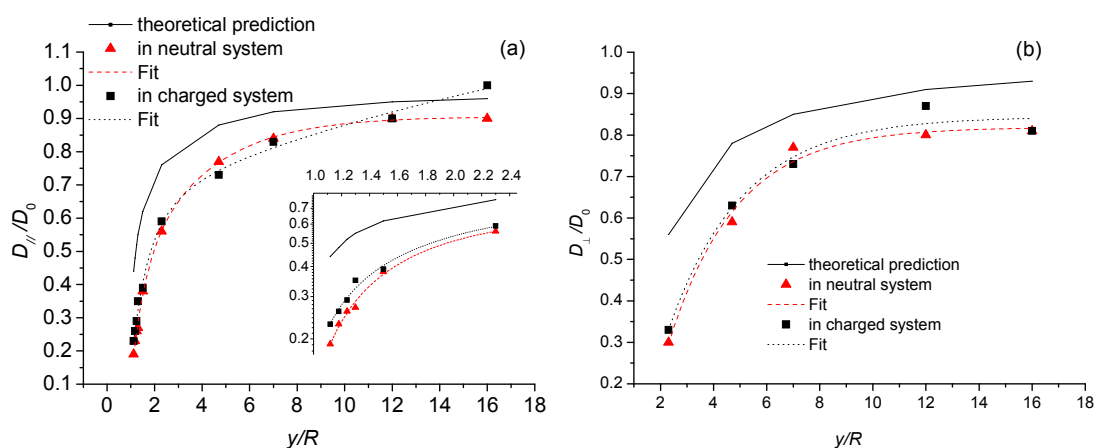


Figure 4-10. D/D_0 for charged particle suspended in aqueous system near a planar wall. Comparison among theoretical prediction, simulation cases of particle in neutral system and in charged system.

(Note: (a) The simulated parallel diffusion coefficients $D_{//}$ (solid square) normalized by D_0 , for particle in charged system near a planar wall, compared with theoretical values (solid line) and particle in neutral system (solid up-triangle). The inset with log-log scales magnifies the difference of $D_{//} / D_0$ between charged system and neutral system when $y/R \sim 1$. And (b) the simulated perpendicular diffusion coefficients D_{\perp} (solid square) normalized by D_0 , for particle in charged system near a planar wall ($y/R > 2$), compared with theoretical values (solid line) and particle in neutral system (solid up-triangle). The dash line and the dot line are fitted with third order exponential decay function for simulation values in neutral system and charged system, respectively.)

The numerical descriptions of diffusion coefficients as explicit functions of the distance between the particle and the wall are:

For neutral system,

$$\lambda_{//}^{-1} = \frac{D_{//}}{D_0} = 0.906 - 1.909e^{-1.847(y/R)} - 0.699e^{-0.345(y/R)} \quad (4-26)$$

$$\lambda_{\perp}^{-1} = \frac{D_{\perp}}{D_0} = 0.819 - 1.290e^{-0.393(y/R)} \quad (4-27)$$

For charged system, when $y/R > 2$,

$$\lambda_{//}^{-1} = \frac{D_{//}}{D_0} = 1.439 - 0.435e^{-0.680(y/R)} - 1.969e^{-1.910(y/R)} - 0.806e^{-0.037(y/R)} \quad (4-28)$$

$$\lambda_{\perp}^{-1} = \frac{D_{\perp}}{D_0} = 0.844 - 1.163e^{-0.355(y/R)} \quad (4-29)$$

However, when $y/R \sim 1$, the mean square displacement $\langle \Delta y^2(t) \rangle$ increases quadratically (Figure 4-11), which means that the perpendicular diffusion coefficient D_{\perp} cannot be derived from linear fit of $\langle \Delta y^2(t) \rangle$ to t as a constant (Equation 4-13). Because the DLVO forces which are perpendicular to the

wall dominate when particle is very close to the wall, i.e. $y/R \sim 1$, the perpendicular diffusion coefficient D_{\perp} varies following the variation of distance between particle and the wall. From Figure 4-11, it is shown that as the particle approaches to the wall, from $y/R=1.5$ to $y/R=1.18$, $\langle \Delta y^2(t) \rangle$ increases more and more quickly. And when $y/R=1.12$, where the hydration layers between particle and wall overlap, the hydration force dominates and prohibits particle diffusion which results in $\langle \Delta y^2(t) \rangle$ decrease.

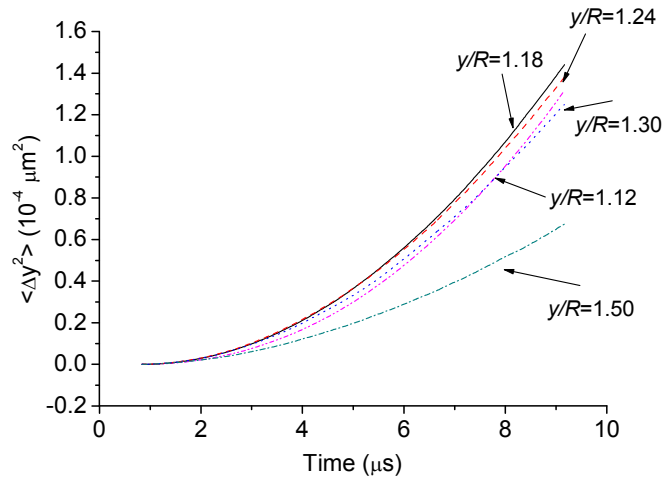


Figure 4-11. Mean square displacements $\langle \Delta y^2(t) \rangle$ as a function of t , for particle of radius 100 nm in charged system near a planar wall ($y/R \sim 1$).

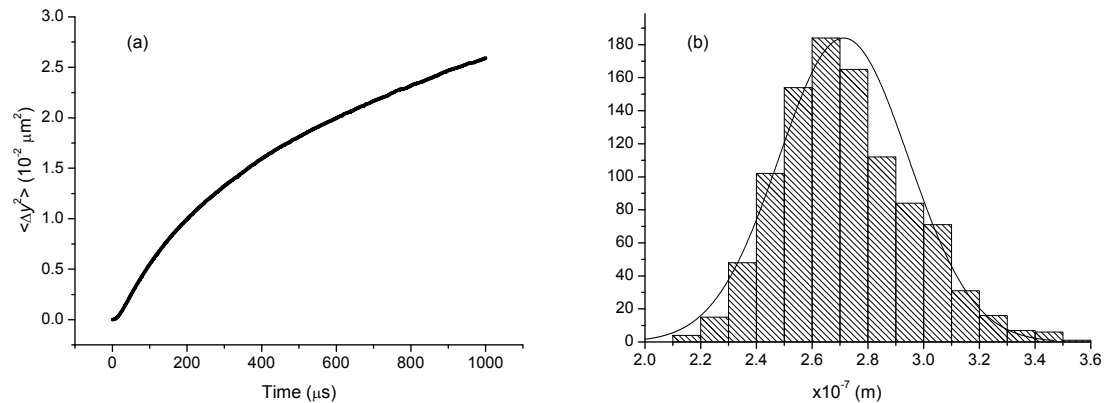


Figure 4-12. Long time effect of particle's diffusion at $y/R=1.12$.

(Note: (a) Mean square displacements $\langle \Delta y^2(t) \rangle$ as a function of t , for particle in charged system near a planar wall ($y/R = 1.12$). And (b) histograms of particle's final position in y direction, over 1000 samples.)

By exploring the particle's diffusion at $y/R=1.12$ for a long time (1ms), the mean square displacement $\langle \Delta y^2(t) \rangle$ increases towards its equilibrium state. And the final positions of particle in y direction agree with a normal distribution, with an average value of 260 nm, which is $2.6R$ away from the wall (Figure 4-12).

4.4.2.3 Particle size effect

Below we examine the diffusion of particle with different size. The particle radius is decreased from 100 nm to 50 nm and 10 nm, respectively, and the simulation time step is decreased to 0.1 ns and 0.005 ns accordingly since the relaxation time decrease. All the other parameters are kept the same as shown in Table 4-2 for a charged particle of radius 100 nm, suspended in an aqueous system.

The relaxation time τ_R calculated from Equation 4-24 for particle of radius 50 nm and 10 nm are 1.31 ns and 7.99×10^{-2} ns, respectively. And the theoretical diffusion coefficients calculated from Equation 4-2 are $3.83 \times 10^{-12} \text{ m}^2\text{s}^{-1}$ and $1.28 \times 10^{-11} \text{ m}^2\text{s}^{-1}$, respectively. The simulated free diffusion coefficients D_0 in bulk for particle of radius 50 nm and 10 nm are $3.81 \times 10^{-12} \text{ m}^2\text{s}^{-1}$ and $1.26 \times 10^{-11} \text{ m}^2\text{s}^{-1}$, respectively. The results are shown in Table 4-9 and Figure 4-13.

Table 4-9. D/D_0 for charged particle suspended in aqueous system near a planar wall. Comparison among theoretical prediction, simulation cases of particle of radius 100 nm, 50 nm and 10 nm.

y/R	$D_{//} / D_0$				D_{\perp} / D_0			
	theory	simulation			theory	simulation		
		100 nm	50 nm	10 nm		100 nm	50 nm	10 nm
1.18	0.48	0.26	0.39	0.25	0.17			
1.24	0.52	0.29	0.41	0.29	0.21			
1.30	0.55	0.35	0.45	0.33	0.24			
1.50	0.62	0.39	0.48	0.42	0.34			0.16
2.3	0.76	0.59	0.67	0.59	0.56	0.33		0.38
4.7	0.88	0.73	0.85	0.79	0.78	0.63	0.76	0.67
7.0	0.92	0.83	0.92	0.85	0.85	0.73	0.81	0.74
12	0.95	0.90	0.94	0.93	0.91	0.87	0.90	0.85
16	0.96	1.0	0.95	0.99	0.93	0.81	0.94	0.84

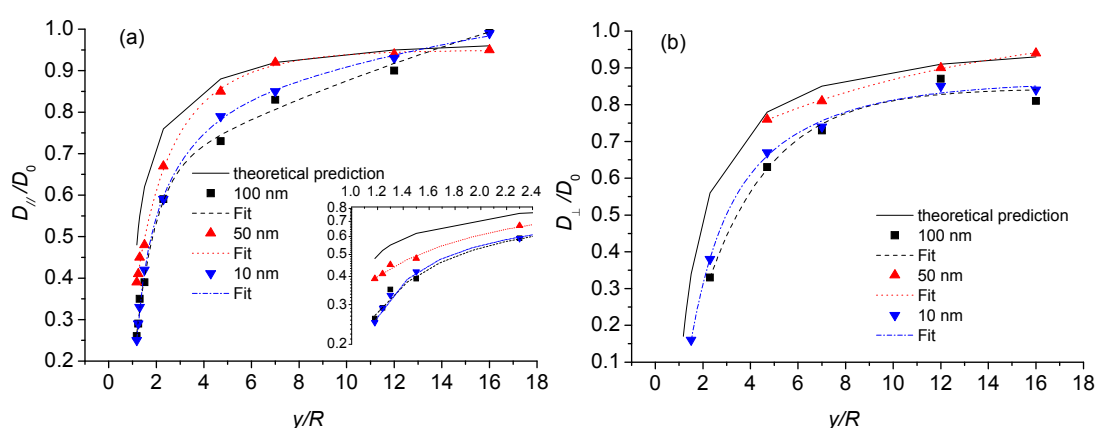


Figure 4-13. D/D_0 for charged particle suspended in aqueous system near a planar wall. Comparison among theoretical prediction, simulation cases of particle of radius 100 nm, 50 nm and 10 nm.

(Note: (a) Comparison of the simulated parallel diffusion coefficients $D_{//}$ normalized by D_0 , for particle size 100 nm (solid square), 50 nm (solid up-triangle), 10 nm (solid down triangle) and

the theoretical prediction (solid line). The inset with log-log scales magnifies the difference of D_{\parallel}/D_0 when $y/R \sim 1$. And (b) comparison of the simulated perpendicular diffusion coefficients D_{\perp} normalized by D_0 , for particle size 100 nm (solid square), 50 nm (solid up-triangle), 10 nm (solid down triangle) and the theoretical prediction (solid line). The dash line, the dot line and the dash-dot line are fitted with third order exponential decay function for simulation values of particle size 100 nm, 50 nm and 10 nm, respectively.)

With the particle size decreasing from 100 nm to 50 nm, the diffusion coefficients in both perpendicular and parallel directions increase (Figure 4-13). And by comparing the mean square displacements $\langle \Delta y^2(t) \rangle$ perpendicular to the planar wall (Figure 4-11, Figure 4-14(a)), smaller particles are less hindered when particle moves close to the planar wall.

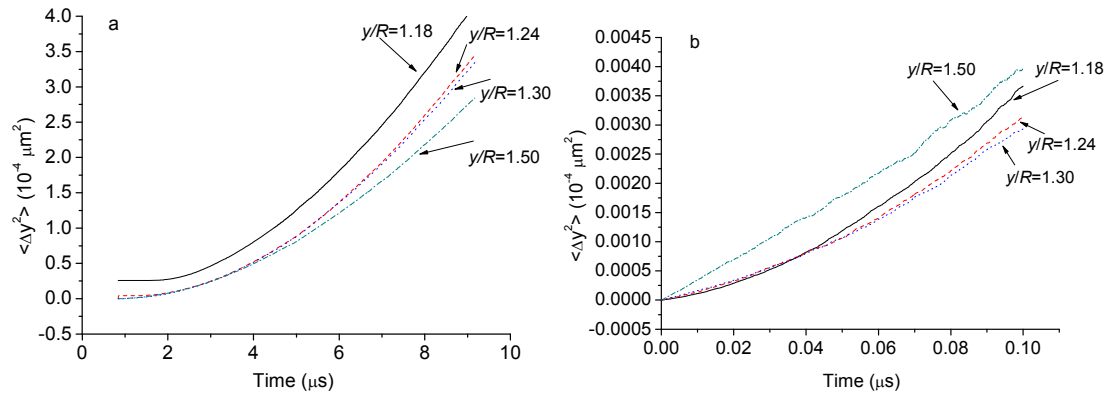


Figure 4-14. Mean square displacements $\langle \Delta y^2(t) \rangle$ as a function of t during 2×10^4 simulation time steps, for particle of radius (a) 50 nm, and (b) 10 nm in charged system near a planar wall ($y/R \sim 1$).

However, when the particle decreases from 50 nm to even smaller size, i.e. 10 nm, the diffusion coefficients in both perpendicular and parallel directions decrease, especially for very close distance, i.e. $y/R \sim 1$. This is because for a particle of radius 10 nm and with a 7 nm hydration layer, the DLVO forces and geometrical confinement effect are negligible compared to hydration force which prohibits particle diffusion (Figure 4-13). And it is shown from Table 4-9 and Figure 4-13(b) that the starting points of perpendicular

diffusion coefficient which can be derived from linear fit of $\langle \Delta y^2(t) \rangle$ to t as a constant are different for different particle sizes, which are $y/R=2.3$, $y/R=4.7$ and $y/R=1.5$ for particle size of 100 nm, 50 nm, and 10 nm, respectively. It is thus confirmed that particle diffusion coefficient in the vicinity of a planar wall is influenced by different types of forces for different particle size. That is hydrodynamic drag force dominates particle diffusion for particle of radius 100 nm, DLVO forces dominates particle diffusion for particle of radius 50 nm, and hydration force dominates particle diffusion for particle of radius 10 nm.

Moreover, a further comparative simulation case is performed to show the effect of charged system on the particle diffusion at nanoscale. As shown in Figure 4-15, for the parallel diffusion coefficient for a particle of radius 10 nm, the difference between a charged system and a neutral system is negligible, especially as y/R approaches 1 (Figure 4-15(a)). And for perpendicular diffusion coefficient D_{\perp} , compared to neutral system, it is larger in charged system, except for very close distance, e.g. $y/R=1.18$ (Figure 4-15(b)), where the effect of hydration force surpasses the DLVO forces.

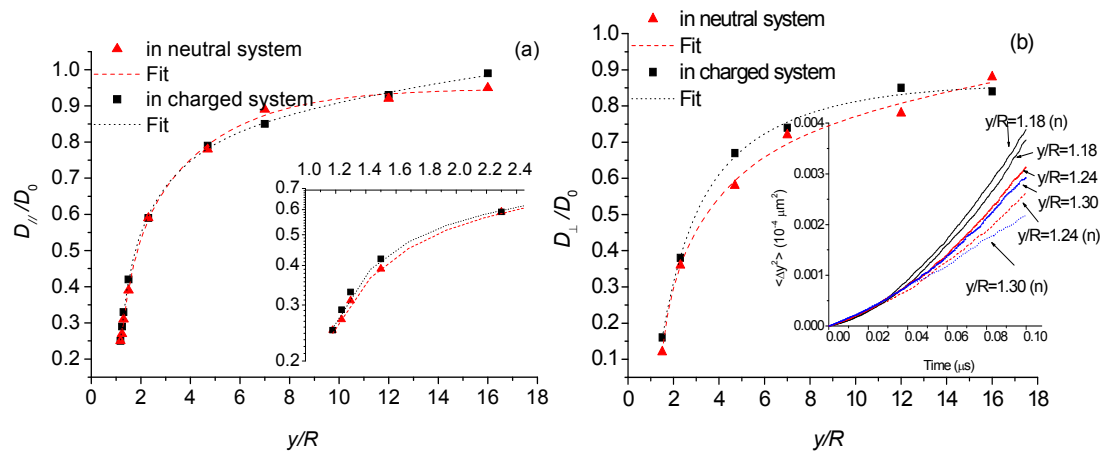


Figure 4-15. Effect of charged system on the particle diffusion at the nanoscale level.

(Note: (a) The simulated parallel diffusion coefficients $D_{||}$ (solid square) normalized by D_0 , for particle of radius 10 nm in charged system near a planar wall, compared with particle in neutral system (solid up-triangle). The inset with log-log scales magnifies the difference of $D_{||}/D_0$ between charged system and neutral system when $y/R \sim 1$. And (b) the simulated

perpendicular diffusion coefficients D_{\perp} (solid square) normalized by D_0 , for particle in charged system near a planar wall, compared with particle in neutral system (solid up-triangle). The inset shows the mean square displacements $\langle \Delta y^2(t) \rangle$ as a function of t , for particle of radius 10 nm in charged system and neutral system near a planar wall ($y/R \sim 1$). The dash line and the dot line are fitted with third order exponential decay function for simulation values in neutral system and charged system, respectively.)

The numerical descriptions of diffusion coefficients as explicit functions of the distance between the particle and the wall are:

For particle of radius 50 nm system,

$$\lambda_{//}^{-1} = \frac{D_{//}}{D_0} = 0.949 - 0.571e^{-0.396(y/R)} - 0.749e^{-1.122(y/R)} \quad (4-30)$$

$$\lambda_{\perp}^{-1} = \frac{D_{\perp}}{D_0} = 1.038 - 0.434e^{-0.094(y/R)} \quad (4-31)$$

For particle of radius 10nm system,

$$\lambda_{//}^{-1} = \frac{D_{//}}{D_0} = 1.165 - 0.679e^{-0.612(y/R)} - 0.451e^{-0.057(y/R)} - 4.835e^{-2.887(y/R)} \quad (4-32)$$

$$\lambda_{\perp}^{-1} = \frac{D_{\perp}}{D_0} = 0.861 - 0.601e^{-0.252(y/R)} - 1.117e^{-0.900(y/R)} \quad (4-33)$$

4.5 CONCLUSIONS

In this study the diffusion of spherical colloidal particle suspended in aqueous solution has been demonstrated at the microscopic level. The simulated model was validated using the experimental work done by Lin et al.. And to enlarge the model's applicability, the diffusion of particle at the very close distance (less than 100 nm) was explored and the diffusion coefficient under different particle size and charged system was analysed. The mobility of charged particle was found to be larger than that of uncharged particle, due to the DLVO forces between charged surfaces (with the same sign). This was

observed through simulation data analysis that the diffusion coefficient of spherical colloidal particles in charged suspension was larger than that in neutral suspension. In charged system, when the particle moved very close to planar wall (less than 100 nm), i.e. $y/R \sim 1$, the asymmetry effect of particle diffusion between perpendicular and parallel directions became more obvious and the mean square displacement perpendicular to the wall increased quadratically. The results yielded the diffusion coefficients as explicit functions of the distance between the particle and the wall.

CHAPTER FIVE

SIMULATION OF COLLOIDAL SELF- ASSEMBLY

CHAPTER FIVE

SIMULATION OF COLLOIDAL SELF-ASSEMBLY

5.1 INTRODUCTION

Monodisperse colloidal particles can self-assemble into highly ordered crystal structures under both equilibrium and non-equilibrium conditions (Grzybowski et al., 2009, Glotzer et al., 2004). The size of the constituent particles indicates that they are the ideal building blocks for creating 2D and 3D highly-ordered structures that can have feature sizes of biological entities, macromolecules, and the wave-length of photons (Xia et al., 2001, Vlasov et al., 2001, López, 2003, Weitz and Russel, 2004).

Various techniques developed for facilitating colloidal self-assembly can be categorised into two types: the first one is based on the methods in which the ordered structures are formed in a confined suspension, such as the sedimentation process (Miguez et al., 1997), while the second one refers to evaporation-induced methods, such as the vertical deposition method (Jiang et al., 1999) where fluid flow field takes effect. In recent years considerable progress has been made to prepare ordered structures by both methods (Xia et al., 2000, Wong et al., 2003, Ramsteiner et al., 2009). However, a fundamental understanding of the convective self-assembly process still requires elucidation. Dimitrov and Nagayama (1996) made the first attempt in modelling vertical lifting convective self-assembly. They derived a mathematical model based on mass balance at the meniscus drying front, which can predict the colloidal crystal thickness as a function of the suspension concentration, vertical lifting speed and evaporation rate. Because of the over-simplifications of the particle-particle, particle-substrate interactions, deviations from the model have been reported (Fustin et al., 2004). More importantly, such a phenomenological model lacks the ability of predicting the detailed microstructures of the crystal formation. Recently, computational fluid dynamics (CFD) simulation has been applied on a three-dimensional face centred cubic (*fcc*) colloidal array and verified the

hypothesis that the fluid convective flow steers the colloidal crystal growth and reinforces the tendency of *fcc* structure formation (Jun et al., 2005, Gasperino et al., 2008, Brewer et al., 2008). However, in these models the interactions between particles and between particles and boundaries are also neglected, limiting the predictive function of the models.

It has been reported from both experimental (Bonissent et al., 1984, Palberg and Biehl, 2003, Fontecha et al., 2005) and mathematical (Pansu et al., 1984, Meng et al., 2006) analyses that a series of structural transitions occur corresponding to the increased crystal thickness of a growing crystal. These transitions consist of changes in both layer numbers and structural patterns. During this process, the meniscus slope near the crystal boundary influences the number of particle layers and the transition structures which typically exhibit changing from triangular stacking to square stacking and back to triangular stacking, as revealed by the microscopic observation by Norris and co-workers (Meng et al., 2006). In their simulation work (Meng et al., 2006), the particles were assumed to be non-interacting hard spheres and the growth front was maintained as ramp shape, and pre-packed rows of particles were added sequentially to the structure during the assembly process. Although such a simulation illustrated the structural transition phenomenon during particle assembly from the viewpoint of geometrical confinement, the strongly imposed simplifications, such as pre-packed rows of particles moving as an integrated body, prevents a thorough understanding on the detailed formation mechanisms of structural transitions.

In the self-assembly of colloidal crystals, the colloids experience a sequence of phases, namely, suspension, migration (towards the crystallization front), deposition, and drying/fixation. Various types of interactions take place simultaneously and the resultant structure of the colloidal crystal is a complex balance of the driving forces, and the attractive or repulsive interactions. In the system, each particle has its own fate as a result of its interactions with the surrounding medium, boundaries, and neighbouring particles. Since the

role of capillary force in the colloidal crystal structure formation has been well studied probably due to the relative ease in experimental observation (Denkov et al., 1993, Zhou et al., 2006), this numerical study attempts to elucidate the effects of the fluid flow and geometry confinement by removing the considerations of the capillary forces. The discrete element method (DEM) (Cundall and Strack, 1979, Tsuji et al., 1993, Li et al., 2005, Feng et al., 2004) was applied to model the colloidal packing under the influences of fluid flow and geometry confinement (such as the shape of the liquid meniscus in vertical-lifting self-assembly) by taking into account the interparticle interactions (Li et al., 2008) and tracking each particle's motion individually. Through the computer simulation, we reveal the assembly mechanism at the microscopic level and study how the structure formations are affected by geometry confinement and fluid flow during the colloidal crystal growth.

5.2 MODEL ESTABLISHMENT

5.2.1 General Framework

In-house developed software 'SimCos' (Fang and Li, 2009), which specifically simulates colloidal suspensions, has been used and modified for this study. The computer program is developed in Microsoft Visual Studio 2005 using Visual C++ programming language. Details of the development of the simulation platform is introduced in Chapter 3.

The geometrical set-up of the simulation unit is sketched in Figure 5-1. A 0.84% (v/v) colloidal suspension system is representatively modelled by this cubic volume ($10\ \mu\text{m} \times 10\ \mu\text{m} \times 10\ \mu\text{m}$). The cube is placed in a Cartesian coordinate system, with its centre as the origin of coordinate, and x-z plane at $y=5\ \mu\text{m}$ as the top plane. On top of the cube, two planes are defined: the vertical plane simulates a solid substrate as often used in the experimentation, while the inclined plane represents the spatial confinement or the free surface of a liquid meniscus. The two planes intersect and form a

wedge-shape confinement with a contact angle θ , which represents the meniscus contact angle on a vertical substrate. 2000 spherical colloidal particles of 200 nm diameter are randomly dispersed in the cube, subject to Brownian motions. It is noted that strong simplifications have been applied to the treatment of the meniscus free surface.

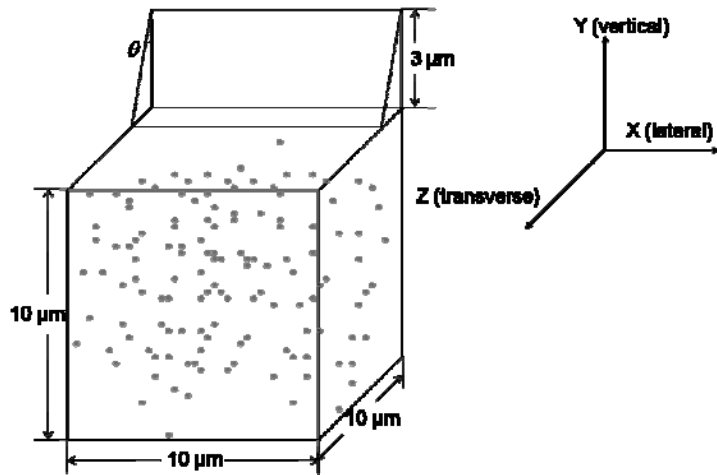


Figure 5-1. Geometrical set-up of the simulated cell of a colloidal suspension system.

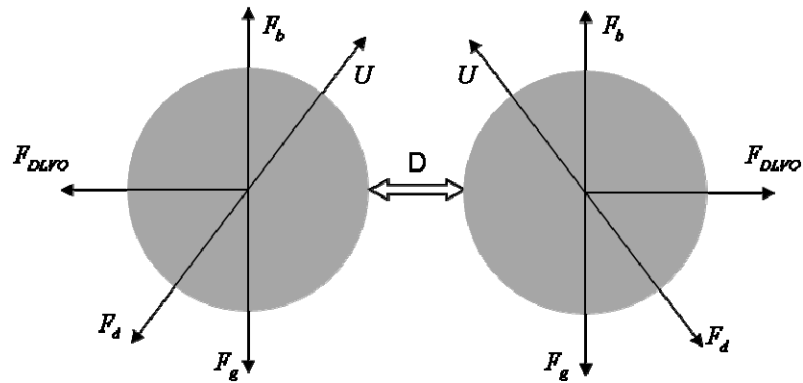


Figure 5-2. Scheme of interparticle interactions.

Both interparticle and particle-boundary interactions are taken into account in the simulation model. The Brownian force and DLVO potential interaction forces have been applied to each particle. The Brownian force is modelled as a Gaussian distribution random sequence signal. The particles are assigned

with a surface potential of -30 mV (Li et al., 2008). The Hamaker constant, A_H is set as 7.65×10^{-21} J (Bergna and Roberts, 2006, Butt et al., 2003, Hunter, 2001). The models used to calculate the forces of interparticle and particle-boundary interactions are listed in Figure 5-2 and Table 5-1. Parameters used in the simulation are listed in Table 5-2.

Table 5-1. Forces acting on the particle.

Forces	Symbols	Equations
DLVO force	F_{DLVO}	$2\pi R\epsilon\epsilon_0\psi_0^2 e^{-\kappa D} - A_H R / 12D^2$
Fluid drag force	F_d	$-6\pi\eta RU$
Buoyancy force	F_b	$-\rho_f \frac{4}{3}\pi R^3 g$
Gravitation force	F_g	$\rho_p \frac{4}{3}\pi R^3 g$
Brownian force	F_B	$G_i \sqrt{\frac{12\pi k_B T \eta R}{t_d}}$

(Note: ψ_0 is the particle surface potential, κ is the inverse Debye length, ϵ , ϵ_0 are the dielectric permittivity of the suspending medium and vacuum permittivity respectively, A_H is the Hamaker constant, R is the particle radius, D is the particle edge-to-edge separation distance, η is the fluid viscosity, U is the particle velocity, G_i is a Gaussian distribution random sequence, k_B is the Boltzmann constant, T is the temperature, t_d is the simulation time step, ρ_f , ρ_p are the fluid density and particle density respectively, g is the acceleration due to gravity)

The computational time step, t_d , is set as 0.5 ns after several trial runs being conducted. It is a constant value chosen to ensure the stability and accuracy of the numerical simulation, particularly for the integration. It was proposed that the selection of t_d should be proportional to the ratio between the maximum stiffness and the particle with smallest mass (Asmar et al., 2002,

Krugger-Emden et al., 2008), i.e. $t_d \propto \sqrt{\frac{k}{m}}$. At each calculation time step the forces that act on a particle are computed; the velocities and the displacements of the particles are calculated by integration of Newton's equations of motion as follows:

$$m_p \frac{dU}{dt} = F_{DLVO} + F_b + F_g + F_d + F_B \quad (5-1)$$

where m_p is the particle mass.

Table 5-2. Key simulation parameters of particles self-assembly model.

Variables	Base values
Particle shape	Spherical
Number of particles, N	2000
Particle radius (nm), R	100
Particle density (kg m^{-3}), ρ_p	2200
Fluid density (kg m^{-3}), ρ_f	1000
Particle surface potential (mV), ψ_o	-30
Hamaker constant (J), A_H	7.65×10^{-21}
Fluid viscosity (Pa s), η	0.001
Time step (ns), t_d	0.5

5.2.2 Consideration on the Fluid Field

All the particles which are originally dispersed in the cube are driven upward by the fluid flow, as illustrated in Figure 5-3. The particles which are driven across the rear plane of the cube are set to re-enter the cube from the front plane, which represents a periodical boundary condition as in a colloidal

suspension system. In the wedge section, the particles driven across the rear plane are set to deposit on the vertical surface. The fluid flow field is modelled 2D in y - z plane, as a function of particle's xyz coordinates (Equations. 5-2, 5-3 and 5-4), which are calculated by dividing its actual decimal coordinates by the particle radius.

$$V_x = 0 \quad (5-2)$$

$$V_y = a \left[(y_i - Y)^2 + (z_i - Z)^2 \right] \quad (5-3)$$

$$V_z = b (y_i^2 + z_i^2) \quad (5-4)$$

where a and b are the coefficients to control the fluid flow velocity and direction, y_i and z_i are particle's coordinates, and Y , Z are the cell size in Y and Z axes.

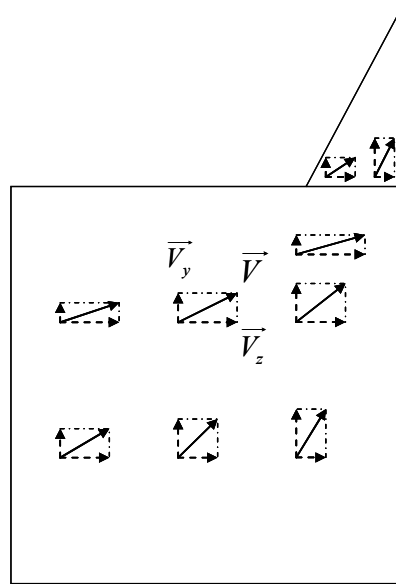


Figure 5-3. Side sectional view of the simulated fluid flow field in a colloidal suspension system.

5.2.3 The Rules Set for Particle Deposition

An essential element for simulating the colloidal crystal formation is the establishment of a set of rules that prescribes the colloidal particles motion and packing based on physical laws. To simplify the simulation, the 1st row of the 1st layer of a close-packed structure is assumed to form instantaneously.

According to the established stability criterion (Rabideau and Bonnecaze, 2004, Gray and Bonnecaze, 2001, Gray et al., 2000, Feder, 1980), the rules of particle deposition are illustrated in Figure 5-4. For the 1st layer grown on the substrate, one particle of interest is set as 'stationary' when it forms a triangular structure with other two stationary particles above it. All these particles are tangent to each other. Particles that fall in the boundary area will be set 'stationary' as soon as they are in contact with two other stationary particles, no matter whether these two particles are above it or not as illustrated in Figure 5-4(a).

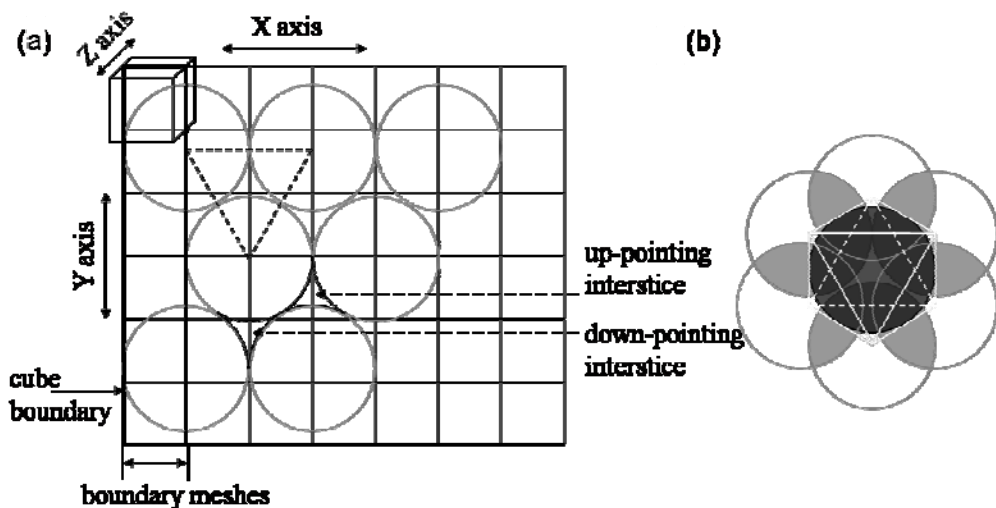


Figure 5-4. General stationary rules for particles deposition.

(Note: (a) for particles in the 1st layer and (b) for particles in multilayer (particles in upper layer have been made transparent in the image).)

For multilayer packing, there are two choices for the 2nd layer to build upon, namely the up-pointing interstices and the down-pointing interstices as indicated in Figure 5-4(a). Theoretical estimations from thermodynamic viewpoint (Frenkel and Ladd, 1984b, Bolhuis et al., 1997, Woodcock, 1997, Mau and Huse, 1999) and from hydrodynamic analysis (Norris et al., 2004) predicted that a particle in multilayer prefers to nestle into an octahedral interstice to form an *fcc* stacking of close-packed structure as illustrated in Figure 5-4(b) (particles of grey colour belong to Layer 1; transparent particles belong to Layer 2; the 3rd layer particle with black colour nestles into the octahedron interstice), which is confirmed by experimental observations (Pusey et al., 1989, Miguez et al., 1997, Vlasov et al., 2001, Wang et al., 2006). For one moving particle of interest, if there are three stationary particles being found in the close vicinity to form such an interstice, the particle of interest settles down in this position (Figure 5-4(b)).

However, because of the geometry confinement, the available thickness d between the inclined plane and vertical solid substrate (Figure 5-5) may not allow the *fcc* stacking mentioned above. In this case, to maximize the packing density and lower the free energy, the triangular stacking structure can transit to square stacking structure, which depends on the available thickness d and in which layer this transition occurs.

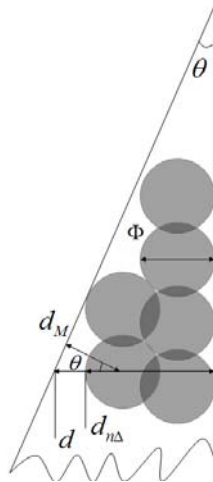


Figure 5-5. Growing structural transition condition.

If the available thickness d is too small, i.e. the centre of a particle in the multilayer is over the inclined plane, this particle will start packing from a row below. Here we use the distance from the centre of a particle to the inclined plane, d_M (Figure 5-5), to check if structural transition occurs. The thickness of a close-packed triangular structure is given by

$$d_{n\Delta} = [1 + (n-1)\sqrt{2/3}] \cdot 2R \quad (5-5)$$

where n is the layer number and R is the radius of a particle. The available thickness can be expressed as:

$$d = d_{n\Delta} - R + d_M \cdot \cos^{-1} \theta \quad (5-6)$$

And d_M is obtained from

$$d_M = (d - d_{n\Delta} + R) \cdot \cos \theta \quad (5-7)$$

If $d_M < 0$, the position is invalid to accommodate a layer addition. If $d_M > R$, the *fcc* structure formation is permitted. If $d_M < R$, transition occurs. For transitions in a bilayer system, the particles in the 1st layer are pressed to rearrange to form a square structure, while the particles in the 2nd layer also reorganise in order to be tangent to them. For transitions occurring in a multilayer system, i.e. n layers ($n > 2$), the particles in the $n-1$ layer shift to the next available interstices to form a square structure with the row above $n-1$ layer. Here we assign a transition flag $M[i]$ with an initial value 0 to each particle, and it changes to a new value 1 for the particles in a transition area.

For one moving particle i in monolayer, searching pattern is two mesh grids backward to two mesh grids forward in X axis, if two stationary particles number i_2 and i_3 with transition flag $M[i_2]=1$ and $M[i_3]=1$ are found (Figure 5-6(a), this moving particle is stationary.

For one moving particle i in multilayer, searching pattern is one mesh grid backward to one mesh grid forward in X axis, two mesh grids backward to one mesh grid backward in Y axis, and two mesh grids backward in Z axis. If two stationary particles number i_2 and i_3 with transition flag $M[i_2]=1$ and $M[i_3]=1$ are found (Figure 5-6(b)), the particle of interest is set as 'stationary'.

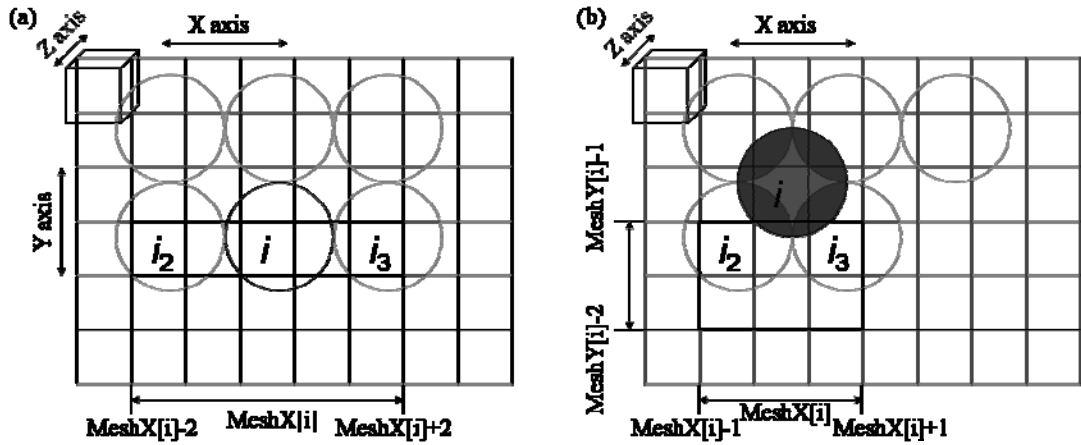


Figure 5-6. Stationary rules for particles in transition row.

(Note: (a) for particles in the 1st layer (b) for particles in multilayer (particles in upper layer has been made transparent in the image))

The structural transition appears to occur interdependently; when the transition is determined to take place at one particular time step, it influences not only the packing of the following active particles, but also the formerly settled particles in the neighbourhood. For simulating this situation, a neighbour list is introduced. For any particle i , when it becomes stationary, it is tangent to at least two other particles i_2 and i_3 when in monolayer, or to three other particles j_2 , j_3 and j_4 when in multilayer. These neighbouring particles form a neighbour list SS ($SS[i_2, i_3]$ or $SS[j_2, j_3, j_4]$), for any stationary particle i . For any stationary particle, it has a its corresponding and specific neighbour list. During the simulation, we check the value of these neighbour lists in each time step, if the value changes from initial value -1 to number i , then we know that particle i is stationary. Then the transition flag $M[i_2]$, $M[i_3]$ and $M[i_4]$ are checked, if one of these values, for example $M[i_2]$

changes from initial value 0 to 1, it means particle i_2 shifts to a new position in this time step and consequently particle i is reactivated (Fang and Li, 2009).

5.3 RESULTS AND DISCUSSIONS

Simulated colloidal crystal structures were formed under different wedge angle θ and different fluid flow field. For each fluid flow field, we simulated the wedge angle of 33.7° , 18.4° and 14.0° , respectively, for investigating the influence of wedge angle. The selection of the wedge angles was based on our previous experimental data where the meniscus shape was adjusted by adding surfactant (Zhou et al., 2006). Due to the small time step used, the simulations required substantial computation time. For instance, when dealing with 2000 particles on a personal computer with 3.00 GHz Intel Core 2 CPU, 2.00 G RAM and Windows XP operating system, the computational time was 24 h for a 0.5 ms simulated self-assembly time.

5.3.1 Self-assembly under Different Fluid Flow Field

In the simulation, the fluid flow velocity was controlled within the range of $10^{-1} \sim 10^1$ m/s by adjusting the coefficients a and b in Equation 5-3 and Equation 5-4. In CASE I (the reference case), a and b were set as 1×10^{-3} and 2×10^{-4} , respectively. In CASE II, both of the coefficients were reduced by a factor of 10; while in CASE III, only coefficient a was reduced by a factor of 10, to the value of 1×10^{-4} . The resultant fluid velocity fields under the three conditions are shown in Figure 5-7. In general, the particle initial velocity was on the order of 10^{-2} m/s, which was the thermal velocity determined by equilibrium equation:

$$\frac{1}{2}mU^2 = \frac{1}{2}k_B T \quad (5-8)$$

where U is the particle velocity. We first set the wedge angle θ constant at 33.7° .

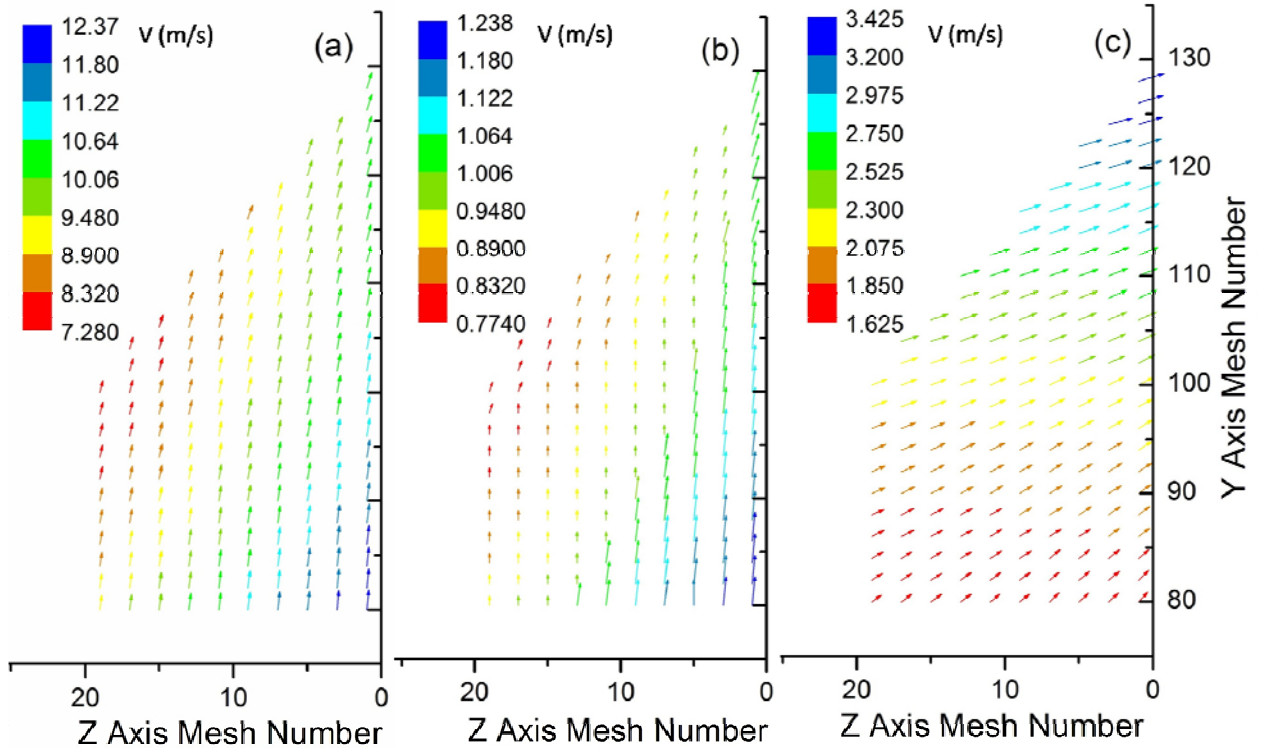


Figure 5-7. Side sectional view of fluid flow velocity vector contour in the wedge-shape confinement and nearby bulk volume.

(Note: The coefficients a and b in the fluid flow field Equation 5-3 and Equation 5-4 are (a) CASE I: $a=1\times 10^{-3}$, $b=2\times 10^{-4}$, (b) CASE II: $a=1\times 10^{-4}$, $b=2\times 10^{-5}$ and (c) CASE III: $a=1\times 10^{-4}$, $b=2\times 10^{-4}$, respectively.)

The simulated structures at the wedge front under the three different fluid flow velocity fields are shown in Figures 5-8(a), 5-8(b), and 5-8(c), respectively. When they are driven upward into the meniscus/wedge confinement, the particles find their niche positions and become stationary, resulting in close-packed crystal structure and increased packing density. It can be seen that under a smaller fluid velocity like in CASE II, rather than being quickly driven upward into the confined wedge space, particles are more broadly dispersed like Brownian particles.

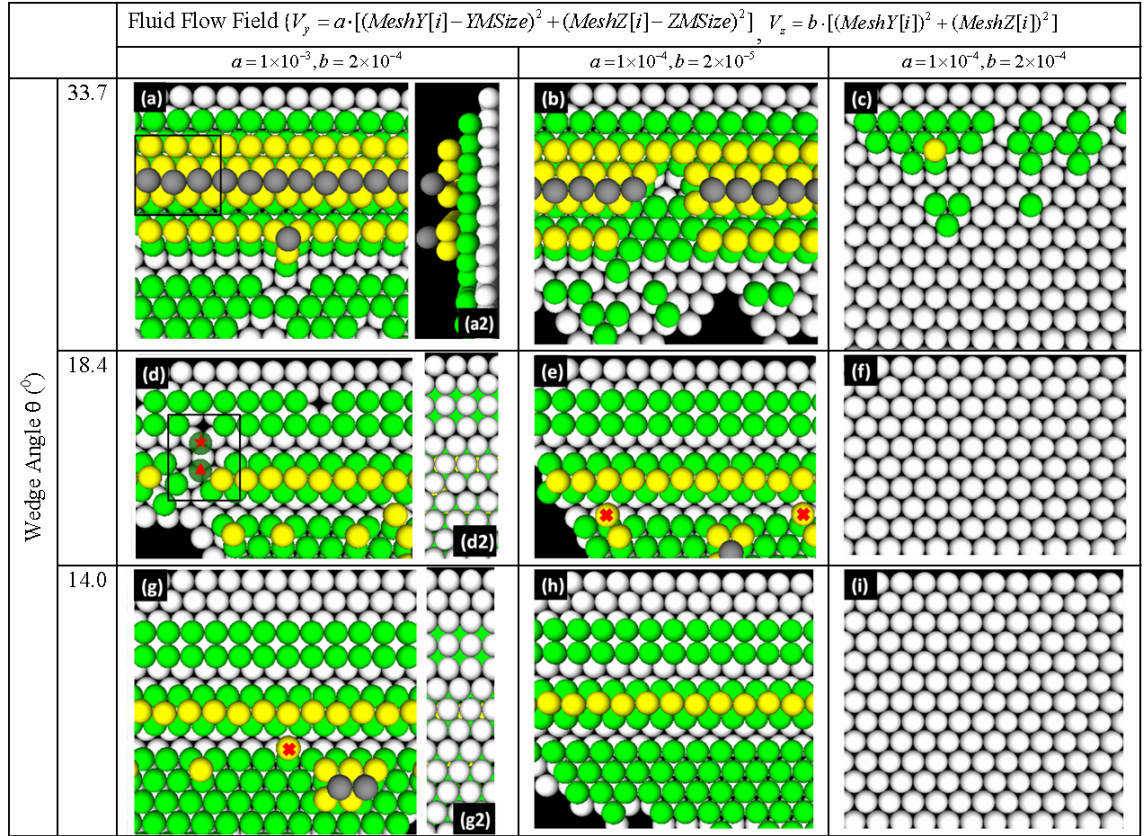


Figure 5-8. Growing crystal structures.

(Note: Different colours represent different layers in the resultant structures, i.e. white, green, yellow and grey represent 1st, 2nd, 3rd and 4th layer, respectively. (a2) is the side view of (a), (d2) is the backside view of (d), and (g2) is the backside view of (g). The particles marked with red star and red triangular will be discussed in the latter section.)

Figure 5-9 shows the snapshots of particles from a selected volume in the bulk under different fluid flow field. At $t = 0$, the colloidal particles are completely dispersed. For this dilute and still system, colloidal particles with the surface potential of -30 mV hardly aggregate because of the long distance repulsive potential between the particles and the displacement of particles by the Brownian motion cannot exceed the interparticle distance. At $t = 0.7 \mu s$, the particles have moved closer to each other driven by fluid flow and the system becomes more concentrated. Compared to the dilute and still system at $t = 0$, for this concentrated system, in contrast, colloidal particles that have relatively high repulsive potential sometimes collide with one

another since the displacement of particles by the fluid flow can exceed the interparticle distance and free Brownian motion. And the average interparticle distance are 2.03 nm and 396 nm respectively, for different fluid flow field in the above Cases I and II.

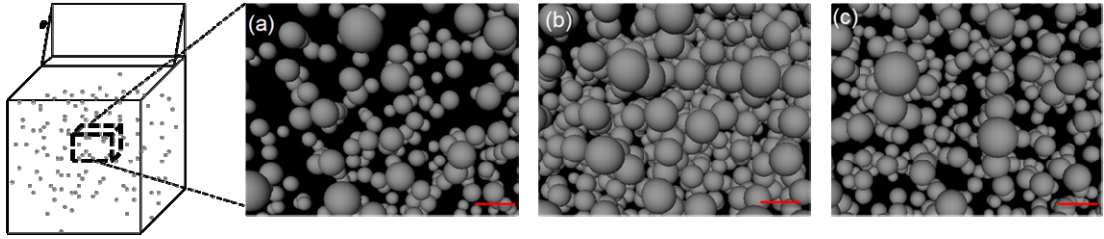


Figure 5-9. Snapshots of particles dispersion in the bulk volume.

(Note: (a) At time step $t = 0$, initial state without fluid flow field, (b) at time step $t = 0.7 \mu\text{s}$, in CASE I, and (c) at time step $t = 0.7 \mu\text{s}$, in CASE II. Scale bar is 200 nm. All particles are in monosize of 200 nm diameter, while the size difference shown in snapshots is caused by perspective projection.)

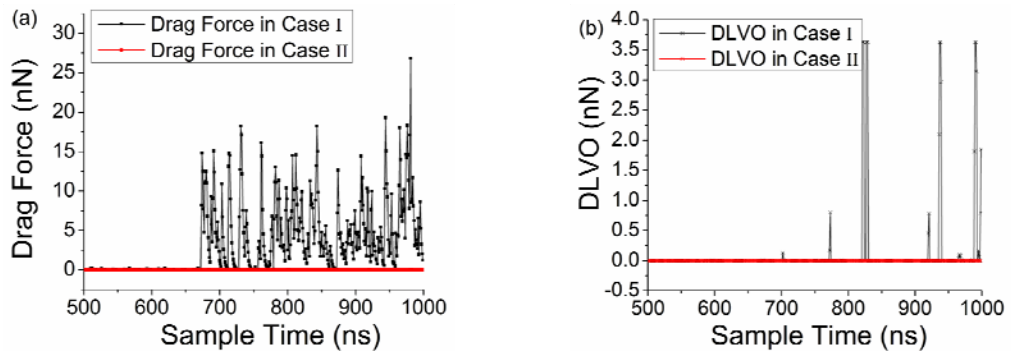


Figure 5-10. Profiles of forces on a randomly selected particle in CASE I and II.

Comparing the forces imposed on a randomly selected particle in the bulk volume from time step $t = 0.5 \mu\text{s}$ to $t = 1.0 \mu\text{s}$, the absolute values of fluid drag force and interparticle interaction forces are much smaller in the mild flow field (CASE II) (Figure 5-10). The particles also form looser packing with more defects in CASE II as shown in Figure 5-8(b). When comparing the DLVO forces experienced by a randomly selected particle, the force curve of the particle in Case I shows more drastic variations in the force magnitude as oppose to force curve of the particle in CASE II, as shown in Figure 5-10(b).

The stronger fluid flow entrains and compacts the particles at a much higher speed, which causes the intensive DLVO interactions among the particles. For example, at sample time $t=827$ ns, the examined particle in Case I is very close to particles in its neighbourhood (0.2 nm to its nearest neighbourhood particle).

Figure 5-8(c) shows the resultant crystal structure at the end of simulated time of CASE III when only the fluid flow velocity in the vertical direction is reduced by a factor of 10. In this case, the components of fluid drag force and interparticle interaction forces in transverse direction are greater than the force components in vertical direction, and fluid drag force plays a dominant role during the process, as shown in Figure 5-11; or in other words, the particles move much more rapidly in the transverse direction than in vertical direction. Under this condition, the resultant structure becomes 2D crystal in dominance, with only a few particles sporadically deposited as the 2nd or 3rd layer.

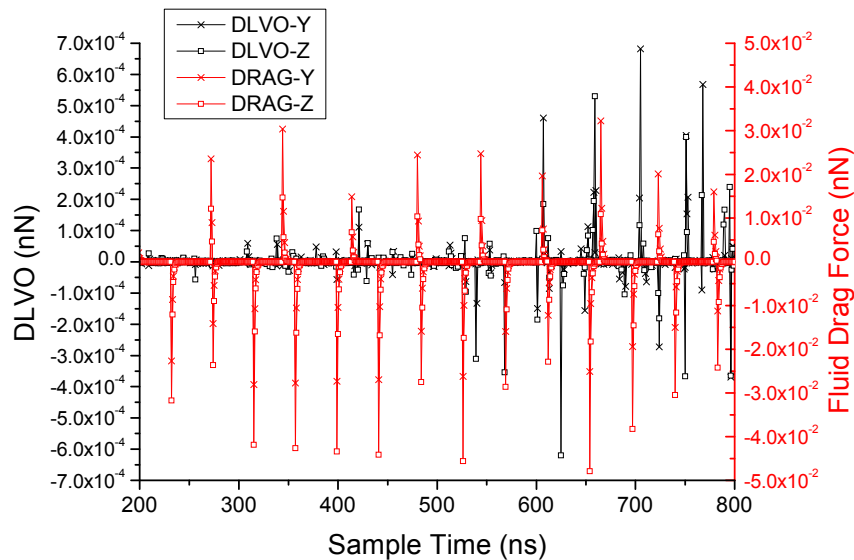


Figure 5-11. Profiles of forces on a randomly selected particle in CASE III.

5.3.2 Self-assembly under Different Wedge Shape Angle

The influence of wedge angle θ can be observed by comparing the simulated crystal structure vertically in Figure 5-8. For example, Figures 5-8(a), 5-8(d) and 5-8(g) show that the simulated colloidal crystal structures at the wedge angle 33.7° , 18.4° , and 14.0° , respectively, when the fluid velocity field is set as in CASE I, i.e. $a = 1 \times 10^{-3}$, $b = 2 \times 10^{-4}$ in Equations 5-3 and 5-4. In Figure 5-8(a), it is shown that with a large wedge angle θ ($\theta = 33.7^\circ$), quadlayer is formed from Row 6 (the 1st row in the 1st layer is used as the reference row), which is also the position where structural transition occurs when particles assemble from a trilayer to a quadlayer, as more clearly shown by the side view in Figure 5-8(a2). The transition occurrence is caused by the available thickness of the confined geometry and the packing density maximization. The available thickness, d , at where a quadlayer formed is 682.7 nm, and d_M is 76.8 nm, according to Equations 5-5, 5-6 and 5-7. Since d_M is less than R (100 nm), the particles in the 3rd layer shifted to the next available interstices to form a square structure with the above 3rd layer row, in order to allow the 4th layer addition. As the particle stacking continues, the available wedge thickness d between the inclined plane and the vertical plane increases continuously. However, due to the lattice mismatching, the immediate subsequent packing is disturbed, which causes the line defect formation between Row 6 and 8 as shown in Figure 5-8(a). When the wedge shape is sufficient to pack 4 layers without deforming the *fcc* ordered structures, that is for the particles in the 4th layer, $d_M \geq R$ (Figure 5-5), the triangular stacking structure is observed again as shown in the lower part of Figure 5-8a.

By decreasing the wedge angle θ ($\theta = 18.4^\circ$), structural transition occurs at Row 3 (shown in Figure 5-8(d2), viewed through the backside of the vertical plane) when particles assemble from monolayer to bilayer, which is a transition region with square stacking structure (Figure 5-8(d)). This is because the available thickness, d , at where a bilayer formed is 282.7 nm,

and d_M is 18.1 nm. Since $d_M < R$, and the particles in the 1st layer rearrange to form a square structure, while the particles in the 2nd layer also reorganise in order to be tangent to them. As the particle stacking continues, square stacking structure is observed in the transition region from a bilayer to a trilayer where $d_M < R$ (as illustrated in Figure 5-5) for particles in the 3rd layer. With even smaller wedge angle θ ($\theta = 14.0^\circ$), compared to the structure formed under large θ ($\theta = 18.4^\circ$), the same square transition region and transition procedure with square stacking structure occurs. However, the transition position shifted to Row 4 (Figure 5-8(g2), backside view) when particles assembled from monolayer to bilayer, because the wedge thickness d was too small to allow square stacking in an upper position.

For particle assembly with relatively small wedge angle θ ($\theta = 18.4^\circ$), and under the fluid flow field in which the components of fluid drag force and interparticle interaction force in vertical direction are greater than the transverse force components by an order of $10^0 \sim 10^2$, only monolayer structure is formed (Figure 5-8(f)). The same structure is formed when the wedge angle reduces to 14.0° (Figure 5-8(j)). This result suggests that colloidal monolayer formation may be controlled by creating a suitable fluid velocity field.

5.3.3 Defect Formation Mechanism

From the resultant ordered structures, some point defects are observed, for example, the area above the particle labelled with a red star in Figure 5-8(d) is a vacancy defect, while the 'red triangle' particle (Figure 5-8(d)) and 'red cross' particles (Figure 5-8(e), Figure 5-8(g)) are interstitial defects, line defects are also observed where structural transition occurred. The simulation data were analysed to understand the cause of defects formation. The 'red star' particle and 'red triangle' particle are selected as the examples to illustrate the defect formation in the simulation (Figure 5-8(d), Figure 5-

12(c)). The selected data set is from 1200 time-steps before the defect formation till the step when defects are created. Figure 5-12 shows the trajectories of these two particles moving to a stable position under the coupling effect of fluid flow and geometry confinement.

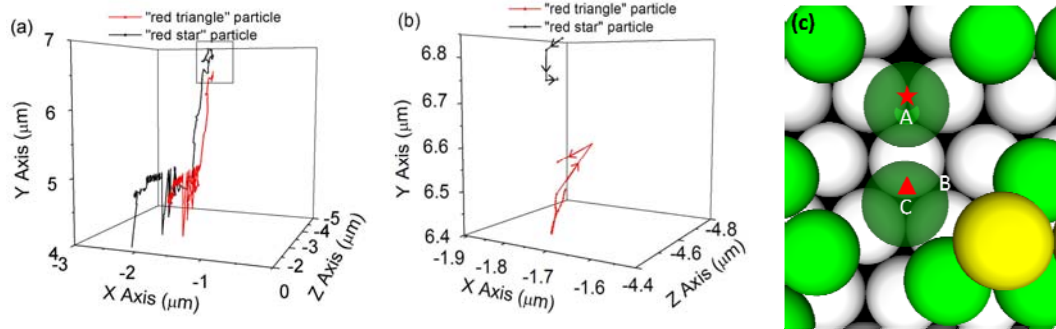


Figure 5-12. Trajectories of two particles during self-assembly process.

(Note: (a) Two particles marked in Figure 5-8(d), (b) close-up view of the rectangular area in Figure 5-12(a), the arrows denote direction of particle movement, and (c) close-up view of the rectangular area in Figure 5-8(d).)

It is shown that both particles move dramatically under fluid flow in the cubic bulk suspension (x - z plane at $y=5$ is the top plane of the cube). And after the particles being driven to the wedge-shape confinement on top of the cube, both particles move mildly since the equilibrium of interaction forces drives the particles to settle down and point defects are formed because of the fluid flow and geometry confinement. As shown in Figure 5-12(b), compared to the 'red triangle' particle, the 'red star' particle settles down at a higher position first.

The settle-down time for 'red star' and 'red triangle' particle are $0.875 \mu s$ and $0.885 \mu s$, respectively. The force profile of the 'red star' particle is shown in Figure 5-13. It demonstrates that fluid drag force has dominated during the whole self-assembly process (Figure 5-13(a), Figure 5-13(b)) and thus drives the 'red star' particle to the wedge-shape confinement to form a point defect.

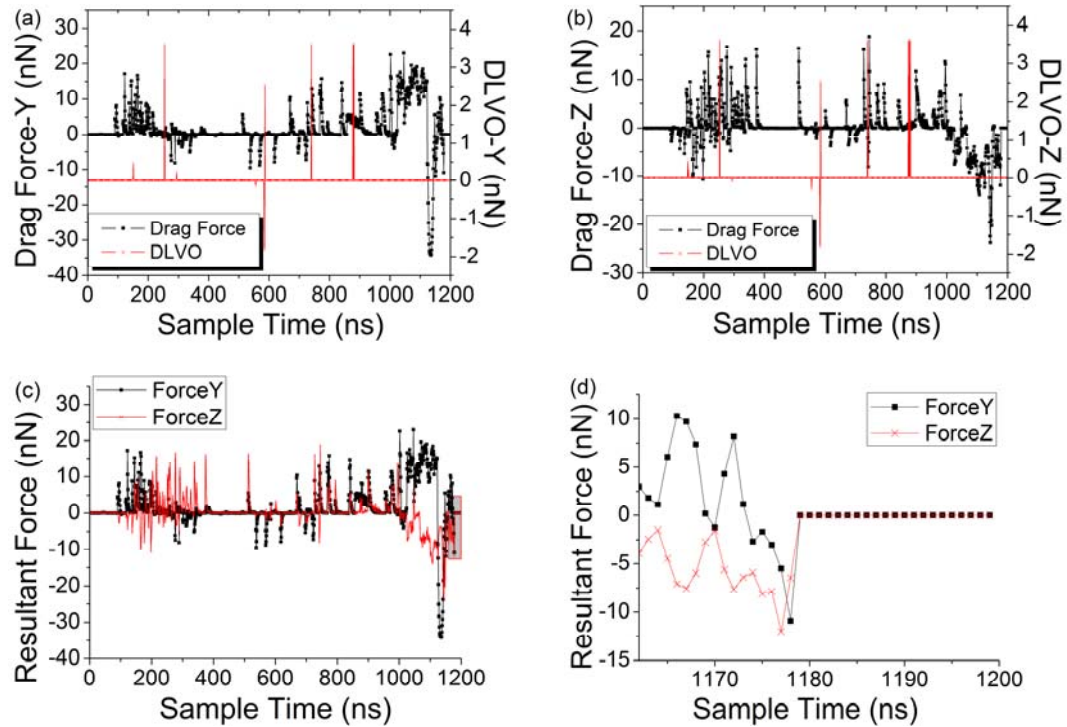


Figure 5-13. The force profile of the 'red star' particle.

(Note: (a)-(b) Profiles of forces on 'red star' particle in Y and Z axes, (c) resultant force on 'red star' particle, and (d) close-up view of the shadow area in Figure 5-13(c).)

The resultant forces in vertical y and transverse z directions are examined for understanding the defect formation process. During the self-assembly process, the resultant forces in vertical y and transverse z directions are of the same magnitude (Figure 5-13(c)), and thus drives the particle closely towards the substrate rather than deposits the particle on the plane of the cube. Before particle settles down, e.g. from 5 time-steps before the vacancy defect formation, the resultant force in vertical y direction are -2.69 nN, -1.67 nN, -3.03 nN, -5.52 nN and -10.90 nN, respectively (Figure 5-13(d)). All these forces are in negative y direction, and thus prohibit the 'red star' particle from moving upwards. Meanwhile, the resultant force in negative z direction is larger than its component in negative y direction, as shown in Figure 5-13(d). So that the resultant force drives the 'red star' particle towards the 1st layer particles which are assembled on the substrate, and 'red star' particle settles down at interstice A which is an up-pointing interstice to form a stable stacking, while the 'red triangle' particle firstly settles down at interstice B

which is an up-pointing interstice. By calculating from Equations 5-5, 5-6 and 5-7, the available thickness for the 3rd layer particle stacking is $d = 435.4$ nm, and $d_M = 7.9$ nm, as $d_M < R$ (100 nm), structural transition occurs and the 'red triangle' particle shifts to its new stable position in interstice C which is a down-pointing interstice (Figure 5-12(c)). In this case, the point defects are formed.

Below the line defect appearing between the 2nd and 3rd rows of the 2nd layer in Figure 5-8(g) is investigated. In the beginning of 2nd layer formation, a transition occurred and square structure was formed as shown by row 1 and 2 of the 2nd layer. If the particles at row 3 of the 2nd layer reside in the up-pointing interstices following the square transition structure, interparticle overlapping would then occur between particles at row 2 and row 3. If the particles at row 3 of the 2nd layer reside in the down-pointing interstices following the square transition structure, the following particles in the 2nd layer would follow the suite and also stabilize into the down-pointing interstices to form triangular structure, as shown in Figure 5-14(b). Then particles in the 3rd layer would occupy the octahedral interstices (as black dashed arrow pointed in Figure 5-14(b)), to form *fcc* structure. By calculating from Equations 5-5, 5-6 and 5-7, the available thickness where this 3rd layer formed is $d = 447.9$ nm, and $d_M = 20.2$ nm. Since $d_M < R$ (100 nm), structural transition would occur. The particles at row 3 of the 2nd layer would move into the up-pointing interstices following the square transition structure, and the interparticle overlapping occurred between particles at row 2 and row 3. In order to avoid interparticle overlapping during structure transition, the particles in the 1st layer would be reorganized, which means the formation energy for this structure would be higher than those for defects in Figure 5-14(a). Therefore, such a transition is less favourable from the thermodynamic principles. If instead of nestling into the position as black dashed arrow pointed in Figure 5-14(b), and to avoid structure transition, because of thickness constraint, the 3rd layer would only start to pack at the octahedral

interstice formed by row 8 and row 9 of the 1st layer and two tangent rows of 2nd layer (as red arrow pointed in Figure 5-14(b)), where the available thickness $d = 534.6$ nm and $d_M = 104.3$ nm $> R$ (200 nm). And the local density of the structure, between row 1 and row 8 of the 1st layer, is 16.2% (v/v), while the structure density in Figure 5-14(a) is 15.2% (v/v). So, the resultant structure shown in Figure 5-14(b) is another packing option. Here the up-pointing interstices of 1st layer were chosen to cover when packing particles of 2nd layer. And in order to avoid interparticle overlapping between particles at row 2 and row 3 of the 2nd layer, line defect occurred after square stacking transition area (Figure 5-14(a)). As the particle stacking continued, rectangular transition area occurred when particles in the 3rd layer settled down (Figure 5-14(a)).

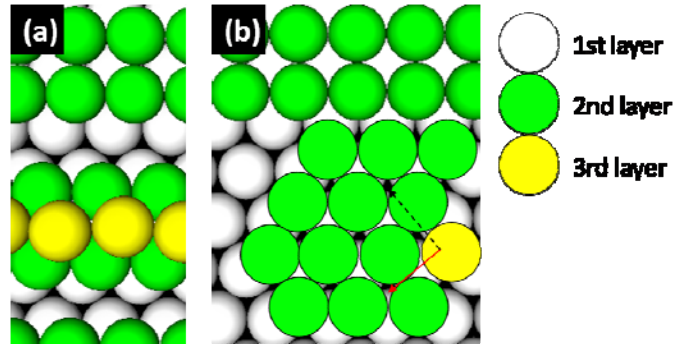


Figure 5-14. Structures comparison for two different packing options.

(Note: (a) Resultant crystal structure with rectangular transition area, and (b) hypothetical packing option for crystal structure without rectangular transition area.)

5.4 CONCLUSIONS

In this study a DEM-based computer model has been established to simulate the colloidal self-assembly process for revealing the information that are inaccessible by experimental means. The interparticle interactions, particle-boundary interactions, particle movement and packing of particles have been built in the simulation platform based on the physical laws. A set of rules and their corresponding numerical schemes have been established to describe the movement of the particles under the influence of fluid flow field and

geometrical confinement. It was found that the growing crystal structure became more close-packed when the fluid flow velocity increased, and that the structural transitions occurred in different areas when the wedge angle θ varied. By solely increasing the fluid velocity in the transverse direction, large area of colloidal monolayer may be formed. The knowledge derived from the simulations will be useful to effectively control the growth of colloidal crystal structure. The simulation platform can be further extended as a versatile virtual tool for studying binary crystal formation and epitaxial crystal growth.

CHAPTER SIX

CONCLUSIONS AND FUTURE WORK

6.1 CONCLUSIONS

The objectives of this study as outlined in Chapter 1 have been achieved, with a particular attention paid to the development of simulation platform 'SimCos' for the colloidal suspension system.

A state-of-the-art review of DEM simulation methods used to simulate various granular flows behaviour of microscale particles and different numerical simulation methods used to simulate submicro to nanoscale colloidal particles have been presented, pointing out the shortcomings of other simulation studies on colloidal particles and the lack of applications of DEM simulation on colloidal particles system, which have therefore been the motivation of this study.

6.1.1 Development of Simulation Platform

As currently there is no specific commercial software suitable for simulating submicro to nanoscale particles behaviour in colloidal suspensions, the simulation platform 'SimCos' was developed. With DEM simulation method, the main interaction forces involved in the model were hydration force, DLVO forces, Brownian force, and hydrodynamic drag force, which could be implemented separately to study and compare the effect of each force on particles behaviour. The system was divided into cubic cells as a mesh system and the neighbourhood list was implemented during particles searching process to minimize the usage of computation processing power.

Data read software was developed to read out data samples at specific time steps from large volume simulation results data and convert the binary data to decimal data which were then easier to output for data analysis.

Off-line data 3D demonstration was developed to present snapshots through a vivid 3D view of simulation process for any particular particles at any particular time step, so as to clearly track trajectories of particles and check interaction between particles. And with a preset large data sample time step during reading off-line simulation data, the nanoscale invisible simulation process was presented in a larger visible time scale, and the movements of particles were tracked in a easier and efficient way.

6.1.2 Diffusion Coefficient Analysis of Brownian Particle

The diffusion of spherical colloidal particle suspended in aqueous solution was simulated and the simulation model was validated by comparing to the experimental work done by Lin *et al.*. The diffusion coefficient analysis of colloidal particle was extended to the very close distance (less than 100 nm) to the planar wall, and studied for different particle size and charged system.

Calculated from simulation results data, the mobility of particle as the diffusion coefficient of spherical colloidal particles in charged suspension was found to be larger than that in neutral suspension, due to the effect of DLVO forces between charged particles and wall. And as the particle moved very close to the planar wall, i.e. $y/R \sim 1$, the asymmetry effect of particle diffusion between perpendicular and parallel directions became more obvious, which were confirmed from the simulation data that the diffusion coefficient in perpendicular direction increased exponentially with second power while the diffusion coefficient in parallel direction decreased.

6.1.3 Simulation of Colloidal Self-assembly

The interparticle interactions, particle-boundary interactions, movement and packing of particles were built in the colloidal self-assembly model based on the physical laws. The motion of the particles and the growing crystal

structure under the influence of fluid flow and geometrical confinement were presented. The increase of fluid flow made more close-packed growing crystal structure, and the increase of fluid flow velocity solely in the transverse direction resulted in formation of large area of colloidal monolayer. Following the variation of wedge angle θ , the structural transitions occurred in different areas. The knowledge derived from the simulations which are inaccessible by experimental means will be useful to effectively control the growth of colloidal crystal structure.

6.2 IDENTIFIED PROBLEMS AND FUTURE WORK

The problems encountered during the modelling and simulation work have been outlined below, together with the recommendations for future work and improvement.

6.2.1 Improvement on Diversity of Geometrical Confinement

During the analysis of diffusion coefficient of Brownian particle in this study, the simulation processed was for a colloidal particle in the vicinity of a planar wall, and one main problem encountered was that the interactions between particle and planar wall varied evenly and monotonically as particle moved towards the plane. Therefore, in order to apply the interaction model and extend the diffusion coefficient analysis influenced by different geometry confinement, diffusion of particle under different geometry confinement, such as cylindrical and spherical confinement can be investigated.

6.2.2 Improvement on Particle Packing Rules

The major problem in the simulation of colloidal self-assembly was the assumption of choosing the up-pointing interstices of 1st layer as settling points for packing of particles in 2nd layer, which was one of the two options for particles packing during self-assembly. And as our simulation study was

mainly interested in the effect of fluid flow and wedge shape angle, the packing rules was simplified. However, in order to study the crystal structure and especially crystal defect completely, the colloid particle packing rules should be polished, by implementing an equilibrium energy calculation and comparison algorithm into the backbone model.

6.2.3 Applications of Simulation Platform ‘SimCos’

The simulation platform ‘SimCos’ developed was a backbone 3D colloid particles simulation environment which can be implemented with different desired interaction models for varying industrial particle handling simulation cases, so as to be further extended as a versatile virtual tool for studying crystal formation of binary particle size, epitaxial crystal growth, and the aggregation of particles. These further applications can be done by changing particle size and accordingly the system mesh size and treating the aggregated particles as a whole body.

REFERENCES

- ALLEN, M. P. & TILDESLEY, D. J. 1987. *Computer Simulation of Liquids*, Oxford, UK, Clarendon Press.
- AMIN, M. & ANTONY, S. J. 2006. Micromechanical behaviour of Si-based particulate assemblies: A comparative study using DEM and atomistic simulations. *Computational Materials Science*, 36, 381-385.
- ASMAR, B. N., LANGSTON, P. A., MATCHETT, A. J. & WALTERS, J. K. 2002. Validation tests on a distinct element model of vibrating cohesive particle systems. *Computers & Chemical Engineering*, 26, 785-802.
- BALEVICIUS, R., DZIUGYS, A., KACIANAUSKAS, R., MAKNICKAS, A. & VISLAVICIUS, K. 2006. Investigation of performance of programming approaches and languages used for numerical simulation of granular material by the discrete element method. *Computer Physics Communications*, 175, 404-415.
- BANERJEE, A. & KIHM, K. D. 2005. Experimental verification of near-wall hindered diffusion for the Brownian motion of nanoparticles using evanescent wave microscopy. *Physical Review E*, 72, 4.
- BARDET, J. P. & SCOTT, R. F. 1985. Seismic stability of fractured rock masses with the distinct element method. *Proceedings of the 26th US Symposium on Rock Mechanics* Rapid City, SD.
- BAREFORD, L. A. & SWAAN, P. W. 2007. Endocytic mechanisms for targeted drug delivery. *Advanced Drug Delivery Reviews*, 59, 748-758.
- BARTOLONI, A., BATTISTA, C., CABASINO, S., PAOLUCCI, P. S., PECH, J., SARNO, R., TODESCO, G. M., TORELLI, M., TROSS, W., VICINI, P., BENZI, R., CABIBBO, N., MASSAIOLI, F. & TRIPICCIONE, R. 1993. Lbe Simulations of Rayleigh-Benard Convection on the Ape100 Parallel Processor. *International Journal of Modern Physics C-Physics and Computers*, 4, 993-1006.
- BASAGAOGLU, H., MEAKIN, P., SUCCI, S., REDDEN, G. R. & GINN, T. R. 2008. Two-dimensional lattice Boltzmann simulation of colloid migration in rough-walled narrow flow channels. *Physical Review E*, 77, -.
- BAXTER, J., BOU-CHAKRA, H., TUZUN, U. & LAMPTEY, B. M. 2000. A DEM simulation and experimental strategy for solving fine powder flow problems. *Chemical Engineering Research & Design*, 78, 1019-1025.
- BERGNA, H. E. & ROBERTS, W. O. 2006. *Colloidal Silica Fundamentals and Applications*, Boca Raton, CRC Press.
- BIZON, C., SHATTUCK, M. D., SWIFT, J. B., MCCORMICK, W. D. & SWINNEY, H. L. 1998. Patterns in 3D vertically oscillated granular layers: Simulation and experiment. *Physical Review Letters*, 80, 57-60.

- BOLHUIS, P. G., FRENKEL, D., MAU, S. C. & HUSE, D. A. 1997. Entropy difference between crystal phases. *Nature*, 388, 235-236.
- BONISSENT, A., PIERANSKI, P. & PIERANSKI, P. 1984. Solid-solid phase transitions in a low-dimensionality system. *Philosophical Magazine A*, 50, 57-64.
- BRANKA, A. C. & HEYES, D. M. 1998. Algorithms for Brownian dynamics simulation. *Physical Review E*, 58, 2611-2615.
- BRANKA, A. C. & HEYES, D. M. 1999. Algorithms for Brownian dynamics computer simulations: Multivariable case. *Physical Review E*, 60, 2381-2387.
- BRENNER, H. 1961. The slow motion of a sphere through a viscous fluid towards a plane surface. *Chemical Engineering Science*, 16, 242-251.
- BRENNER, H. 1962. Effect of finite boundaries on the Stokes resistance of an arbitrary particle. *Journal of Fluid Mechanics*, 12, 144-158.
- BREWER, D. D., ALLEN, J., MILLER, M. R., DE SANTOS, J. M., KUMAR, S., NORRIS, D. J., TSAPATSIS, M. & SCRIVEN, L. E. 2008. Mechanistic principles of colloidal crystal growth by evaporation-induced convective steering. *Langmuir*, 24, 13683-13693.
- BURADA, P. S., HANGGI, P., MARCHESONI, F., SCHMID, G. & TALKNER, P. 2009. Diffusion in Confined Geometries. *Chemphyschem*, 10, 45-54.
- BUTT, H. J., GRAF, K. & KAPPL, M. 2003. Physics and chemistry of interfaces. Weinheim: Wiley-VCH Verlag GmbH & Co. KGaA.
- CAMPBELL, C. S., CLEARY, P. W. & HOPKINS, M. 1995. Large-Scale Landslide Simulations - Global Deformation, Velocities and Basal Friction. *Journal of Geophysical Research-Solid Earth*, 100, 8267-8283.
- CARBAJAL-TINOCO, M. D., LOPEZ-FERNANDEZ, R. & ARAUZ-LARA, J. L. 2007. Asymmetry in colloidal diffusion near a rigid wall. *Physical Review Letters*, 99, 4.
- CHANDRASEKHAR, S. 1943. Stochastic problems in physics and astronomy. *Reviews of Modern Physics*, 15, 0001-0089.
- CHEN, J. C., ELIMELECH, M. & KIM, A. S. 2005. Monte Carlo simulation of colloidal membrane filtration: Model development with application to characterization of colloid phase transition. *Journal of Membrane Science*, 255, 291-305.
- CHEN, J. C. & KIM, A. S. 2006. Monte Carlo simulation of colloidal membrane filtration: Principal issues for modeling. *Advances in Colloid and Interface Science*, 119, 35-53.
- CHEN, S. & DOOLEN, G. D. 1998. Lattice Boltzmann method for fluid flows. *Annual Review of Fluid Mechanics*, 30, 329-364.

- CHEN, Y., OHASHI, H. & AKIYAMA, M. 1994. THERMAL LATTICE BHATNAGAR-GROSS-KROOK MODEL WITHOUT NONLINEAR DEVIATIONS IN MACRODYNAMIC EQUATIONS. *Physical Review E*, 50, 2776-2783.
- CLEARY, P. W. & CAMPBELL, C. S. 1993. Self-Lubrication for Long Runout Landslides - Examination by Computer-Simulation. *Journal of Geophysical Research-Solid Earth*, 98, 21911-21924.
- CLEARY, P. W. & PRAKASH, N. 2004. Discrete-element modelling and smoothed particle hydrodynamics: potential in the environmental sciences. *Philosophical Transactions of the Royal Society of London Series A-Mathematical Physical and Engineering Sciences*, 362, 2003-2030.
- CLEARY, P. W. & SINNOTT, M. D. 2008. Assessing mixing characteristics of particle-mixing and granulation devices. *Particuology*, 6, 419-444.
- CORDELAIR, J. & GREIL, P. 2004. Discrete element modeling of solid formation during electrophoretic deposition. *Journal of Materials Science*, 39, 1017-1021.
- CORMA, A. 1997. From microporous to mesoporous molecular sieve materials and their use in catalysis. *Chemical Reviews*, 97, 2373-2419.
- CUNDALL, P. A. & STRACE, O. D. L. 1979. A discrete numerical model for granular assemblies. *Geotechnique*, 29, 47-65.
- DANIEL, M. C. & ASTRUC, D. 2004. Gold nanoparticles: Assembly, supramolecular chemistry, quantum-size-related properties, and applications toward biology, catalysis, and nanotechnology. *Chemical Reviews*, 104, 293-346.
- DENKOV, N. D., VELEV, O. D., KRALCHEVSKY, P. A., IVANOV, I. B., YOSHIMURA, H. & NAGAYAMA, K. 1993. Two-dimensional crystallization. *Nature*, 361, 26-26.
- DERJAGUIN, B. V. & KUSSAKOV, M. M. 1939. Anomalous Properties of Thin Polymolecular Films. *Acta Phys. Chim. URSS* 10.
- DICKINSON, E. 2000. Structure and rheology of simulated gels formed from aggregated colloidal particles. *Journal of Colloid and Interface Science*, 225, 2-15.
- DIMITROV, A. S. & NAGAYAMA, K. 1996. Continuous convective assembling of fine particles into two-dimensional arrays on solid surfaces. *Langmuir*, 12, 1303-1311.
- DUNWEG, B. & LADD, A. J. C. 2009. Lattice Boltzmann Simulations of Soft Matter Systems. *Advanced Computer Simulation Approaches for Soft Matter Sciences Iii*, 221, 89-166.
- EINSTEIN, A. 1905. The motion of elements suspended in static liquids as claimed in the molecular kinetic theory of heat. *ANNALEN DER PHYSIK* 17.
- ERMAK, D. L. 1975. Computer-Simulation of Charged-Particles in Solution .1. Technique and Equilibrium Properties. *Journal of Chemical Physics*, 62, 4189-4196.

- ERMAK, D. L. & MCCAMMON, J. A. 1978. Brownian Dynamics with Hydrodynamic Interactions. *Journal of Chemical Physics*, 69, 1352-1360.
- FANG, H. F. & LI, Q. 2009. SimCos software documentation. *Internal Report*.
- FAUCHEUX, L. P. & LIBCHABER, A. J. 1994. Confined Brownian-Motion. *Physical Review E*, 49, 5158-5163.
- FAXEN, H. 1923. Die Bewegung einer starren K ge l ngs der Achse eines mit z her Fl ssigkeit gef llten Rohres. *Ark. Mat. Astron. Fys.*, 27.
- FEDER, J. 1980. Random Sequential Adsorption. *Journal of Theoretical Biology*, 87, 237-254.
- FEITOSA, M. I. M. & MESQUITA, O. N. 1991. WALL-DRAG EFFECT ON DIFFUSION OF COLLOIDAL PARTICLES NEAR SURFACES - A PHOTON-CORRELATION STUDY. *Physical Review A*, 44, 6677-6685.
- FENG, Y. Q., XU, B. H., ZHANG, S. J., YU, A. B. & ZULLI, P. 2004. Discrete particle simulation of gas fluidization of particle mixtures. *Aiche Journal*, 50, 1713-1728.
- FONTECHA, A. B., SCHOPPE, H. J., KONIG, H., PALBERG, T., MESSINA, R. & LOWEN, H. 2005. A comparative study on the phase behaviour of highly charged colloidal spheres in a confining wedge geometry. *Journal of Physics: Condensed Matter*, 17, S2779-S2786.
- FOSNARIC, M., IGLIC, A., KROLL, D. M. & MAY, S. 2009. Monte Carlo simulations of complex formation between a mixed fluid vesicle and a charged colloid. *Journal of Chemical Physics*, 131, -.
- FRENKEL, D. & EPPENGA, R. 1982. Monte-Carlo Study of the Isotropic-Nematic Transition in a Fluid of Thin Hard Disks. *Physical Review Letters*, 49, 1089-1092.
- FRENKEL, D. & LADD, A. J. C. 1984a. New Monte-Carlo Method to Compute the Free-Energy of Arbitrary Solids - Application to the Fcc and Hcp Phases of Hard-Spheres. *Journal of Chemical Physics*, 81, 3188-3193.
- FRENKEL, D. & LADD, A. J. C. 1984b. New Monte Carlo method to compute the free energy of arbitrary solids - application to the fcc and hcp phases of hard spheres. *Journal of Chemical Physics*, 81, 3188-3193.
- FREY, E. & KROY, K. 2005. Brownian motion: a paradigm of soft matter and biological physics. *Annalen Der Physik*, 14, 20-50.
- FUJITA, M. & YAMAGUCHI, Y. 2008. Simulation model of concentrated colloidal nanoparticulate flows. *Physical Review E*, 77, -.
- FUSTIN, C. A., GLASSER, G., SPIESS, H. W. & JONAS, U. 2004. Parameters influencing the templated growth of colloidal crystals on chemically patterned surfaces. *Langmuir*, 20, 9114-9123.

- GALLAS, J. A. C., HERRMANN, H. J. & SOKOLOWSKI, S. 1992. Convection Cells in Vibrating Granular Media. *Physical Review Letters*, 69, 1371-1374.
- GAMBIN, Y., LOPEZ-ESPARZA, R., REFFAY, M., SIERECKI, E., GOV, N. S., GENEST, M., HODGES, R. S. & URBACH, W. 2006. Lateral mobility of proteins in liquid membranes revisited. *Proceedings of the National Academy of Sciences of the United States of America*, 103, 2098-2102.
- GASPERINO, D., MENG, L. L., NORRIS, D. J. & DERBY, J. J. 2008. The role of fluid flow and convective steering during the assembly of colloidal crystals. *Journal of Crystal Growth*, 310, 131-139.
- GLOTZER, S. C., SOLOMON, M. J. & KOTOV, N. A. 2004. Self-assembly: From nanoscale to microscale colloids. *Aiche Journal*, 50, 2978-2985.
- GOLDMAN, A. 1967. Slow viscous motion of a sphere parallel to a plane wall 鈥檛 Motion through a quiescent fluid. *Chemical Engineering Science*, 22, 637-651.
- GRANFELDT, M. K., JONSSON, B. & WOODWARD, C. E. 1991. A Monte-Carlo Simulation Study of the Interaction between Charged Colloids Carrying Adsorbed Polyelectrolytes. *Journal of Physical Chemistry*, 95, 4819-4826.
- GRAY, J. J. & BONNECAZE, R. T. 2001. Adsorption of colloidal particles by Brownian dynamics simulation: Kinetics and surface structures. *Journal of Chemical Physics*, 114, 1366-1381.
- GRAY, J. J., KLEIN, D. H., BONNECAZE, R. T. & KORGEL, B. A. 2000. Nonequilibrium phase behavior during the random sequential adsorption of tethered hard disks. *Physical Review Letters*, 85, 4430-4433.
- GRIER, D. G. 1997. Optical tweezers in colloid and interface science. *Current Opinion in Colloid & Interface Science*, 2, 264-270.
- GRZYBOWSKI, B. A., WILMER, C. E., KIM, J., BROWNE, K. P. & BISHOP, K. J. M. 2009. Self-assembly: from crystals to cells. *Soft Matter*, 5, 1110-1128.
- GUNAL, Y. & VISSCHER, P. B. 1996. Brownian dynamics simulation of magnetic colloid aggregation. *Ieee Transactions on Magnetics*, 32, 4049-4051.
- HANGGI, P. & MARCHESONI, F. 2005. Introduction: 100 years of Brownian motion. *Chaos*, 15, 5.
- HE, X., CHEN, S. & DOOLEN, G. D. 1998. A novel thermal model for the lattice Boltzmann method in incompressible limit. *Journal of Computational Physics*, 146, 282-300.
- HE, Y. L., LI, Q., WANG, Y. & TANG, G. H. 2009. Lattice Boltzmann method and its applications in engineering thermophysics. *Chinese Science Bulletin*, 54, 4117-4134.

- HEYES, D. M. 1988. Rheology of Molecular Liquids and Concentrated Suspensions by Microscopic Dynamical Simulations. *Journal of Non-Newtonian Fluid Mechanics*, 27, 47-85.
- HONG, C. W. 1997. New concept for simulating particle packing in colloidal forming processes. *Journal of the American Ceramic Society*, 80, 2517-2524.
- HOOMANS, B. P. B., KUIPERS, J. A. M., BRIELS, W. J. & VANSWAAIJ, W. P. M. 1996. Discrete particle simulation of bubble and slug formation in a two-dimensional gas-fluidised bed: A hard-sphere approach. *Chemical Engineering Science*, 51, 99-118.
- HOPKINS, M. A., DALY, S. F. & LEVER, J. H. 1996. Three-dimensional simulation of river ice jams. *Proceedings of the 8th International Specialty Conference on Cold Regions Engineering*. Fairbanks, AK.
- HUNTER, R. J. 2001. *Foundations of colloid science*. New York: Oxford University Press.
- HUTTER, M. 1999. *Brownian Dynamics Simulation of Stable and Coagulating Suspensions*. Ph.D. dissertation, University of Zurich.
- ISRAELACHVILI, J. & WENNERSTROM, H. 1996. Role of hydration and water structure in biological and colloidal interactions. *Nature*, 379, 219-225.
- ISRAELACHVILI, J. N. 1992. *Intermolecular and Surface Forces*, London, Academic Press Limited.
- JIANG, P., BERTONE, J. F., HWANG, K. S. & COLVIN, V. L. 1999. Single-crystal colloidal multilayers of controlled thickness. *Chemistry of Materials*, 11, 2132-2140.
- JUN, Y., LEATHERDALE, C. A. & NORRIS, D. J. 2005. Tailoring air defects in self-assembled photonic bandgap crystals. *Advanced Materials*, 17, 1908-1911.
- KATAOKA, T. & TSUTAHARA, M. 2004. Lattice Boltzmann method for the compressible Euler equations. *Physical Review E*, 69, 14.
- KHANAL, M., SCHUBERT, W. & TOMAS, J. 2007. Discrete element method simulation of bed comminution. *Minerals Engineering*, 20, 179-187.
- KIM, J. P., HAN, I. S. & CHUNG, C. B. 2003. Monte Carlo simulations of colloidal particle coagulation and breakup under turbulent shear. *Korean Journal of Chemical Engineering*, 20, 580-586.
- KRUGGEL-EMDEN, H., STURM, M., WIRTZ, S. & SCHERER, V. 2008. Selection of an appropriate time integration scheme for the discrete element method (DEM). *Computers & Chemical Engineering*, 32, 2263-2279.
- KUO, H. P., KNIGHT, P. C., PARKER, D. J., TSUJI, Y., ADAMS, M. J. & SEVILLE, J. P. K. 2002. The influence of DEM simulation parameters on the particle behaviour in a V-mixer. *Chemical Engineering Science*, 57, 3621-3638.

- LADD, A. J. C. & VERBERG, R. 2001. Lattice-Boltzmann simulations of particle-fluid suspensions. *Journal of Statistical Physics*, 104, 1191-1251.
- LARSON, R. G. 1999. *The Structure and Rheology of Complex Fluids*, Oxford, Oxford University Press.
- LEMIEUX, A., LEONARD, G., DOUCET, J., LECLAIRE, L. A., VIENS, F., CHAOUKI, J. & BERTRAND, F. 2008. Large-scale numerical investigation of solids mixing in a V-blender using the discrete element method. *Powder Technology*, 181, 205-216.
- LI, Q., JONAS, U., ZHAO, X. S. & KAPPL, M. 2008. The forces at work in colloidal self-assembly: a review on fundamental interactions between colloidal particles. *Asia-Pacific Journal of Chemical Engineering* 3, 255-268.
- LI, Q., RUDOLPH, V., WANG, F. Y. & HORIO, M. 2005. A study of particle packing compression under fluid drag force by DEM simulations. *Developments in Chemical Engineering and Mineral Processing*, 13, 693-708.
- LIM, C. Y., SHU, C., NIU, X. D. & CHEW, Y. T. 2002. Application of lattice Boltzmann method to simulate microchannel flows. *Physics of Fluids*, 14, 2299-2308.
- LIN, B. H., YU, J. & RICE, S. A. 2000. Direct measurements of constrained Brownian motion of an isolated sphere between two walls. *Physical Review E*, 62, 3909-3919.
- LINK, J. M., GODLIEB, W., DEEN, N. G. & KUIPERS, J. A. M. 2007. Discrete element study of granulation in a spout-fluidized bed. *Chemical Engineering Science*, 62, 195-207.
- LINK, J. M., GODLIEB, W., TRIPP, P., DEEN, N. G., HEINRICH, S., KUIPERS, J. A. M., SCHONHERR, M. & PEGLOW, M. 2009. Comparison of fibre optical measurements and discrete element simulations for the study of granulation in a spout fluidized bed. *Powder Technology*, 189, 202-217.
- LOPEZ, C. 2003. Materials aspects of photonic crystals. *Advanced Materials*, 15, 1679-1704.
- MAU, S. C. & HUSE, D. A. 1999. Stacking entropy of hard-sphere crystals. *Physical Review E*, 59, 4396-4401.
- MCNAMARA, G. & ALDER, B. 1993. ANALYSIS OF THE LATTICE BOLTZMANN TREATMENT OF HYDRODYNAMICS. *Physica A*, 194, 218-228.
- MCNAMARA, G. R., GARCIA, A. L. & ALDER, B. J. 1997. A hydrodynamically correct thermal lattice Boltzmann model. *Journal of Statistical Physics*, 87, 1111-1121.
- MCNAMARA, G. R. & ZANETTI, G. 1988. Use of the Boltzmann-Equation to Simulate Lattice-Gas Automata. *Physical Review Letters*, 61, 2332-2335.
- MENG, L. L., WEI, H., NAGEL, A., WILEY, B. J., SCRIVEN, L. E. & NORRIS, D. J. 2006. The role of thickness transitions in convective assembly. *Nano Letters*, 6, 2249-2253.

- METROPOLIS, N., ROSENBLUTH, A. W., ROSENBLUTH, M. N., TELLER, A. H. & TELLER, E. 1953. Equation of State Calculations by Fast Computing Machines. *The Journal of Chemical Physics*, 21, 1087-1092.
- MIGUEZ, H., MESEGUER, F., LÓPEZ, C., MIFSUD, A., MOYA, J. S. & VAZQUEZ, L. 1997. Evidence of FCC crystallization of SiO₂ nanospheres. *Langmuir*, 13, 6009-6011.
- MILCHEV, A. & BHATTACHARYA, A. 2002. Polymer depletion interaction between a colloid particle and a wall: A Monte Carlo study. *Journal of Chemical Physics*, 117, 5415-5420.
- MORGAN, J. K. 2006. Volcanotectonic interactions between Mauna Loa and Kilauea: Insights from 2-D discrete element simulations. *Journal of Volcanology and Geothermal Research*, 151, 109-131.
- NEUMAN, K. C. & BLOCK, S. M. 2004. Optical trapping. *Review of Scientific Instruments*, 75, 2787-2809.
- NEZAMI, E. G., HASHASH, Y. M. A., ZHAO, D. W. & GHABOUSSI, J. 2004. A fast contact detection algorithm for 3-D discrete element method. *Computers and Geotechnics*, 31, 575-587.
- NIE, X. B., DOOLEN, G. D. & CHEN, S. Y. 2002. Lattice-Boltzmann simulations of fluid flows in MEMS. *Journal of Statistical Physics*, 107, 279-289.
- NORRIS, D. J., ARLINGHAUS, E. G., MENG, L. L., HEINY, R. & SCRIVEN, L. E. 2004. Opaline photonic crystals: How does self-assembly work? *Advanced Materials*, 16, 1393-1399.
- ODRIOZOLA, G., ROMERO-BASTIDA, M. & GUEVARA-RODRIGUEZ, F. D. 2004. Brownian dynamics simulations of Laponite colloid suspensions. *Physical Review E*, 70, -.
- OLIVI-TRAN, N., BOTET, R. & CABANE, B. 1998. Monte Carlo simulations of colloidal dispersions under shear. *Physical Review E*, 57, 1997-2003.
- OUNIS, H., AHMADI, G. & MCLAUGHLIN, J. B. 1991. Brownian Diffusion of Submicrometer Particles in the Viscous Sublayer. *Journal of Colloid and Interface Science*, 143, 266-277.
- PALBERG, T. & BIEHL, R. 2003. Sheared colloidal crystals in confined geometry: a real space study on stationary structures under shear. *Faraday Discussions*, 123, 133-143.
- PANSU, B., PIERANSKI, P. & PIERANSKI, P. 1984. Structures of thin layers of hard spheres: high pressure limit. *Journal De Physique*, 45, 331-339.
- PENG, C. S., SONG, S. X. & FORT, T. 2006. Study of hydration layers near a hydrophilic surface in water through AFM imaging. *Surface and Interface Analysis*, 38, 975-980.

- PESCHEL, G., BELOUSCHEK, P., MULLER, M. M., MULLER, M. R. & KONIG, R. 1982. The Interaction of Solid-Surfaces in Aqueous Systems. *Colloid and Polymer Science*, 260, 444-451.
- PHULE, P. P. & GINDER, J. M. 1998. The materials science of field-responsive fluids. *MRS Bulletin*, 23, 19-21.
- PLUM, M. A., STEFFEN, W., FYTAS, G., KNOLL, W. & MENGES, B. 2009. Probing dynamics at interfaces: resonance enhanced dynamic light scattering. *Optics Express*, 17, 10364-10371.
- PUSEY, P. N., VANMEGEN, W., BARTLETT, P., ACKERSON, B. J., RARITY, J. G. & UNDERWOOD, S. M. 1989. Structure of crystals of hard colloidal spheres. *Physical Review Letters*, 63, 2753-2756.
- RABIDEAU, B. D. & BONNECAZE, R. T. 2004. Computational study of the self-organization of bidisperse nanoparticles. *Langmuir*, 20, 9408-9414.
- RAMSTEINER, I. B., JENSEN, K. E., WEITZ, D. A. & SPAEPEN, F. 2009. Experimental observation of the crystallization of hard-sphere colloidal particles by sedimentation onto flat and patterned surfaces. *Physical Review E*, 79, 011403.
- REIMANN, P. 2002. Brownian motors: noisy transport far from equilibrium. *Physics Reports-Review Section of Physics Letters*, 361, 57-265.
- RICCI, A. & CICCOTTI, G. 2003. Algorithms for Brownian dynamics. *Molecular Physics*, 101, 1927-1931.
- RISTOW, G. H. 1992. Simulating Granular Flow with Molecular-Dynamics. *Journal de Physique I*, 2, 649-662.
- RUSSEL, W. B., SAVILLE, D. A. & SCHOWALTER, W. R. 1989. *Colloidal Suspensions*, Cambridge, Cambridge University Press.
- SAKKA, Y. & SUZUKI, T. S. 2005. New processing of textured ceramics by colloidal processing under high magnetic field. In: PAN, W., GONG, J. H., GE, C. C. & LI, J. F. (eds.) *High-Performance Ceramics Iii, Pts 1 and 2*. Zurich-Uetikon: Trans Tech Publications Ltd.
- SASAKI, S. & MAEDA, H. 1994. Electrostatic Effect on the Hydration Layer of Colloidal Silica Particles. *Journal of Colloid and Interface Science*, 167, 146-149.
- SATOH, A., CHANTRELL, R. W. & COVERDALE, G. N. 1999. Brownian dynamics simulations of ferromagnetic colloidal dispersions in a simple shear flow. *Journal of Colloid and Interface Science*, 209, 44-59.
- SCHAFFER, E., NORRELYKKE, S. F. & HOWARD, J. 2007. Surface forces and drag coefficients of microspheres near a plane surface measured with optical tweezers. *Langmuir*, 23, 3654-3665.

- SEVERENS, I. E. M., DE VEN, A. A. F. V., WOLF, D. E. & MATTHEIJ, R. M. M. 2006. Discrete element method simulations of toner behavior in the development nip of the Oce Direct Imaging print process. *Granular Matter*, 8, 137-150.
- SHOLL, D. S., FENWICK, M. K., ATMAN, E. & PRIEVE, D. C. 2000. Brownian dynamics simulation of the motion of a rigid sphere in a viscous fluid very near a wall. *Journal of Chemical Physics*, 113, 9268-9278.
- SKVARLA, J. & KMET, S. 1991. Influence of Wettability on the Aggregation of Fine Minerals. *International Journal of Mineral Processing*, 32, 111-131.
- SMOLUCHOWSKI, M. V. 1906. Zur kinetischen Theorie der Brownschen Molekularbewegung und der Suspensionen. *Annalen der Physik*, 326, 756-780.
- SOKOLOV, I. M. & KLAFTER, J. 2005. From diffusion to anomalous diffusion: A century after Einstein's Brownian motion. *Chaos*, 15, -.
- STEWART, R. L., BRIDGWATER, J., ZHOU, Y. C. & YU, A. B. 2001. Simulated and measured flow of granules in a bladed mixer - a detailed comparison. *Chemical Engineering Science*, 56, 5457-5471.
- STOLL, S. & PEFFERKORN, E. 1996. Monte Carlo simulation of controlled colloid growth by homo- and heterocoagulation in two dimensions. *Journal of Colloid and Interface Science*, 177, 192-197.
- SUCCI, S. 2001. *The Lattice Boltzmann Equation for Fluid Dynamics and Beyond*, Oxford, Clarendon Press.
- TANG, G. H., TAO, W. Q. & HE, Y. L. 2005. Gas slippage effect on microscale porous flow using the lattice Boltzmann method. *Physical Review E*, 72, 8.
- TSUJI, Y., KAWAGUCHI, T. & TANAKA, T. 1993. Discrete particle simulation of two-dimensional fluidized bed. *Powder Technology*, 77, 79-87.
- UNNI, H. N. & YANG, C. 2005. Brownian dynamics simulation and experimental study of colloidal particle deposition in a microchannel flow. *Journal of Colloid and Interface Science*, 291, 28-36.
- VALLE-DELGADO, J. J., MOLINA-BOLIVAR, J. A., GALISTEO-GONZALEZ, F., GALVEZ-RUIZ, M. J., FEILER, A. & RUTLAND, M. W. 2005. Existence of hydration forces in the interaction between apoferritin molecules adsorbed on silica surfaces. *Langmuir*, 21, 9544-9554.
- VANGUNSTEREN, W. F. & BERENDSEN, H. J. C. 1982. Algorithms for Brownian Dynamics. *Molecular Physics*, 45, 637-647.
- VLASOV, Y. A., BO, X. Z., STURM, J. C. & NORRIS, D. J. 2001. On-chip natural assembly of silicon photonic bandgap crystals. *Nature*, 414, 289-293.

- WALZ, J. Y. & SURESH, L. 1995. Study of the sedimentation of a single particle toward a flat plate. *Journal of Chemical Physics*, 103, 10714-10725.
- WANG, J. J., LI, Q., KNOLL, W. & JONAS, U. 2006. Preparation of multilayered trimodal colloid crystals and binary inverse opals. *Journal of the American Chemical Society*, 128, 15606-15607.
- WEITZ, D. A. & RUSSEL, W. B. 2004. New developments in colloid science. *MRS Bulletin*, 29, 82-83.
- WONG, S., KITAEV, V. & OZIN, G. A. 2003. Colloidal crystal films: Advances in universality and perfection. *Journal of the American Chemical Society*, 125, 15589-15598.
- WOODCOCK, L. V. 1997. Entropy difference between the face-centred cubic and hexagonal close-packed crystal structures. *Nature*, 385, 141-143.
- XIA, Y. N., GATES, B. & LI, Z. Y. 2001. Self-assembly approaches to three-dimensional photonic crystals. *Advanced Materials*, 13, 409-413.
- XIA, Y. N., GATES, B., YIN, Y. D. & LU, Y. 2000. Monodispersed colloidal spheres: Old materials with new applications. *Advanced Materials*, 12, 693-713.
- YANG, R. Y., ZOU, R. P. & YU, A. B. 2000. Computer simulation of the packing of fine particles. *Physical Review E*, 62, 3900-3908.
- YOTSUMOTO, H. & YOON, R. H. 1993. Application of Extended DLVO Theory .2. Stability of Silica Suspensions. *Journal of Colloid and Interface Science*, 157, 434-441.
- YUU, S., ABE, T., SAITOH, T. & UMEKAGE, T. 1995. Three-dimensional numerical simulation of the motion of particles discharging from a rectangular hopper using distinct element method and comparison with experimental data (effects of time steps and material properties). *Advanced Powder Technology*, 6, 259-269.
- ZHOU, Z. C., LI, Q. & ZHAO, X. S. 2006. Evolution of interparticle capillary forces during drying of colloidal crystals. *Langmuir*, 22, 3692-3697.
- ZHU, H. P. & YU, A. B. 2004. Steady-state granular flow in a three-dimensional cylindrical hopper with flat bottom: microscopic analysis. *Journal of Physics D-Applied Physics*, 37, 1497-1508.

Every reasonable effort has been made to acknowledge the owners of copyright material. I would be pleased to hear from any copyright owner who has been omitted or incorrectly acknowledged.